REVIEW

Emerging Halide Superionic Conductors for All-Solid-State Batteries: Design, Synthesis, and Practical Applications

Hiram Kwak,[⊥] Shuo Wang,[⊥] Juhyoun Park, Yunsheng Liu, Kyu Tae Kim, Yeji Choi, Yifei Mo,* and Yoon Seok Jung*

Cite This: ACS Energy Lett. 2022, 7, 1776−1805

Read Online

ACCESS | 📊 Metrics & More | 📖 Article Recommendations | SI Supporting Information

ABSTRACT: Recently, halide superionic conductors have emerged as promising solid electrolyte (SE) materials for all-solid-state batteries (ASSBs), owing to their inherent properties combining high Li$^+$ conductivity, good chemical and electrochemical oxidation stabilities, and mechanical deformability, compared to sulfide or oxide SEs. In this Review, recent advances in halide Li$^+$- and Na$^+$-conducting SEs are comprehensively summarized. After introducing the ionic diffusion mechanism and related governing factors of the crystal structures, we discuss the design strategies, such as the substitution and synthesis protocols, of the halide materials for further improving their properties. We review theoretical and experimental results on electrochemical stabilities and compatibilities with electrode materials. Moreover, we offer a critical assessment of the challenges and issues associated with the development of practical ASSB applications, such as cost considerations, stabilities in atmospheric air, aqueous solutions, and slurry-processing, and the wet-slurry or dry fabrication of sheet-type electrodes (or SE membranes) for large-format ASSBs. Based on these discussions, we provide a perspective on the future research directions of halide SEs, emphasizing the need for expanding the materials space.
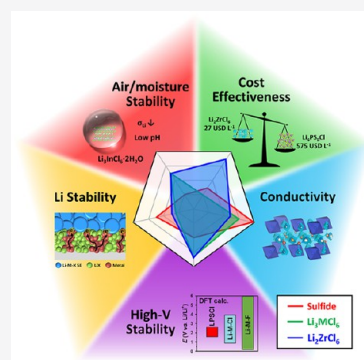
Lithium-ion batteries (LIBs) have revolutionized energy storage from portable electronics to electrical vehicles and battery-based utility-scale storage.[1−3] While the development of optimal organic liquid electrolytes is vital for enabling stable cycling of electrode chemistries in LIBs, safety hazards originating from the flammability of these organic liquid electrolytes pose significant threats to the further advancement of LIB technologies.[3,4] Moreover, the adoption of new high-energy electrode chemistries, such as Li metal, has driven researchers' interests in the development and applications of solid electrolytes (SEs).[5−14] All-solid-state batteries (ASSBs) employing inorganic superionic conductors (SICs) as SEs are thus considered the most promising next-generation batteries.[5,9,15−23] Thus far, several classes of SEs with ionic conductivities of 1 mS cm^{-1} or higher at room temperature (RT) have been developed and employed for ASSBs. These demonstrated SEs include sulfides (e.g., Li$_{6-y}$PS$_{5-y}$X$_{1+y}$ (X = Cl, Br; y = 0.0−0.5), max. ~10 mS cm^{-1}),[24,25] oxides (e.g., Li$_7$La$_3$Zr$_2$O$_{12}$, max. 1 mS cm^{-1}),[26] halides (e.g., Li$_3$MX$_6$ (X = Cl, Br), max. ~1 mS cm^{-1}),[8,11,27] and *closo*-borates (e.g., 0.7Li-(CB$_9$H$_{10}$)−0.3Li(CB$_{11}$H$_{12}$), 6.7 mS cm^{-1}).[28,29]

Over the past decades, oxide and sulfide SEs have been the most extensively investigated materials classes for ASSBs. However, their employment in ASSB applications faces several challenges (Figure 1). Despite their acceptable stability in atmospheric air and excellent electrochemical oxidation stability, oxide SEs generally suffer from poor ionic contacts with electrode materials, which require hot-sintering processes or the infiltration of liquid or polymer electrolytes.[9,26,30−33] In contrast, sulfide SEs exhibit significant advantages in the cell assembly of ASSBs, thanks to their high ionic conductivities, comparable with those of liquid electrolytes (~10 mS cm^{-1}), and the mechanical sinterability by cold-pressing.[9,31,34,35] However, as a key issue for large-scale applications, sulfide SEs are vulnerable to the water in atmospheric air, which causes the detrimental hydrolysis reaction and releases toxic H$_2$S.[36−41] Moreover, the low intrinsic electrochemical stability windows of sulfide SEs have been well documented by computational and experimental studies.[31,34,35,42] Particularly, sulfide SEs in combination with 4-V-class layered oxide cathodes without
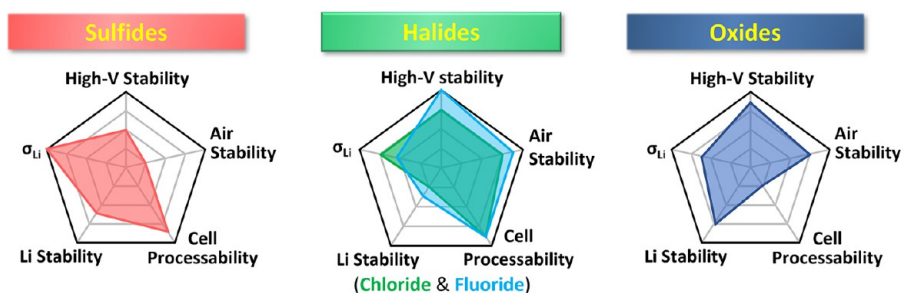
Figure 1. Spider plots comparing the key performances of three major inorganic SEs: sulfides, halides, and oxides.
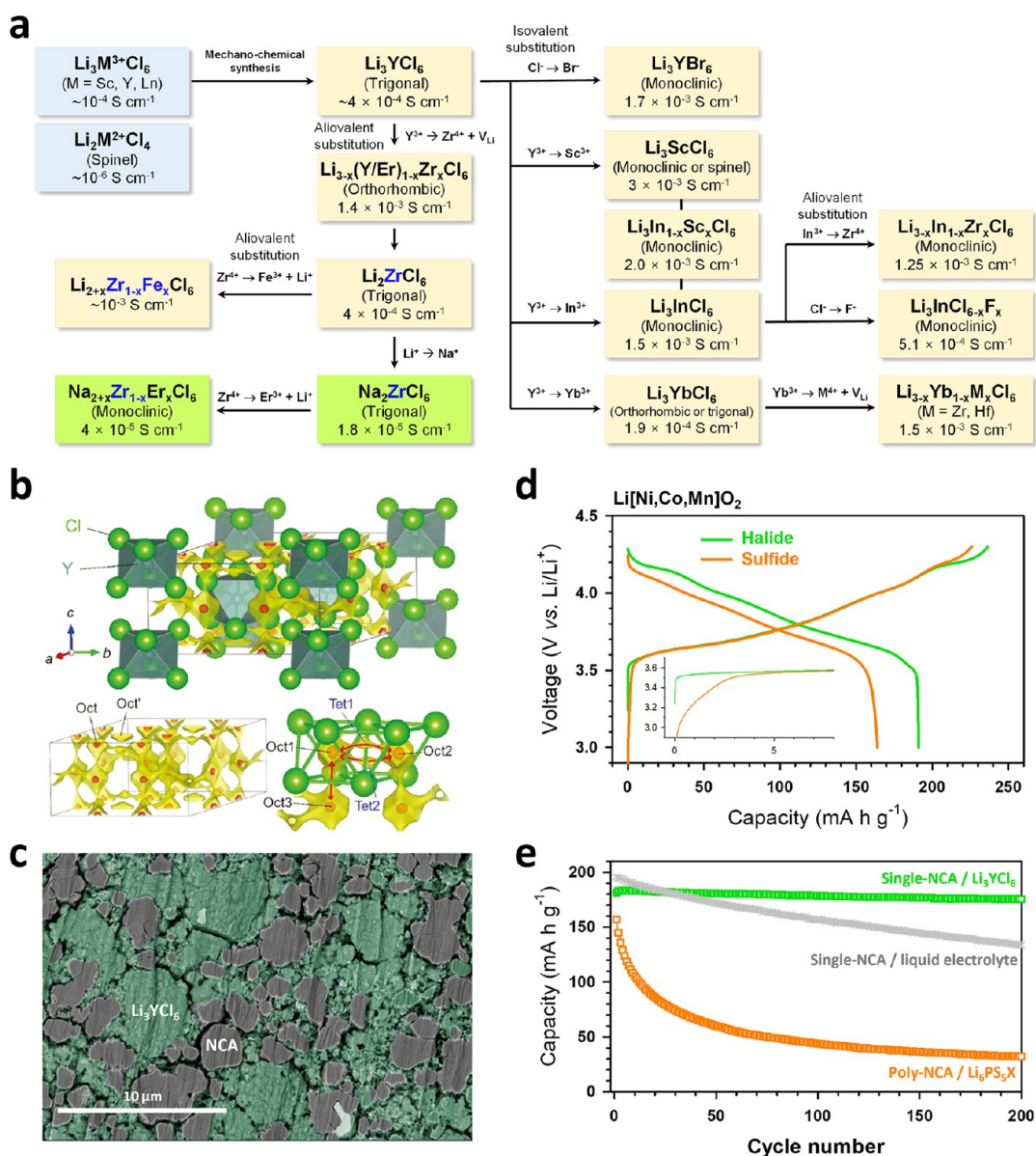

Figure 2. Major features and progress of halide SICs. (a) Progress in development of Li$^+$ and Na$^+$ halide SICs. (b) Crystal structure of Li$_3$YCl$_6$, superimposed with a Li$^+$ potential map obtained using bond valence site energy calculations. Reproduced with permission from ref 27. Copyright 2018, Wiley-VCH. (c) Cross-sectional SEM-BSE image of single-crystalline NCA88 electrodes using Li$_3$YCl$_6$, showing the mechanically deformable feature of Li$_3$YCl$_6$. Reproduced with permission from ref 22. Copyright 2021, Wiley-VCH. (d) First-cycle charge–discharge voltage profiles, and (e) cycling performances for NCA88 electrodes using sulfide (LPSX) and halide (Li$_3$YCl$_6$). Reproduced with permission from ref 22. Copyright 2021, Wiley-VCH.

protective coating layers, such as LiNbO$_3$, Li$_2$ZrO$_3$, and Li$_{3-x}$B$_{1-x}$C$_x$O$_3$, are known to result in poor electrochemical performances of the ASSB cells.[42−45]

Since the ionic conductivity of LiX (X = Cl, Br, I) was first reported in the 1930s, various Li-M-X phases have been investigated,[11,46] including (i) halide spinels with divalent

Table 1. Properties of Halide SEs, Compared with Those of Representative Sulfide and Oxide SEs

SE	structure	ionic conductivity (mS cm^{-1})	specific density (g cm^{-3})	concentration of Li or Na (mol L^{-1})	ref
Li_3YCl_6	trigonal, $P\bar{3}m1$	0.51	2.43	22.61	27
Li_3InCl_6	monoclinic, $C2/m$	1.54	2.71	23.34	111
Li_3ScCl_6	monoclinic, $C2/m$	3.02	2.2	23.70	54
$Li_2Sc_{2/3}Cl_4$	cubic, $Fd\bar{3}m$	1.5	2.19	23.59	77
HT-Li_2ZrCl_6	monoclinic, $C2/m$	0.005	2.53	15.92	49
BM-Li_2ZrCl_6	trigonal, $P\bar{3}m1$	0.51	2.57	16.17	49
Na_2ZrCl_6	trigonal, $P\bar{3}m1$	0.018	2.43	13.89	70
$Na_{2+x}Zr_{1-x}Er_xCl_6$	monoclinic, $P2_1/n$	0.05	2.43–2.97	13.89–19.85	122
Li_3YbCl_6	trigonal, $P\bar{3}m1$	0.1	3.14	23.17	51
	orthorhombic, $Pnma$	0.1	3.12	23.02	51
Li_3YBr_6	monoclinic, $C2/m$	1.7	3.63	18.48	27
$Li_3In[Cl,F]_6$	monoclinic, $C2/m$	0.51	2.55	23.32	127
$Li_2Sc_{2/3-x}In_xCl_4$	cubic, $Fd\bar{3}m$	2	2.2	23.59	50
$Li_{2+x}Zr_{1-x}Fe_xCl_6$	trigonal, $P\bar{3}m1$	0.98	–	–	49
$Li_{2+x}Zr_{1-x}In_xCl_6$	monoclinic, $C2/m$	0.005–2	2.53–2.71	15.92–23.34	61
$Li_{3-x}Yb_{1-x}Zr_xCl_6$	orthorhombic, $Pnma$	1.1	–	–	51
$xLiCl\text{-}GaF_3$	–	3.7	–	–	159
$LiAlF_4$	amorphous	0.001	–	–	175
$Li_{5.5}PS_{4.5}Cl_{1.5}$	cubic, $F\bar{4}3m$	9.4	1.88	38.78	176
$Li_{10}GeP_2S_{12}$	tetragonal, $P42/nmc$	10	2.08	35.33	15
$Li_7La_3Zr_2O_{12}$	cubic, $Ia\bar{3}d$	0.1–0.4	5.15	42.93	177
$La_{0.57}Li_{0.29}TiO_3$	tetragonal, $P4/mmm$	0.02	5.14	10.22	178
$LiTi_2(PO_4)_3$	trigonal, $R\bar{3}c$	0.1	2.93	9.97	179

metals (Mg and Zn), (ii) those with group 13 elements, such as Al, Ga, and In, and (iii) those with lanthanide elements, such as Sc, Y, and La−Lu. However, due to the previously perceived poor ionic conduction, the entire halide class did not receive much attention, until 2018, with the inspiring discovery by Asano et al., who reported trigonal Li_3YCl_6 and monoclinic Li_3YBr_6 exhibiting decent RT Li^+ conductivities of 0.51 and 1.7 mS cm^{-1}, respectively. Since then, halide SEs have drawn significant interest from the battery research communities.[27] Several halide SICs with high ionic conductivities (≥1 mS cm^{-1} at RT) were identified (Figure 2a, Table 1). These halide Li^+ conductors are based on close-packed structures, which would not exhibit such fast ion diffusion in sulfide or oxide compounds (Figure 2b).[47,48] According to theoretical studies,[48] the weak bonding between the monovalent halide anion and the mobile Li^+ ions leads to intrinsically low energy barriers for Li^+ diffusion. The low bond strength between the metals and halide anions and the high polarizabilities of halide anions lead to good mechanical deformability, which is greatly beneficial for ASSB cell assembly (Figure 2c).[27,48] In addition, the good electrochemical stabilities of halide SEs result in good compatibilities with 4-V-class $LiMO_2$ (M = Ni, Co, Mn, and Al mixture) cathodes without protective coating (Figure 2d, e) and thus enable good capacities and high initial Coulombic efficiencies (ICEs) for ASSB cells.[22,27,49,50]

Theoretical computations confirmed that chloride and bromide chemistries exhibit both fast Li^+ diffusion and good electrochemical stability, making them promising material systems for SEs.[48] First-principles computation revealed that Li^+ migration in chlorides and bromides has an intrinsically low energy barrier, which can be attributed to a weaker Coulombic interaction of Li^+ with the monovalent Cl^-/Br^- compared to that with O^{2-} and S^{2-}.[48] As a result, halides need not meet the stringent requirements of crystal structures in sulfide and oxide Li^+ conductors.[47] Thermodynamic analyses revealed the intrinsically high oxidation limit of halide anions compared to

the sulfur anions, which affords the halide with a wider stable electrochemical window and superior interfacial compatibility with the cathode active materials (CAMs).[48] Furthermore, thermodynamic analyses proved that chlorides generally have much better moisture stability than sulfides.[37] Compared to oxides and sulfides, halide chemistries offer a broader range of choices in structures, chemistries, and compositions for designing SEs with high ionic conductivities and good stabilities.

Thus far, the Li_3MCl_6 family (M = Sc, Y, In, Yb, Er, etc.) has been the most successful class of halide superionic conductors.[11] Ionic conductivities reaching ∼1 mS cm^{-1} at RT have been demonstrated for Li_3YCl_6 (trigonal, $P\bar{3}m1$, 0.51 mS cm^{-1}; hereafter, unless specified, conductivity values are at RT),[27] Li_3YbCl_6 (orthorhombic, $Pnma$, 0.14 mS cm^{-1}),[51,52] Li_3InCl_6 (monoclinic, $C2/m$, 1.49 mS cm^{-1}),[53] and Li_3ScCl_6 (monoclinic, $C2/m$, 3 mS cm^{-1}).[54] For successful design of halide SEs, selecting central metal cations with appropriate ionic sizes is critical for achieving the desired structures, such as hexagonal close-packed (hcp) trigonal and cubic close-packed (ccp) monoclinic structures.[55] The concentrations of the mobile-ion carriers (Li^+ or vacancy) can be tuned by aliovalent substitutions to further increase ionic conductivity.[56,57] Several promising materials design examples of halide SEs with enhanced ionic conductivities have been reported,[58] such as Zr^{4+}-substituted Li_3YCl_6 or Li_3InCl_6 and Fe^{3+}-substituted Li_2ZrCl_6 ($Li_{2.5}Y_{0.5}Zr_{0.5}Cl_6$, 1.40 mS cm^{-1}; $Li_{2.7}In_{0.3}Zr_{0.7}Cl_6$, 2.07 mS cm^{-1}; and $Li_{2.25}Zr_{0.75}Fe_{0.25}Cl_6$, 1 mS cm^{-1}).[49,59−61]

Notably, the mechanochemical preparation protocol plays a key role in the investigation of halide SEs. The low Li^+ conductivity of Li_3YCl_6 (0.01 mS cm^{-1}) prepared by conventional heat treatment (HT) is significantly improved by more than an order of magnitude to 0.51 mS cm^{-1} when prepared by ball-milling.[62] Previously, Li_3InCl_6 and Li_3InBr_6 were reported to show Li^+ conductivities of ∼0.01 and ≥1 mS cm^{-1}, respectively.[63−67] However, when prepared by ball-milling and subsequent HT at 260 °C, Li_3InCl_6 shows a high ionic
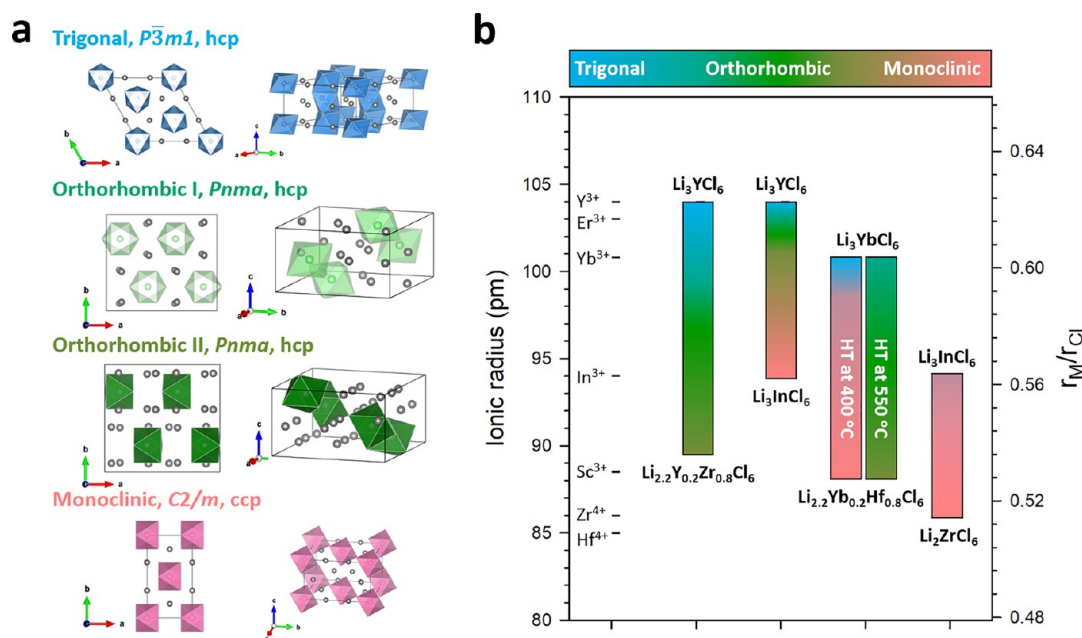
Figure 3. Structural evolution and corresponding Li⁺ conductivities of central-metal-substituted halide SICs. (a) Crystal structures outlined with the unit cells for trigonal, monoclinic, orthorhombic I and II Li_3MCl_6 (or Li_2MCl_6). Reproduced with permission from ref 51. Copyright 2021, Wiley-VCH. (b) Phase evolution of halide SEs, depending on the average ionic radius of central metals or ionic radius ratio of central metal to halide ion.

conductivity of 1.49 mS cm⁻¹.[53] Through pair distribution function (PDF) and X-ray diffraction (XRD) analyses, Schlem et al. suggested that the M2/M3 metal site disordering caused by the mechanochemical synthesis is the origin of the facile Li⁺ conduction in the ball-milling-prepared Li_3YCl_6.[62]

Thus far, the major research themes in halide SEs focus on exploring new compositions and structures. However, there have been few reports on the various issues and considerations for the practical applications of halide SEs in ASSBs, such as synthesis/processing protocols, cost, chemical stability, and large-scale ASSB fabrication. In this Review, we begin with a summary of the recent advances in halide SEs, including design strategies based on materials substitution, synthesis methods, and ion-transport mechanisms. The electrochemical stability and compatibility of halide SEs with electrode active materials are then reviewed, followed by the practical considerations for commercial ASSB usage of halide SEs, such as air/moisture stability, cost, and fabrication of sheet-type electrodes, in comparison with current state-of-the-art sulfide SEs. Finally, we offer a research outlook for addressing the challenges and issues emerging from the use of halide SEs in ASSBs.

STRUCTURE AND IONIC CONDUCTIVITY OF HALIDE SEs

Structure of Halide SEs. Among the ternary lithium halide SE systems, the Li_3MX_6 compounds (M = Sc, In, Er, Y, Ho, Yb, etc., X = Cl, Br) are the most common Li⁺ conductors that show high ionic conductivity (>0.1 mS cm⁻¹) at RT. All Li_3MX_6 halides have a close-packed anion sublattice with the M cations at the octahedral sites. The anion arrangements of these halide SEs can be categorized into hcp and ccp structures.[11,48] For the hcp anion sublattice, there are two distinct crystal structures, the trigonal structure of Li_3ErCl_6 (space group of $P\bar{3}m1$) and orthorhombic structure of Li_3YbCl_6 (space group of $Pnma$) (Figure 3a).[68] The Li_3MCl_6, with central metal M of Tb−Tm and Y with similar ionic radius of Er, has an hcp trigonal

structure, and Li_3LuCl_6 has an hcp orthorhombic structure as Li_3YbCl_6.[27,51,54] For ccp anion sublattice, there are spinel $Li_2Sc_{2/3}Cl_4$ (space group of $Fd\bar{3}m$) and monoclinic Li_3ErBr_6 (space group of $C2/m$). While Li_3MCl_6 chlorides can form either hcp anion sublattice (M = Er, Y, Yb, etc.) or ccp anion sublattice (M = Sc, In, etc.), all known Li_3MBr_6 bromides (M = Y, Sm−Lu) form the monoclinic structure with ccp anion sublattice ($C2/m$).[69] For iodides, Li_3ErI_6 exhibits a monoclinic crystal structure with the space group $C2/c$. By analyzing a large set of halide SEs on the basis of Pauling's rules of ion packing, Liang et al. summarized that the anion and cation sublattices (e.g., the arrangement and distributions of anions and cations) are determined by the ratio of ionic radii of cation M and anion X, $r_{M/X}$ (Figure 3b).[55] For $r_{M/X}$ values ranging from 0.599 to 0.637, halide SEs crystallize with hcp trigonal or orthorhombic structure. With increased $r_{M/X}$ values for reduced cation radii or increased anion radii, the crystalline structures convert to ccp anion sublattice, as observed in Li_3MCl_6 and Li_3MBr_6 (M = Er, Y). When the $r_{M/X}$ value is higher than 0.732, halide SEs tend to form a cubic structure which is similar to the CsCl structure.

Na⁺ halide SEs have different structural features compared to their Li⁺ counterparts. Li_2ZrCl_6 and Na_2ZrCl_6 exhibit highly distinctive structures.[49,70] While the ccp monoclinic structure of Li_2ZrCl_6 is due to the small ionic radius of Zr^{4+}, the hcp trigonal structure for Na_2ZrCl_6 can be explained by the larger ionic radius of Na⁺ (crystal ionic radius of 116 pm; hereafter, all the shown ionic radius values are the crystal ionic radii[71]) than that of Li⁺ (90 pm). Na⁺ halide SEs are reviewed in the section "Na⁺ Analogues of Halide SEs".

Design Principles and Factors for Fast Ionic Diffusion in Halide SEs. In Li_3MX_6 chlorides and bromides with hcp and ccp anion sublattices, Li⁺ ions occupy the octahedral (Oct) sites coordinated with six halogen anions, and the occupancy of the tetrahedral (Tet) sites is also reported in recent studies for heavily doped systems such as $Li_{3-x}M_{1-x}Zr_xCl_6$ (M = Y, In, Er, and Yb) and $Li_3YBr_3Cl_3$.[51,59−61,72] The hcp and ccp anion
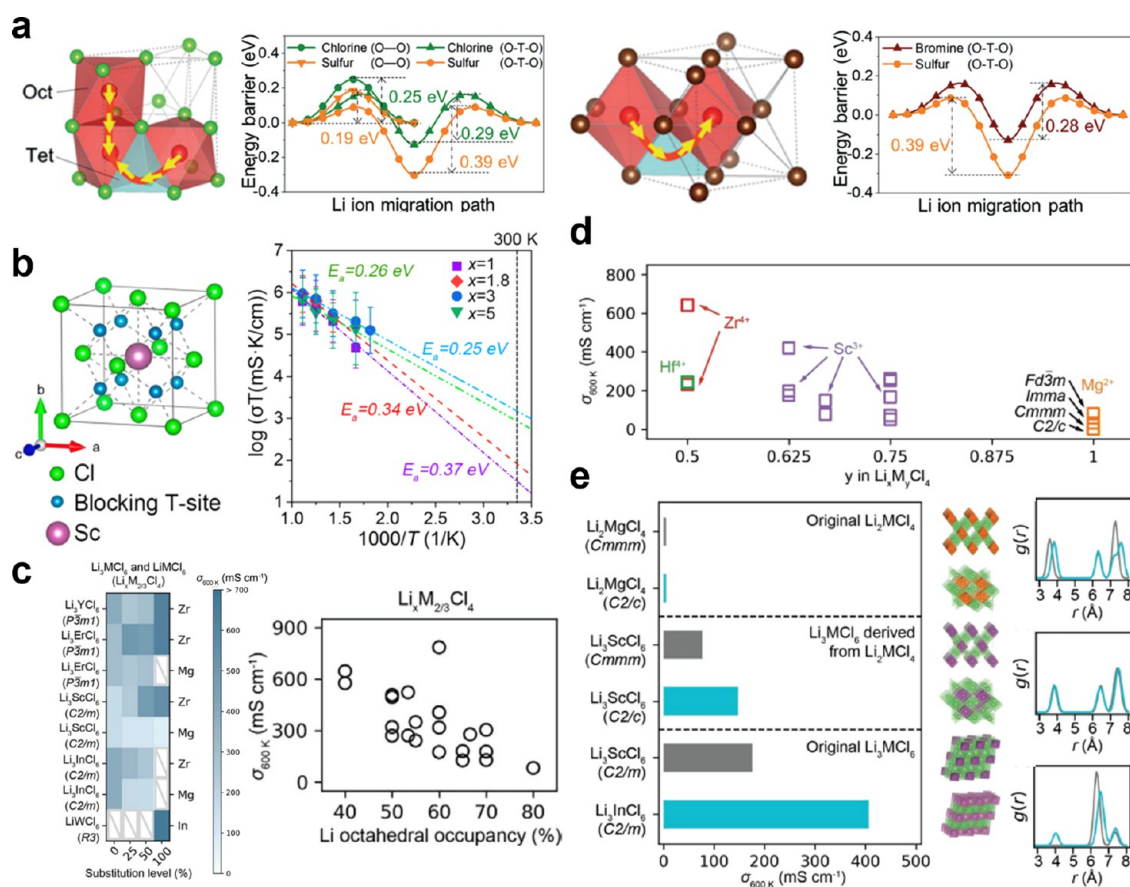
Figure 4. Computation studies for fast ion conduction in lithium halides. (a) Energy landscape of single Li^+ migration in fixed hcp (left) and ccp (right) anion lattice at volume per anion of S^{2-} (LGPS: 40.0 Å³), Cl^- (Li_3YCl_6: 37.4 Å³), and Br^- (Li_3YBr_6: 44.8 Å³), respectively. Reproduced with permission from ref 48. Copyright 2019, Wiley-VCH. (b) Cation blocking effect and its influence on Li^+ diffusivity in Li_xScCl_{3+x}. Reproduced with permission from ref 54. Copyright 2020, American Chemical Society. (c) Li^+ conductivities versus Li octahedral occupancy in a range of renormalized compositions $Li_xM_{2/3}Cl_4$ from AIMD simulation at 600 K. (d) Li^+ conductivities at 600 K as a function of M cation concentration y in hypothetical Li^+ conductors in $Li_xM_yCl_4$. (e) Hypothetical Li^+ conductors derived from Li_2MgCl_4 and Li_3MCl_6 materials, along with their crystal structures (right) and RDF $g(r)$ of M cations. Reproduced with permission from ref 73. Copyright 2020, Wiley-VCH.

sublattices result in distinct diffusion channels in the crystal structures.[27,48] In the ccp anion sublattice, Li^+ diffusion occurs through a 3D isotropic network where Li^+ ions hop between the Oct sites through the intermediate Tet sites (Oct-Tet-Oct). In the hcp anion sublattice, the Li^+ diffusion is anisotropic with one-dimensional (1D) diffusion channels, in which Li^+ ions hop among the adjacent face-sharing octahedral sites (Oct-Oct). These 1D channels are connected through Tet sites (Oct-Tet-Oct) to form a 3D diffusion network, and these fast 1D channels are susceptible to channel-blocking defects, such as anti-site defects, impurities, and grain boundaries. These different diffusion channels in the hcp and ccp anion sublattices lead to different ionic conductivities in halide SEs.

Using first-principles calculations, Wang et al. studied the energy landscape of single Li^+ migration in fixed hcp and ccp anion sublattices of Cl^-, Br^-, and S^{2-} with no M cations and revealed that chloride and bromide anion sublattices exhibit intrinsically low energy barriers for Li^+ migration.[48] The hcp Cl^-/Br^- anion sublattice at the lattice volume of Li_3YCl_6/Li_3YBr_3 shows a low diffusion barrier of 0.25 eV for the Oct-Oct pathway along the c-axis and 0.29 eV for Oct−Tet−Oct pathway within the ab-plane. The computation results for Li_3YCl_6 are in agreement with the experimental anisotropic activation energies of 0.18 and 0.25 eV. In addition, the ccp Cl^-/Br^- anion sublattice exhibits a low barrier of 0.28 eV for the Oct-Tet-Oct

pathway (Figure 4a) at the lattice volume of Li_3YCl_6/Li_3YBr_3. These intrinsic energy barriers for Li^+ migration in chlorides and bromides are significantly lower than 0.39 eV of the close-packed hcp/ccp S^{2-}-anion sublattice at the lattice volume of $Li_{10}GeP_2S_{12}$ (LGPS). In addition, the Li^+ migration barriers in chlorides and bromides are low for a wide range of lattice volumes of chloride/bromide materials. Compared to the divalent O^{2-} and S^{2-} anions, the monovalent Cl^- and Br^- anions have weaker Coulombic interactions with Li^+ ions, thus leading to a flatter potential energy landscape for ionic diffusion. In addition, Adelstein and Wood proposed that the chemical bond dynamics show intrinsic frustration, as revealed by the correlated fluctuations between cation−anion interactions with different degrees of directional covalent character in AIMD simulations, leading to increased Li^+ mobility.[66] In general, lithium-containing chlorides and bromides have energy landscapes with intrinsically low barriers for Li^+ diffusion in their common close-packed anion sublattices, whereas other anion chemistries, such as sulfides, require the rare bcc anion frameworks to achieve low migration barriers and to become SICs.

Given that close-packed anion sublattices are common for Li-containing chlorides and bromides, different Li/cation configurations and concentrations are the key factors in determining ion conductivities. Liu et al. performed a high-throughput

computation study on a wide range of chloride materials and revealed that the Li content and cation sublattice significantly affect Li^+ conduction.[73] In their high-throughput computation, they generated and studied a total of 74 chloride compounds with different Li contents through aliovalent substitution of 20 known chloride systems (Figure 4c). Comparing the Li^+ diffusion in these chlorides, they found that decreasing the Li contents generally increases Li^+ conductivities, which were attributed to greater availability of the octahedral sites for Li^+ hopping.[73] The analyses also found that Li content of approximately 40−60% of the octahedral site occupancy is optimal, and further lowering of the Li content would be detrimental to Li^+ diffusion. For Li_xMCl_6 (Figure 4c), substituting the M^{3+} cations by Zr^{4+} can reduce the Li content to form a number of SICs, including $Li_{5/2}Y_{1/2}Zr_{1/2}Cl_6$ ($P\bar{3}m1$), $Li_{11/4}Sc_{3/4}Zr_{1/4}Cl_6$ ($C2/m$), and $Li_{8/3}Y_{2/3}Zr_{1/3}Cl_6$ ($P\bar{3}m1$). Liu et al. further investigated the role of the cation M and found that lowering the cation concentration or having sparse cation distributions are beneficial for fast Li^+ conduction.[73] For the Li_3MCl_6 materials with the same composition but different cation sublattices, the sparse cation distributions, i.e., large cation−cation distances, generally lead to faster Li^+ diffusion than those materials with denser cation distributions (Figure 4e). By analyzing and comparing a wide range of chloride compounds and structures, the computation study revealed that Li_3MCl_6 has faster diffusion than Li_2MCl_4 (M = Mg, Mn, Cd, Zn, etc.) (Figure 4d), which are known to show low conductivities in experiments.[11,74−76] The poor Li^+ diffusion in the Li_2MX_4 spinel structures is caused by the blocking effect of M cations, as a result of the high concentration of M cations and denser M-cation distributions, which block the empty sites for Li hopping and cause high energy barriers for Li^+ migration. Based on these findings, Liu et al. concluded that (1) low Li content, typically between 40 and 60% of the available octahedron sites, (2) low cation concentration, and (3) sparse cation distribution are the three key factors for improving Li^+ conductivities in halide Li^+ conductors.[73]

The significant effect of cation concentration and configuration on Li^+ conduction is systematically illustrated in an experimental study by Liang et al.[54] In this study, a series of Li_xScCl_{3+x} compositions (x = 1, 1.5, 2, 2.5, 3, 3.5, and 4) were synthesized by tuning cation (Sc^{3+}) and Li^+ concentrations in a close-packed ccp anion sublattice. At a high cation concentration (low x), $LiScCl_4$ and $Li_{1.5}ScCl_{4.5}$ (x = 1, 1.5) showed a relatively high E_a of 0.39−0.40 eV and a relatively low ionic conductivity of 0.12−0.24 mS cm^{-1}, as the high concentration of Sc^{3+} blocks the surrounding Tet sites for Li^+ migration (Figure 4b) by Coulombic repulsion. The Li contents in these compounds are also low for optimal Li^+ diffusion, in agreement with the design principles proposed by Liu et al.[54,73] With the increase in x to 2, 2.5, and 3, the Sc^{3+} concentration in Li_xScCl_{3+x} is lowered, thus alleviating the cation blocking effects from Sc^{3+} ions while achieving the optimal range of Li content. As a result, the ionic conductivity increased to 3 mS cm^{-1} and E_a reduced to 0.36 eV. At higher x values of 3.5 and 4.0, the ionic conductivity decreased while E_a remained relatively low, as the increase in Li concentration decreased the available vacancy sites for Li^+ hopping. This trend of ion conduction for the series of Li_xScCl_{3+x} compositions agrees well with the computationally obtained design principles by Liu et al.[73] Similarly, the same design principles are also successfully applied to improve the Li^+ conduction in Li_2MCl_4 spinel, which are known to be poor Li^+ conductors. By lowering the M-cation concentration, Zhou et al.

achieved high ionic conductivity of ~1 mS cm^{-1} at RT in disordered-spinel $Li_2Sc_{2/3}Cl_4$.[77]

> Tuning the disordering of cation/anion sublattice is a promising strategy to further improve the ionic conductivity of lithium halide SEs.

Recent experiments on a wide range of new halide Li^+ conductors also confirm the significant roles of cation ordering, in agreement with computation analyses. Asano et al. reported the ionic conductivity of cold-pressed Li_3YCl_6 decreases after HT that improves the crystallinity.[27] It was found that the different synthesis and processing procedures determine the cation sublattice and ordering in hcp-Li_3MCl_6 (M = Er, Y, etc.) and result in distinct ionic conductivity. Hiroaki et al. reported that β-Li_3YCl_6 with disordered Y^{3+} sublattice shows higher ionic conductivity than α-Li_3YCl_6 with relatively ordered Y^{3+} sites.[78] Schlem et al. also reported the disordering of Er/Y sites in hcp-Li_3ErCl_6/Li_3YCl_6 in enhancing Li^+ conduction in samples prepared by mechanochemical synthesis.[62] These significant effects of cation ordering in ion conduction may explain the discrepancies between the values from AIMD simulations (14 mS cm^{-1} and 0.19 eV) with experimental measurements (0.51 mS cm^{-1} and 0.40 eV) for Li_3YCl_6. The discrepancies were also attributed to defects, such as Li-M anti-sites and grain boundaries, in the materials.[48] A recent computational study by Qi et al. reported a superionic transition above 425 K in Li_3YCl_6 indicating the extrapolated high-temperature Li^+ conductivity in AIMD simulations would overestimate the ionic conductivity, which also help explain the discrepancy with experimental measurements.[79]

All of these results suggest the significant role of the cation sublattice in determining high ionic conduction, in agreement with the computation study.[73] Furthermore, Liu et al. introduced the anion disordering in ccp-$Li_3YBr_3Cl_3$ by anion mixing and achieved a room-temperature conductivity of 7.2 mS cm^{-1}.[72] In a computation study by Zevgolis et al., the anion mixing of $Li_3InBr_{6-x}Cl_x$ was shown to tune the strain and bonding chemistry, thus further affecting activation energy and diffusivity.[67] The anion mixing has been successfully demonstrated in Li argyrodites Li_6PS_5X (X = Cl, Br, or I), in which the S^{2-}/X^- anion disordering gives rise to Li disordering and fast Li^+ conduction as revealed by Morgan et al.[80] Therefore, tuning the disordering of cation/anion sublattice is a promising strategy to further improve the ionic conductivity of lithium halide SEs. The effects of the structural disorder on ionic conductivity are discussed further in the section "Synthesis Methods of Halide SEs".

Substitution in Halide SEs. To discover novel halide SEs with improved ionic conductivity and (electro)chemical stability, lithium metal chloride ternary systems $LiCl−MCl_y−M'Cl_z$ have been explored via the substitution of the central metals, which changes the crystal structure according to the average ionic radius of the central metals. Park et al. reported Zr^{4+}-substituted Li_3MCl_6 ($Li_{3-x}M_{1-x}Zr_xCl_6$, M = Y, Er) with the structural evolution from trigonal to orthorhombic I and II structures, reaching the high ionic conductivity with the maximum of 1.4 mS cm^{-1} (Figure 5a,b).[59] As Zr^{4+} (r = 86 pm) substituted Er^{3+} (r = 103 pm) or Y^{3+} (r = 104 pm), the hcp trigonal structure was transformed to orthorhombic I structure ($x \geq 0.2$), which is isostructural with Li_3YbCl_6. Considering that
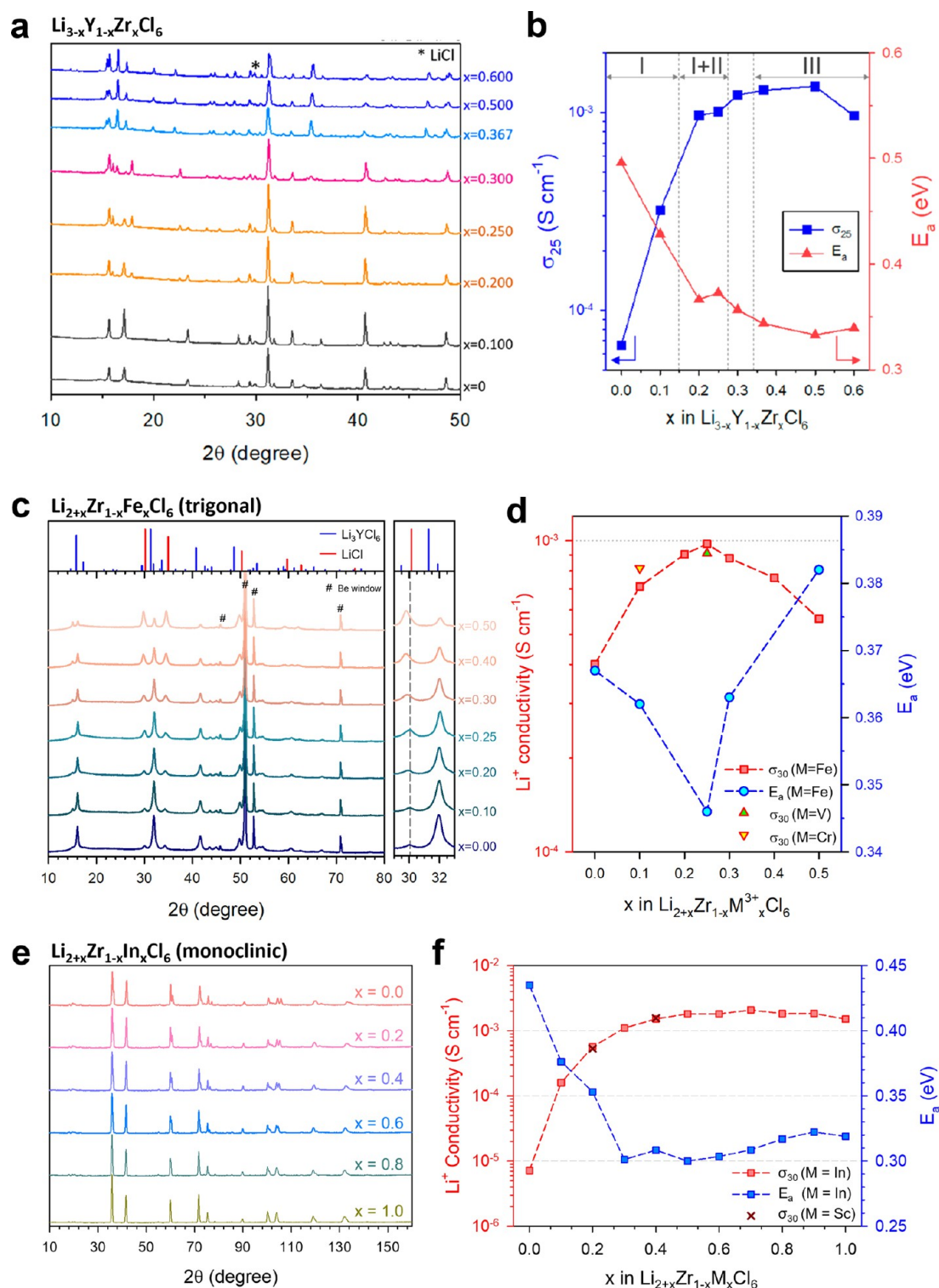
Figure 5. Structural evolution and corresponding Li^+ conductivities of central-metal-substituted halide SICs. XRD (or neutron diffraction) patterns and corresponding Li^+ conductivities with activation energies for (a, b) $Li_{3-x}Y_{1-x}Zr_xCl_6$, (c, d) $Li_{2+x}Zr_{1-x}M_xCl_6$ (M = Fe, V, Cr) prepared by mechanochemical method, and (e, f) $Li_{2+x}Zr_{1-x}M_xCl_6$ (M = In, Sc) prepared by HT. (a, b) Reproduced with permission from ref 59. Copyright 2020, American Chemical Society. (c, d) Reproduced with permission from ref 49. Copyright 2021, Wiley-VCH. (e, f) Reproduced with permission from ref 61. Copyright 2022, Wiley-VCH.

the average ionic radius of the central metals for $Li_{2.8}Er_{0.8}Zr_{0.2}Cl_6$ is 99.6 pm, the evolution of orthorhombic Li_3YbCl_6 phase (Yb = 100.8 pm) is revealed. Furthermore, a new solid-solution orthorhombic II phase emerged as more Er^{3+} or Y^{3+} was replaced by Zr^{4+} at $x > 0.4$. From the results of the time-of-flight neutron

diffraction and single-crystal XRD measurements, it was suggested that the new tetrahedral Li site created by the Zr^{4+} substitution facilitates Li^+ conduction in the orthorhombic II structure, reading a high ionic conductivity of 1.40 mS cm^{-1} in $Li_{2.5}Y_{0.5}Zr_{0.5}Cl_6$. The structural evolution and corresponding

modulation of ionic conductivities via central metal substitution were also observed in Zr^{4+} or Hf^{4+} (Hf^{4+} = 85 pm)-substituted Li_3YbCl_6.[51] With HT, $Li_{3-x}Yb_{1-x}M_xCl_6$ crystallized to monoclinic structures from trigonal at 400 °C and to orthorhombic II from orthorhombic I at 500 °C. Accordingly, Li^+ conductivities were significantly increased, reaching the maximum value of 1.50 mS cm^{-1} with the lowest activation energy of 0.26 eV for the $Li_{2.6}Yb_{0.6}Hf_{0.4}Cl_6$ prepared at 400 °C. Li et al. investigated the isovalent In^{3+} substitution in Li_3YCl_6.[58] The In^{3+} substitution resulted in a structural transformation from the hcp to ccp structure, and the ionic conductivities were enhanced to a maximum value of 1.42 mS cm^{-1} ($Li_3Y_{0.5}In_{0.5}Cl_6$). Moreover, the humidity tolerance was improved, which was ascribed to the formation of hydrated intermediates rather than the hydrolysis reaction. In-substituted $Li_2Sc_{2/3}Cl_4$ was also recently identified by Zhou et al.[50] In the solid solution range of 0 to 0.444 in

> The substitution of central metals and anions in halide SEs not only changes the structural framework but also tunes the distribution and concentration of Li^+ ions, as effective strategies to improve ionic conductivity.

$Li_2Sc_{2/3-x}In_xCl_4$, the cubic spinel structure of $Li_2Sc_{2/3}Cl_4$ was retained without the evolution of any noticeable impurity phases, with the corresponding Li^+ conductivities ranged from 1.83 to 2.03 mS cm^{-1}. However, at the higher x values ($\geq$0.555), In^{3+} was not incorporated into the cubic spinel structure of $Li_2Sc_{2/3}Cl_4$, and instead the monoclinic Li_3InCl_6 evolved with
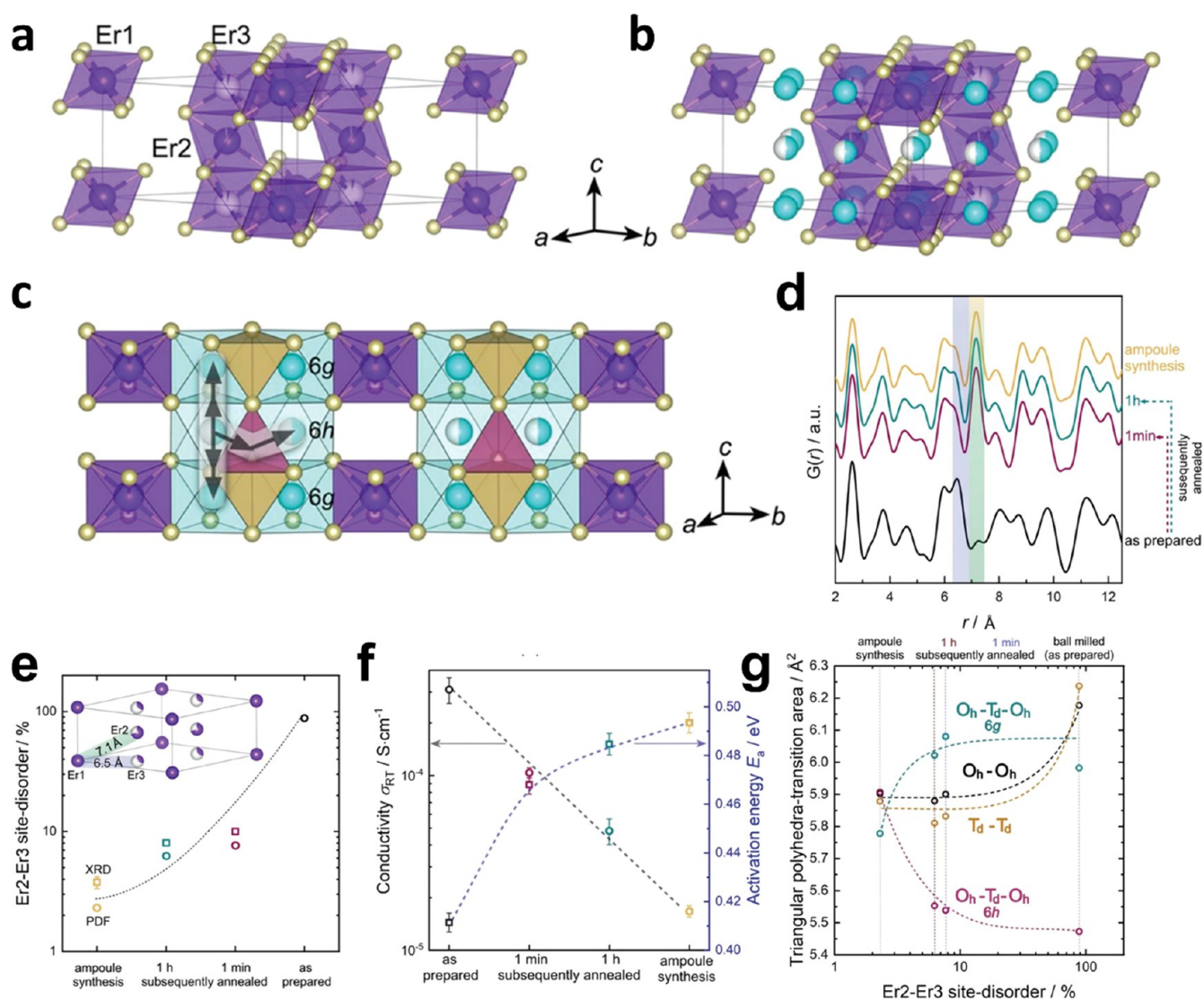

Figure 6. Structural evolution of M2/M3 metal site disordering in Li_3ErCl_6 prepared by mechanochemical synthesis. (a) Li_3ErCl_6 unit cell with the building units of $ErCl_6^{3-}$ octahedra that form a trigonal unit cell and face-sharing $ErCl_6^{3-}$ octahedra chains perpendicular to the (002) plane, with three possible Er sites (Er1, Wyckoff 1a; Er2 and Er3, Wyckoff 2d). (b) Li occupying the vacant octahedral sites (Wyckoff 6g, 100% occupied; Wyckoff 6h, 50% occupied). (c) Possible Li^+ pathways including face-sharing $LiCl_6^{5-}$ octahedra and a tetrahedral void. (d) Comparison of the PDF $G(r)$ of Li_3ErCl_6 samples prepared differently, (e) Er2−Er3 disorder determined by $G(r)$ fits (open circles) and Rietveld refinements (open squares), (f) ionic conductivities and corresponding activation barriers, and (g) different transition areas for possible Li^+ diffusion pathways. Reproduced with permission from ref 62. Copyright 2020, Wiley-VCH.

the formation of the LiCl impurity, owing to the preference of the ccp monoclinic structure by In^{3+} with larger ionic radius.

Recently, Kwak et al. reported two different types of Li_2ZrCl_6, the hcp trigonal Li_2ZrCl_6 (0.40 mS cm^{-1}) and ccp monoclinic Li_2ZrCl_6 (0.0057 mS cm^{-1}), prepared by mechanochemical method and HT at elevated temperature (260 °C), respectively.[49] To improve Li^+ conductivity of hcp trigonal Li_2ZrCl_6, tetravalent Zr in Li_2ZrCl_6 was substituted by trivalent metals, such as Fe^{3+}, Cr^{3+}, and V^{3+}. The solubility limit was $x = 0.25-0.30$ ($Li_{2+x}Zr_{1-x}Fe_xCl_6$), and Li^+ conductivity was significantly boosted from 0.40 to the maximum of ∼1 mS cm^{-1} at $x = 0.25$, which was attributed to the increased concentration and redistribution of Li^+ in the lattice (Figure 5c,d).[41,56,57,81−83] The aliovalent substitution was also effective in improving Li^+ conductivity of the ccp monoclinic Li_2ZrCl_6, which exhibited a much lower Li^+ conductivity (0.0057 mS cm^{-1}) compared to the isostructural Li_3InCl_6 (1.49 mS cm^{-1})[53] and Li_3ScCl_6 (3 mS cm^{-1}).[54] Kwak et al. and Helm et al. independently investigated the structural evolution and Li^+ distribution in M^{3+}-substituted ccp monoclinic Li_2ZrCl_6 ($Li_{2+x}Zr_{1-x}M_xCl_6$, M = In, Sc).[60,61] In Figure 5e, $Li_{2+x}Zr_{1-x}M_xCl_6$ exhibited a ccp monoclinic crystal structure with a $C2/m$ symmetry in this solid solution series over the entire range of x ($0 \leq x \leq 1$). Upon In^{3+} substitution, Li^+ conductivity was considerably increased up to 2.1 mS cm^{-1} (Figure 5f). The combined analysis of the Rietveld refinement of neutron diffraction and high-resolution synchrotron XRD measurements revealed that the insufficient amount of mobile charge carriers of Li^+ in Li_2ZrCl_6, compared to those in Li_3InCl_6 or Li_3ScCl_6, especially in the (002) plane, was the cause of low Li^+ conductivity in the monoclinic Li_2ZrCl_6. In summary, the substitution of central metals in halide SEs not only changes the structural framework through the average metal-ion radius but also tunes the distribution and concentration of Li^+ ions, as effective strategies to improve ionic conductivity.

In a similar manner to that of the central-metal substitution, anion substitution also changes the ratio of cation/anion ionic radii, $r_{M/X}$, and thus changes the crystal structure of halide SEs. Liu et al. reported that $Li_3YBr_3Cl_3$ prepared by ball-milling of trigonal Li_3YCl_6 and monoclinic-like Li_3YBr_6 exhibited a monoclinic single phase.[72] The $r_{M/X}$ value of $Li_3YBr_3Cl_3$, 0.596, is slightly below the lower limit for the hcp structure ($r_{M/X} = 0.605$ for Li_3LuCl_6). The crystal structure of halide SEs can also be affected by mobile-ion substitution. While the Li_3MCl_6 (M = Y, Tb−Lu) has a trigonal structure, a series of elpasolite compounds ($A_2^+B^+M^{3+}X_6$: Cs_2LiYCl_6, and Cs_2NaYCl_6) wherein mobile ions are substituted with Cs^+ showed a cubic structure.[84,85] These phase transitions can be explained by the larger ionic radius of Cs^+ (181 pm) compared to that of Li^+ (90 pm).

Synthesis Methods of Halide SEs. For preparing ceramic materials, popular techniques include conventional high-temperature solid-state reactions, melt-quenching, co-precipitation, mechanochemistry, and gas-phase reaction methods. Among them, solid-state reactions and the mechanochemical method have been commonly used to synthesize halide SEs.[11] The preparation methods greatly influence the crystal structure, particularly the structural disorder and metal distributions, and thus significantly impact ionic conductivity. Notably, the mechanochemical method could generate unique phases of SEs that could not be obtained by other methods.[86−89] While SEs prepared at high temperatures produce thermodynamically stable phases, the mechanochemical method commonly generates amorphous and/or nanocrystalline phases, which are often unique metastable phases. The widely investigated mechanochemically derived glass and/or glass-ceramic sulfide SEs could be a good benchmark for the development of halide SEs.[16,90−94] Specifically, the argyrodite sulfide SEs having the general formula $Li_{7+x-y}M_x^{4+}M_{1-x}^{5+}S_{6-y}X_y$ (M^{4+} = Si, Ge, Sn; M^{5+} = P, Sb; X = Cl, Br, I; $0 \leq x \leq 1$; $0 \leq y \leq 2$; e.g., Li_6PS_5Cl) are an interesting example. Li^+ conductivities of Li_6PS_5I were enhanced by 2 orders and 1 order of magnitude when prepared by a mechanochemical method and by a solution process, respectively, which was explained by the increased local structural disorder and distortion.[93,94] In addition, it was shown that sulfide/halide anion site disorder and Li site disorder are the key factors for the ionic conduction in argyrodite sulfide SEs.[80,95] The mechanochemical synthesis method is also gaining importance for the development of highly conductive halide SEs, and the underlying local structural evolution emerges as an important research topic.[27,49,62,96]

The Li^+ conductivity of highly crystalline Li_3YCl_6 synthesized by conventional solid-state synthesis at high temperatures was as low as 0.01 mS cm^{-1}.[27,62] On the other hand, mechanochemically synthesized Li_3YCl_6 exhibited a much higher Li^+ conductivity of 0.51 mS cm^{-1}.[27,62] The mechanochemically prepared samples exhibit low crystallinity and/or structural disorder and may include amorphous phases, and as a result conventional XRD analysis cannot offer complete structural information. In the study by Schlem et al., the crystal structures and ion conduction mechanisms of Li_3MCl_6 (M = Y, Er) prepared using various synthesis methods were investigated and analyzed by PDF and XRD measurements (Figure 6).[62] Li_3MCl_6 (M = Y, Er) exhibited a trigonal crystal structure ($P\bar{3}m1$) with three kinds of MCl_6 octahedra (Figure 6a−c), such as the M1 (Wyckoff position 1a), M2 (Wyckoff position 2d), and M3 (M2-equivalent position in the (001) plane) sites. For the highly crystalline Li_3ErCl_6 prepared at high temperatures, the M1 and M2 sites were mostly occupied, and the M3 site (which is the disordered position of the M2 site) was largely unoccupied. In contrast, for mechanochemically prepared nanocrystalline Li_3ErCl_6, an M2/M3 site disordering was observed, and the ratio of M3 to M2 sites increased significantly upon mechanical milling. When the mechanochemically prepared samples were subjected to HT, the M2/M3 site disordering decreased along with the increased crystallinity, which might account for the lowered Li^+ conductivity (Figure 6e,f). The structure of the highly crystalline Li_3ErCl_6 with the fully occupied M2 site led to a higher Li^+ migration barrier along the c-axis owing to the higher repulsive force of the M2 sites. In contrast, the M2/M3 site disordering derived via the mechanochemical process lowered the migration barrier along the c-axis by weakening the repulsion force. Furthermore, the M2/M3 site disordering also reordered the Li^+ sublattice, facilitating Li^+ diffusion. Specifically, in the four distinct polyhedral transition areas for Li^+ migration, noticeable changes were observed (Figure 6g), which likely affected the Li^+ occupancies as a result of Coulombic repulsion.

The M2/M3 site disordering achieved using the mechanochemical method was also observed in hcp trigonal halide SEs.[49,70] Similar to Li_3YCl_6, Na_2ZrCl_6 exhibited a much higher Na^+ conductivity in the mechanochemically synthesized samples (BM-Na_2ZrCl_6: 1.8 × 10^{-5} S cm^{-1}) than in the heat-treated samples (HT-Na_2ZrCl_6: 6.9 × 10^{-8} S cm^{-1}).[70] In HT-Na_2ZrCl_6, the Zr1 and Zr2 sites exhibited 100% occupancy without any disordering, and Na^+ existed only at the Na1 site in the (001)
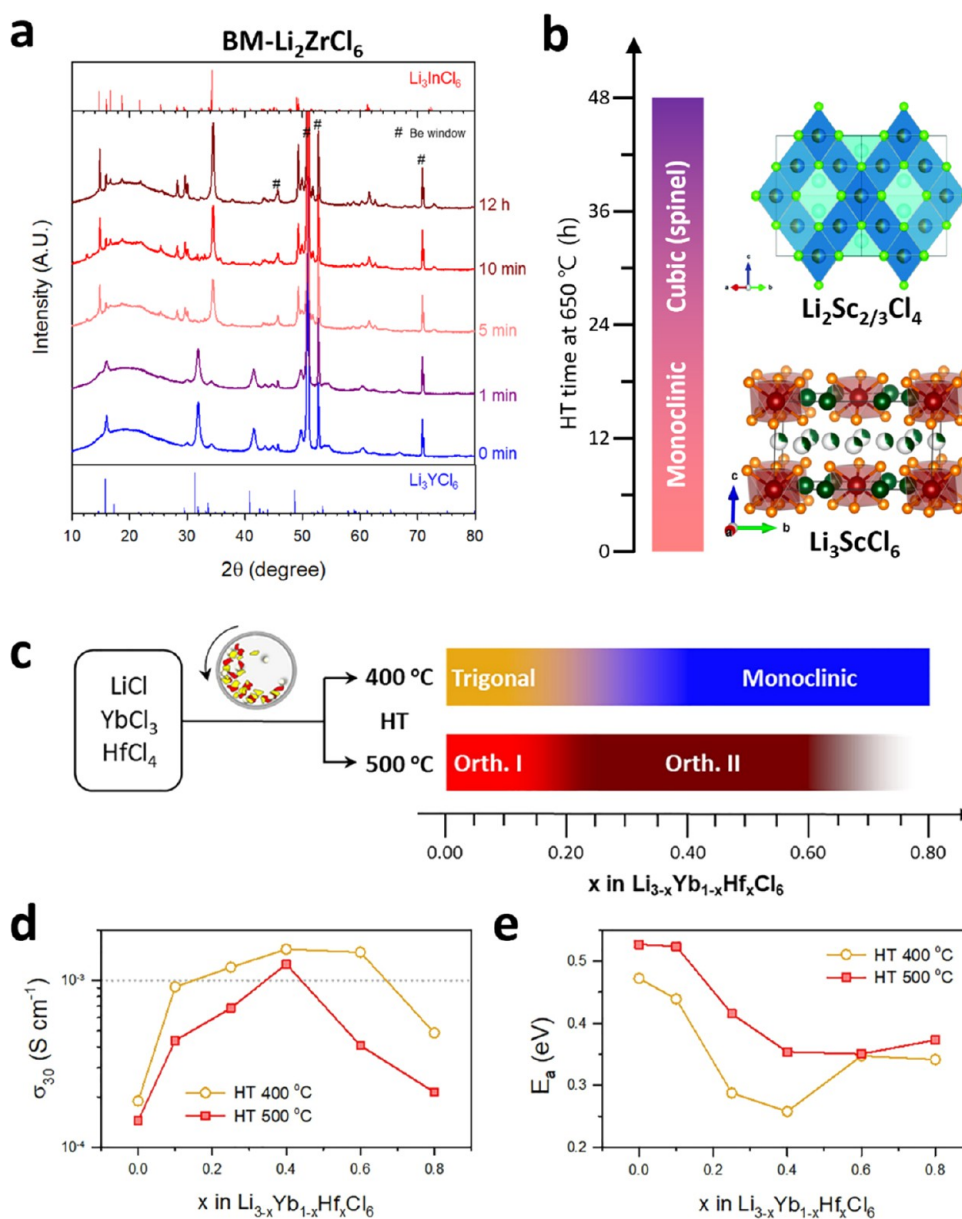
Figure 7. Structural evolution and corresponding Li^+ conductivities upon HT condition of representative halide SEs. (a) XRD patterns of BM-Li_2ZrCl_6 upon HT at 260 °C. Reproduced with permission from ref 49. Copyright 2021, Wiley-VCH. (b) Schematic of the phase evolutions of Li-Sc-Cl upon HT at 650 °C, as a function of HT time variations. Reproduced with permission from ref 54. Copyright 2020, American Chemical Society. Reproduced with permission from ref 77. Copyright 2020 the Royal Society of chemistry (c) Schematic of the phase evolutions upon Hf^{4+} substitution of Li_3YbCl_6 prepared at 400 or 500 °C. (d) Li^+ conductivities at 30 °C, and (e) corresponding activation energies for $Li_{3-x}Yb_{1-x}Hf_xCl_6$. Reproduced with permission from ref 51. Copyright 2021, Elsevier.

plane. In the (002) plane, the Zr2 site was fully occupied, and the Na^+ occupancy at the Na^+ interstitial sites that forms Na^+ migration channels along the *c*-axis was zero, which might explain the poor Na^+ conduction in HT-Na_2ZrCl_6. In contrast, the mechanochemical method would result in disordering of the Zr and Na sites in the halide structures, leading to the partial occupation of the Na interstitial sites and the formation of Na^+ migration channels for the significantly enhanced Na^+ conductivity. Furthermore, Kwak et al. revealed that the mechanochemically synthesized Li_2ZrCl_6 has an hcp trigonal structure and M2/M3 site disordering, as verified by the PDF analysis, as is the case for Li_3YCl_6.[49]

As an intriguing example, Li_2ZrCl_6 can crystallize into two different structures depending on the synthesis method (Figure

7a).[49] Since Zr^{4+} (86 pm) has a similar ionic radius to Mg^{2+} (86 pm)[74,75] and Sc^{3+} (88.5 pm),[54,77] Li_2ZrCl_6 is expected to form a disordered spinel or monoclinic structure, whereas Y^{3+} (104 pm), with a larger radius, forms hcp trigonal Li_3YCl_6. The ccp monoclinic structure of Li_2ZrCl_6 prepared by HT can thus be understood according to its ionic radius. In contrast, Li_2ZrCl_6 prepared by the mechanochemical method unexpectedly crystallizes into the hcp trigonal structure. However, upon annealing at 260 °C for only a few minutes, the mechanochemically prepared sample with the hcp trigonal structure exhibits a phase transition to the ccp monoclinic structure (Figure 7a). This phase transition indicates that the hcp trigonal structure derived from mechanochemical method is a metastable phase.[49]
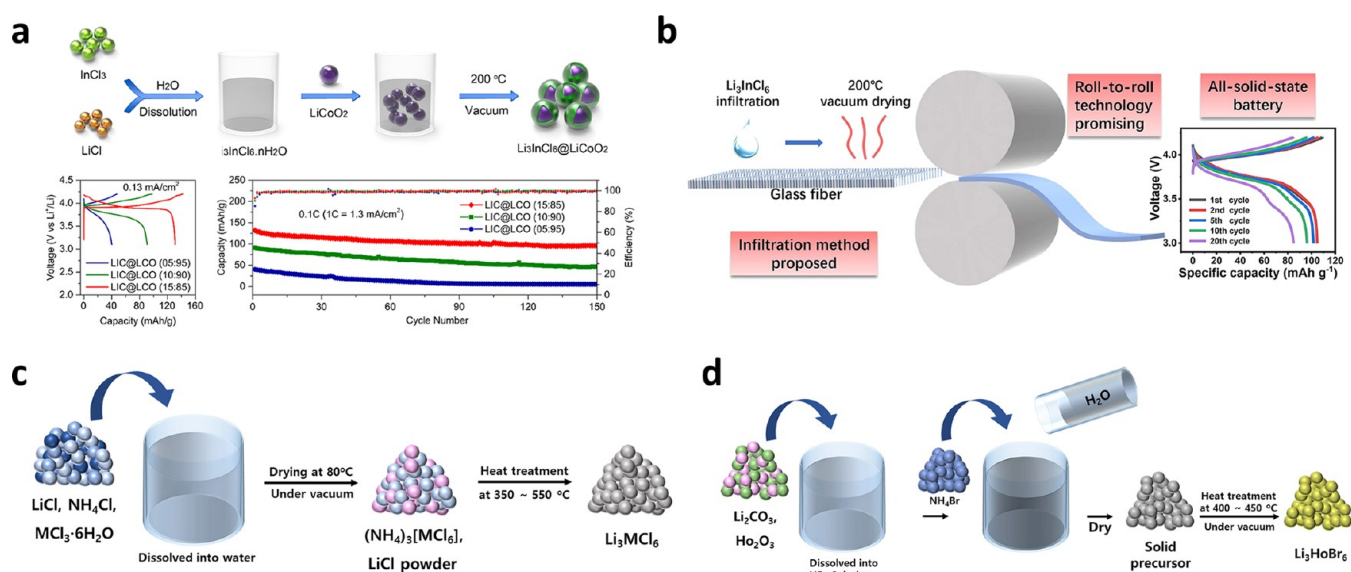
Figure 8. Wet-chemical syntheses of halide SEs. (a) Schematic of the in situ synthesis of Li_3InCl_6 for the coatings on $LiCoO_2$ (LIC@LCO), initial charge−discharge curves of LIC@LCO electrodes, and the corresponding cycling stabilities. Reproduced with permission from ref 115. Copyright 2020, Elsevier. (b) Schematic of the infiltration method for Li_3InCl_6/glass-fiber solid composite electrolyte film and the corresponding charge−discharge curves. Reproduced with permission from ref 116. Copyright 2022, Elsevier. (c) Schematic illustrating the ammonium-assisted synthesis method of halide SEs. (d) Schematic illustrating the HBr-assisted synthesis method of Li_3HoBr_6.

Flores-González et al. investigated structures, thermal stabilities, and electrochemical characteristics of mechanochemically prepared $LiAlX_4$ (X = Cl, Br, I).[88] Interestingly, while $LiAlI_4$ could not be synthesized by conventional HT, it could be prepared mechanochemically. $LiAlBr_4$ and $LiAlI_4$ were isostructural to $LiAlCl_4$ according to synchrotron and neutron diffraction results.

The HT condition is an important factor for achieving the desired structure and ionic conductivity of halide SEs, similar to the observation for sulfide SEs such as the $Li_2S-P_2S_5$ binary system.[97] Ito et al. investigated the kinetically stable metastable phase of Li_3YCl_6 using in situ XRD while heating of a mixture of LiCl and YCl_3 powders.[78] In the metastable β-Li_3YCl_6 synthesized below 600 K and the stable α-Li_3YCl_6 synthesized above 600 K, an hcp structure was observed for the Cl^- arrangement. While Y could occupy three different Wyckoff positions in α-Li_3YCl_6, all of the Y sites are identical in β-Li_3YCl_6 due to the Y site disordering along the c-axis. The disordering of Y sites in β-Li_3YCl_6 increases the Li^+ conductivity, similar to the effect of M2/M3 site disordering observed in the mechanochemically prepared Li_3ErCl_6. It was postulated that the disorder along the c-axis leads to the flattening of the energy landscape of Li^+ along the c-axis.[62] Furthermore, different phase evolutions could also occur, depending on the HT time. Recently, Liang et al. and Zhou et al. independently reported on Sc-based halide SEs prepared by HT at 650 °C, wherein different crystal structures were observed for the same chemical composition upon varying the HT time (Figure 7b); monoclinic Li_3ScCl_6 (max. 3 mS cm^{-1})[54] and disordered spinel $Li_2Sc_{2/3}Cl_4$ (1.5 mS cm^{-1})[77] were synthesized by heating for 12 and 48 h, respectively. Given the similarities in the ionic radii of Sc^{3+} (88.5 pm) and the divalent metals such as Mg^{2+} (86 pm), the formation of Sc-based halide SEs in a disordered spinel structure may be expected. The occurrence of the two different crystal structures for the same composition implies a subtle difference in their formation energies.

Park et al. recently revealed the dynamic structural evolutions of Hf^{4+} or Zr^{4+}-substituted Li_3YbCl_6 as a function of HT temperature variations (Figure 7c−e).[51] The unsubstituted Li_3YbCl_6 synthesized at 400 and 500 °C crystallized with trigonal and orthorhombic I structures, respectively. The aliovalent substitution of Yb^{3+} with the tetravalent Hf^{4+} and Zr^{4+} metal ions led to phase transitions from trigonal to monoclinic for HT at 400 °C and from orthorhombic I to orthorhombic II for HT at 500 °C (Figure 7c). Compared to the orthorhombic II phase prepared at 500 °C, the monoclinic phase prepared at 400 °C showed higher Li^+ conductivities and lower activation energies over the entire composition range (Figure 7d, e). The highest Li^+ conductivity of 1.5 mS cm^{-1}, with the lowest activation energy of 0.26 eV, was obtained for $Li_{2.60}Yb_{0.60}Hf_{0.40}Cl_6$. Further, Zr^{4+}-substituted Li_3YCl_6 formed different phases upon varying the HT temperature.[51,59] While $Li_{2.5}Y_{0.5}Zr_{0.5}Cl_6$ prepared at 200 °C had a trigonal structure, the orthorhombic II phase emerged at 400 °C, which exhibited slightly decreased Li^+ conductivities and increased activation energies.

Wet-chemical synthesis may be beneficial for the mass production of SEs, thanks to its reduced processing time and efforts for precursor mixing.[9,98−100] Solvent-mediated soft chemistry may also create novel metastable materials that would otherwise be inaccessible.[86,101−103] For cell fabrication, solution-processing enables direct SE coatings on electrode active materials and also allows the fabrication of sheet-type electrodes and SE membranes with intimate ionic contacts by infiltration.[38−40,86,94,104−110] While these techniques have been widely investigated for sulfide SEs, the development of wet syntheses for halide SEs has been limited. Known examples are the synthesis of Li_3InCl_6 using water, Li_3YCl_6 using NH_4Cl as a coordination agent, and Li_3HoBr_6 using a vacuum-evaporation-assisted (VEA) method.[53,111−113]

Li et al. reported an important chemical feature of Li_3InCl_6: i.e., the crystal structure and ionic conductivity of Li_3InCl_6 exposed to humid air (30% humidity) can be mostly recovered

to the original state upon heating at 260 °C.[53] Using X-ray absorption near edge structure (XANES), Raman, and synchrotron XRD, they revealed that Li_3InCl_6, which is hydrophilic in nature, rather than undergoing hydrolysis, reacted with the water in air to generate $Li_3InCl_6 \cdot xH_2O$ with trace amounts of In_2O_3, LiCl, and HCl.[114] Upon heating, $Li_3InCl_6 \cdot xH_2O$ returned to Li_3InCl_6 without undergoing oxidation. Furthermore, $Li_3InCl_6 \cdot xH_2O$ was generated by reacting LiCl and $InCl_3$ in water, and Li_3InCl_6 could be obtained by heating at 200 °C (Figure 8a).[111] Notably, the solution processing of Li_3InCl_6 using water allowed the direct coating of Li_3InCl_6 on $LiCoO_2$ for $LiCoO_2$/Li-In ASSB cells (Figure 8a).[115] The halide SE coating provides a higher ionic conductivity than conventional oxide cathode coatings and a higher electrochemical oxidation stability than sulfide SEs, resulting in good electrochemical performances of ASSB cells. At 0.1C, $LiCoO_2$ coated with 15 wt% Li_3InCl_6 showed an initial capacity of 131.7 mA h g^{-1} and could be operated up to 4C at RT. Furthermore, infiltration using Li_3InCl_6 solution could also be applied for producing Li_3InCl_6/glass-fiber solid composite electrolyte films with good mechanical strength and a high ionic conductivity of 0.54 mS cm^{-1} (Figure 8b).[116]

However, among chloride (and bromide) SEs, Li_3InCl_6 has been the only SE that can be prepared by wet-synthesis (or process) using pure water. The other chloride SEs exhibit hydrolysis reactions to form metal oxides or metal oxychlorides upon heating (Table 2), and the poor water stabilities make
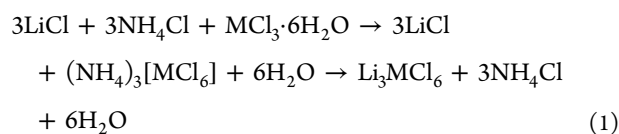
Table 2. Hydrolysis Reaction of Metal Halides

| metal halide	hydrate form	products after heat treatment
YCl_3	$YCl_3 \cdot 6H_2O$	MOCl or M_2O_3 (M = Y, Sc, La−Lu)
$ScCl_3$	$ScCl_3 \cdot xH_2O$	
$InCl_3$	$InCl_3 \cdot xH_2O$	major: $InCl_3$
		minor: In_2O_3
$ZrCl_4$	−(hydrolysis)−	$ZrOCl_2$, ZrO_2

them inaccessible for wet-synthesis using water.[117−119] To achieve the wet-synthesis of alternative halide SEs, it is essential that the formed intermediate species do not produce an oxidized product upon heating (Table 3).[117] Motivated by the industrial "ammonium chloride route" to produce metal chlorides, Wang et al. synthesized various halide SEs, such as Li_3YCl_6, Li_3ErCl_6, and Li_3ScCl_6 (eq 1, Figure 8c), through[112]

Table 3. Synthesis Routes for Anhydrous Metal Halides

reagents	chemical reaction
NH_4Cl	$12(NH_4)Cl + Y_2O_3 \rightarrow 2(NH_4)_3[YCl_6] + 6NH_3 + 3H_2O$
	$6(NH_4)Cl + 2YCl_3 \cdot 6H_2O \rightarrow 2(NH_4)_3[YCl_6] + 3H_2O$
	$12(NH_4)Cl + 2Y \rightarrow 2(NH_4)_3[YCl_6] + 6NH_3 + 3H_2$
	$2(NH_4)_3[YCl_6] \rightarrow (NH_4)[Y_2Cl_7] + 5(NH_4)Cl \rightarrow 2YCl_3 + 6(NH_4)Cl$
$SOCl_2$	$MCl_n \cdot xH_2O + xSOCl_2 \rightarrow MCl_n + xSO_2 + 2xHCl$
CCl_4	$Ln_2O_3 + 3CCl_4 \rightarrow 2LnCl_3 + 3Cl_2 + 3CO$
	$MO_2 + 2CCl_4 \rightarrow MCl_4 + 2COCl_2$ (M = Zr, Hf)

$$3LiCl + 3NH_4Cl + MCl_3 \cdot 6H_2O \rightarrow 3LiCl$$
$$+ (NH_4)_3[MCl_6] + 6H_2O \rightarrow Li_3MCl_6 + 3NH_4Cl$$
$$+ 6H_2O \qquad (1)$$

When LiCl and the metal halide were reacted in water in the presence of NH_4Cl, $(NH_4)_3[MCl_6]$ could be obtained as an intermediate species. Upon heating at elevated temperatures, $(NH_4)_3[MCl_6]$ was not oxidized or hydrolyzed, and the desired halide SEs could be obtained. Li_3HoBr_6 could be synthesized on a gram scale using a new VEA method, which has the advantage of using relatively inexpensive precursors such rare earth metal (REM) oxides, lithium carbonates, and ammonium halides (eq 2, Figure 8d).[113]

$$3Li_2CO_3 + Ho_2O_3 + 12NH_4Br$$
$$\rightarrow 2Li_3HoBr_6 + 3CO_2 + 12NH_3 + 6H_2O \qquad (2)$$
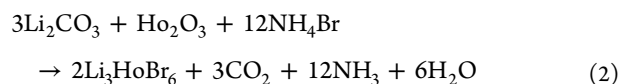
The key to the underlying mechanism was the formation of an intermediate product by reaction with NH_4Br. Because the wet-chemical syntheses/processes discussed thus far are based on water and could produce halide SEs with high ionic conductivities and electrochemical oxidation stability at the same time, they have the potential for scalable preparation of halide ASSBs. However, the low pH (or acidity) of the halide solutions remains a challenge to be addressed, which can cause damages to the exterior packages, manufacturing equipment and facilities, and the electrode components, including active materials and/or the current collectors.[111]

Na$^+$ Analogues of Halide SEs. Compared to Li$^+$ halide SEs, fewer types of Na$^+$ halide SEs have been reported. Park et al. computationally investigated a series of Na_3MCl_6 SEs with three structures, i.e., trigonal $P\bar{3}m1$, trigonal $R\bar{3}$, and monoclinic $P2_1/n$.[120] Similar to Li$^+$ halide SEs, Na_3MCl_6 SEs possessed good oxidation stability and interfacial compatibility with cathodes, and the formation of vacancies by aliovalent substitution also enhanced the ionic conductivity of Na_3MCl_6 SEs, as in their Li counterparts. While computational studies predicted Na$^+$ halide SEs with high ionic conductivities,[120,121] only three Na$^+$ halide SEs have thus far been experimentally identified with Na$^+$ conductivities over 10^{-5} S cm^{-1} (Figure 9): the ccp monoclinic [$P2_1/n$, $Na_{3-x}Er_{1-x}Zr_xCl_6$ (0.04 mS cm^{-1}),[122] and $Na_{3-x}Y_{1-x}Zr_xCl_6$ (0.066 mS cm^{-1})][123] and hcp trigonal [$P\bar{3}m1$, Na_2ZrCl_6 (0.018 mS cm^{-1})].[70] $Na_{3-x}Er_{1-x}Zr_xCl_6$ and $Na_{3-x}Y_{1-x}Zr_xCl_6$ showed the same ccp monoclinic structure, owing to the similar ionic sizes of Er^{3+} (103 pm) and Y^{3+} (104 pm), as the Li counterparts Li_3ErCl_6 and Li_3YCl_6 showed the same hcp trigonal structure. However, it was noted that the Na$^+$ halide SEs crystallize differently from their Li$^+$ counterparts. The simple $r_{M/X}$ rule for Li$^+$ halide SEs does not apply for the Na$^+$ halide SEs. Na_3ScCl_6 (Sc^{3+}: 88.5 pm) and Na_3YCl_6 (Y^{3+}: 104 pm) showed the same structure (monoclinic, $P2_1/n$) despite the large difference in the ionic size of their central metal atoms.[124] On the other hand, Na_3InCl_6 (94 pm), comprising In^{3+} with a radius value between those of Sc^{3+} and Y^{3+}, showed a crystal structure (trigonal, $P\bar{3}m1$) different from that of Li_3InCl_6 (ccp monoclinic, $C2/m$).[125] $Na_{3-x}M_{1-x}Zr_xCl_6$ (M = Y, Er) showed the ccp monoclinic structure ($P2_1/n$) for the entire range of the composition, except for the end member Na_2ZrCl_6 (Figure 9a,b), which had a trigonal ($P\bar{3}m1$) space group (Figure 9h,i) analogous to Li_3ErCl_6. The much larger ionic radius of Na$^+$ (116 pm) than that of Li$^+$ (90 pm) likely causes the differences in the crystal structures.
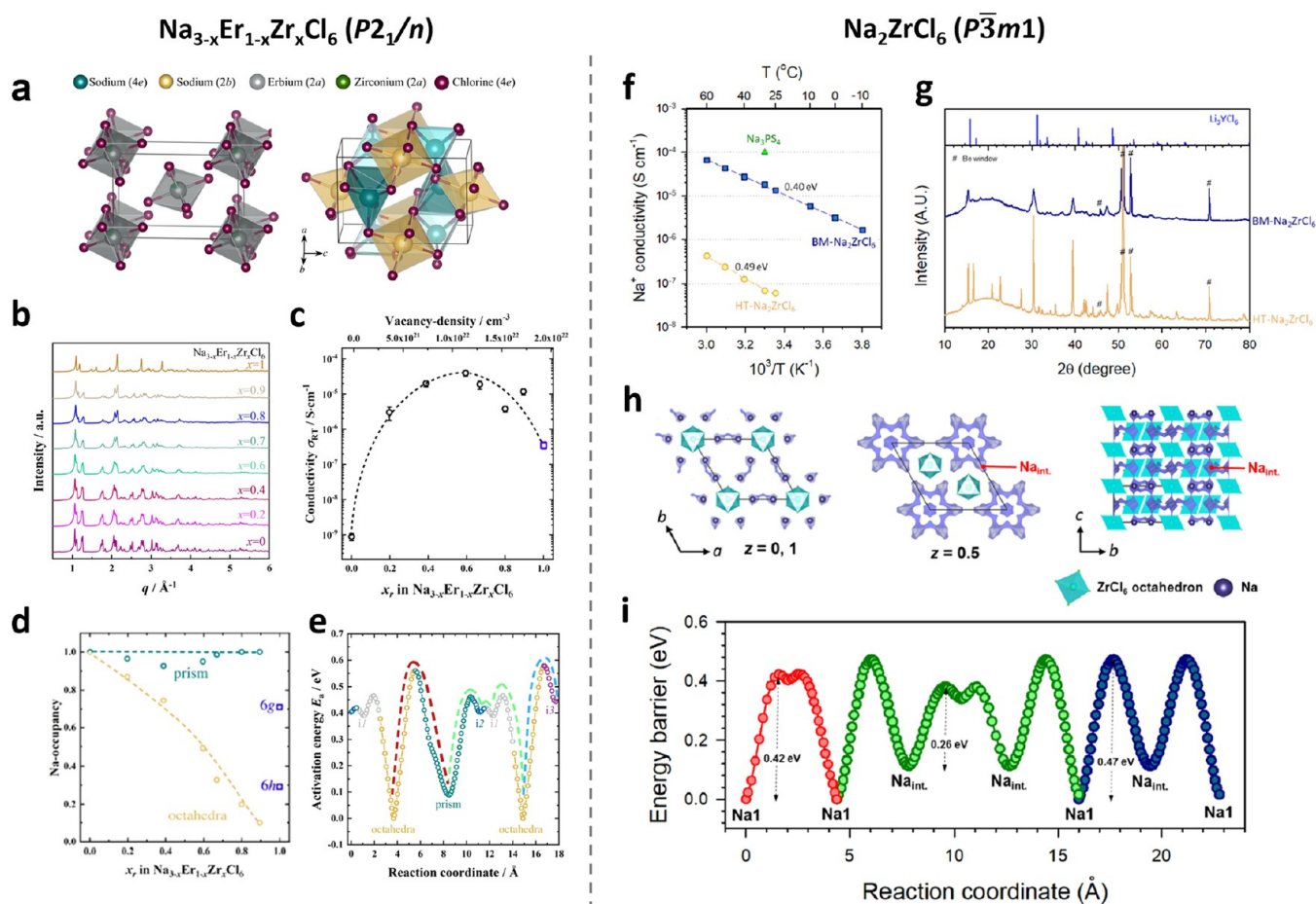
Figure 9. Crystal structures and Na⁺ conduction pathways for Na⁺ halide SEs. (a) Na₃ErCl₆ structure built in a bcc-like arrangement of ErCl₆³⁻ octahedra and two different Na polyhedra that were found to be either prisms or octahedra, being linked by either a corner or an edge. (b) XRD patterns for Na₃₋ₓErₓ₋ₓZrₓCl₆ showing that the full-substitution series crystallizes in the $P2_1/n$ space group except for Na₂ZrCl₆. (c) Na⁺ conductivity for Na₃₋ₓErₓ₋ₓZrₓCl₆. (d) Na Wyckoff positions exhibiting Na occupancies. (e) Energy landscape diagram of Na⁺ diffusion for Na₂.₈Er₀.₈Zr₀.₂Cl₆, obtained by the BVEL calculations. Reproduced with permission from ref 122. Copyright 2020, American Chemical Society. (f) Arrhenius plots of Na⁺ conductivity and (g) powder XRD patterns for BM- and HT-Na₂ZrCl₆ ($P\bar{3}m1$). (i) Na⁺ diffusion paths and (j) energy landscape diagram for HT-Na₂ZrCl₆, obtained by the BVEL calculations. Reproduced with permission from ref 70. Copyright 2021, Elsevier.

Similar to Li⁺ halide SEs, aliovalent substitution of Na₃MCl₆ SEs is also employed to enhance the ionic conductivity. In the Zr⁴⁺-substituted Na₃ErCl₆, only Na atoms in the octahedral Na site were removed to create Na vacancies in the prismatic and octahedral sites. The authors suggested that this occurred even though the aliovalent substitution of Er³⁺ with Zr⁴⁺ decreased the activation energy and increased Na⁺ conductivity owing to the vacancy-driven Na⁺ conduction (Figure 9c−e). The bond valence energy level (BVEL) calculations of Na₂ZrCl₆ revealed that an interstitial octahedral site bridged the Wyckoff 6g Na sites along the *c*-axis, which facilitated the Na⁺ migration along the *c*-axis (Figure 9h,i).[70]

Similar to the Li⁺ counterparts,[49,51,54,77] the preparation method affected the structure and ionic conductivities of Na⁺ halide SEs.[70,122,123] For Na₂ZrCl₆ and Na₃₋ₓY₁₋ₓZrₓCl₆, the Na⁺ conductivities for the samples prepared by mechanical milling were several orders of magnitude higher than those prepared by HT (Figure 9f). For mechanisms similar to those used with the Li⁺ halides discussed in the section "Na⁺ Analogues of Halide SEs", the structural disorder may have rendered more favorable sublattices for Na⁺ conduction.[62,87]

■ HALIDE SEs FOR ALL-SOLID-STATE BATTERIES

Halide SEs bring together the combined advantages of sulfide and oxide SEs, that is, the mechanical sinterability and excellent electrochemical oxidation stability, and thus are among the best candidates for achieving high-energy ASSBs with at-scale manufacturing. The poor electrochemical reduction stability of halide SEs prevents their use with current major anodes such as Li metal, graphite, and Si, and multiple SEs could be applied in a single ASSB cell to mitigate the stability issue at the anode interface while maintaining the exceptional advantage of halide SEs for catholytes.

Intrinsic Electrochemical Stability of Halide SEs. The computation study by Wang et al. confirmed that halide SE materials have wide electrochemical windows and good interface compatibility with CAMs (Figure 10).[48] For example, Li₃YCl₆ and Li₃YBr₆ have large band gaps of 6.02 and 5.05 eV as well as wide electrochemical windows with cathodic limits of 0.59 and 0.62 V and anodic limits of 3.15 and 4.21 V, respectively. At lower potentials, the cathodic limits were caused by the reduction reaction of metal cations, such as Y in Li₃YCl₆ and Li₃YBr₆, leading to the formation of LiX (X = Cl or Br) and reduced metals. Due to the reduction of metal cations in halides, they are not thermodynamically stable in the presence of Li
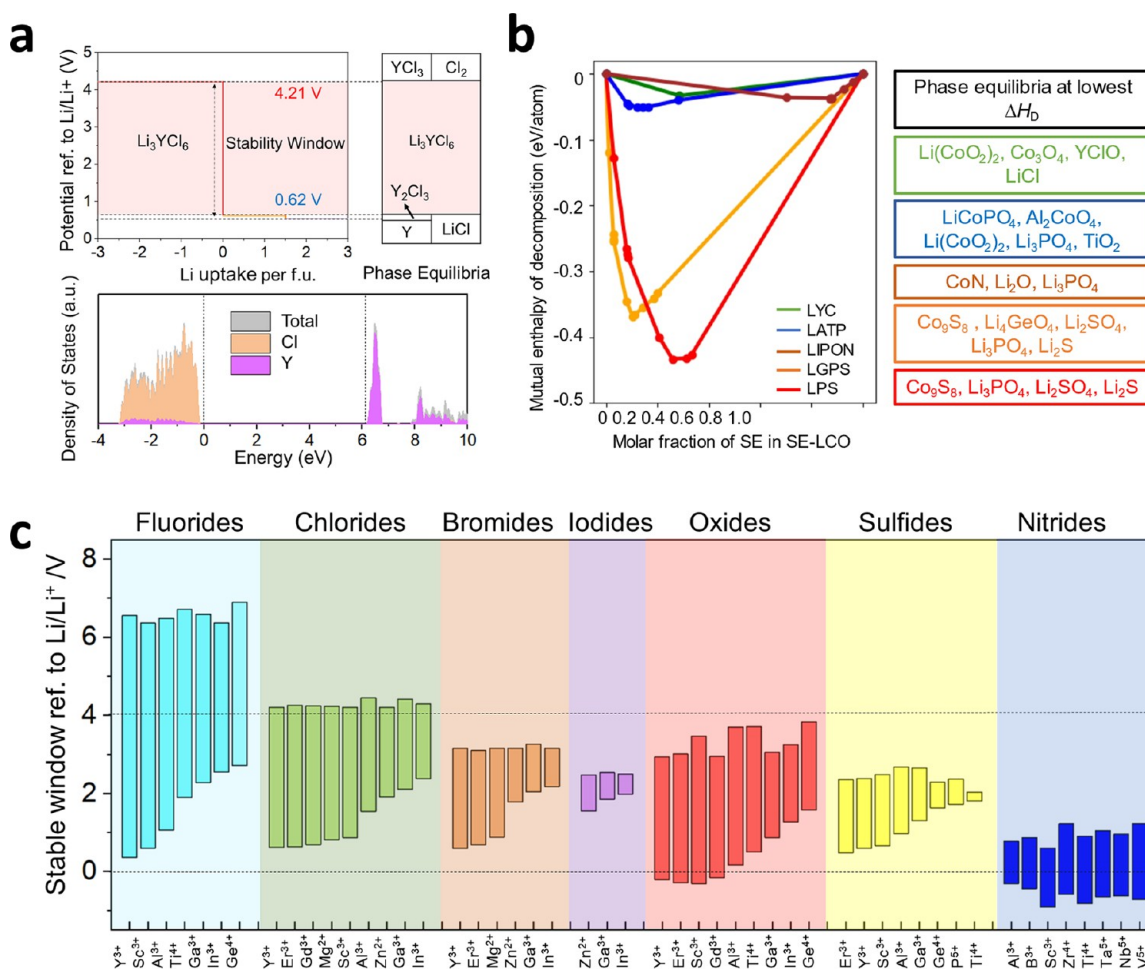
Figure 10. Thermodynamics intrinsic electrochemical window and interface stability of halide SEs. (a) Calculated thermodynamic equilibrium voltage profile and phase equilibria for Li_3YCl_6, and density of states (DOS) from HSE calculations. (b) Calculated mutual reaction enthalpy between SEs and $LiCoO_2$ as a function of mixing ratio and the corresponding phase equilibria. (c) Calculated thermodynamic intrinsic electrochemical windows of Li-M-X ternary fluorides, chlorides, bromides, iodides, oxides, sulfides, and nitrides. M is a metal cation at its highest common valence state. Reproduced with permission from ref 48. Copyright 2019, Wiley-VCH.

metal. At high potentials, the anodic limits of ∼3 V for bromides and ∼4 V for chlorides are caused by the oxidation reaction of halogen anions. The oxidation limits of chloride SEs are generally higher than those of oxide and sulfide SEs, such as LGPS (1.72−2.29 V), Li_3PS_4 (1.71−2.31 V), $Li_{1.3}Al_{0.3}Ti_{1.7}(PO_4)_3$ (2.17−4.21 V), and $Li_{0.33}La_{0.56}TiO_3$ (1.75−3.71 V). The high oxidation stability is an intrinsic property of the halide anion chemistries, as confirmed by the analyses of thermodynamic intrinsic windows of Li-M-X ternary compounds (M = cation; X = F, Cl, Br, I, O, S, N) over a range of cations and anions (Figure 10c). Among these common anion chemistries, fluorides have the highest oxidation stability of more than 6 V, followed by the chlorides at around 4 V. For oxides, the oxidation limits are much higher than the thermodynamic intrinsic limits of 3.0−3.5 V due to the kinetic limitations of O^{2-} oxidation. In general, sulfides have intrinsically poor stability, considering that the oxidation of S^{2-} occurs at >2 V. On the other hand, the cathodic limits are largely determined by the reduction of cations. In general, rare-earth elements, including Sc^{3+}, Y^{3+}, and many lanthanides, have relatively good reduction stability, while Ge^{4+}, Sn^{4+}, P^{5+}, and Sb^{5+} sacrifice their electrochemical stability under reduction.[37] For common chloride SEs Li_3MCl_6, the reduction limits follow the trend of $Y^{3+} < Sc^{3+} < In^{3+}$. No known halide SEs are stable

with Li metal, and they are often used with an In anode.[48,54,113,126,127] Therefore, it is a critical challenge to enable halide SEs with good stabilities with Li metal. Among these anion chemistries, nitrides are a known exception that exhibit intrinsic thermodynamic stability toward Li metal.[48] Thermodynamic analyses of the intrinsic electrochemical stabilities of different anion chemistries show the significant advantages of chloride SEs in the electrochemical stability window compared to sulfide SEs.

The thermodynamic analyses also reveal that halide SEs have significantly better interface stabilities with CAMs than sulfide SEs (Figure 10b). For sulfide SEs, the reaction energies of LGPS with $LiCoO_2$ and $Li_{0.5}CoO_2$ are −322 and −476 meV/atom, respectively. In comparison, the Li_3YCl_6 chloride is much more stable with $LiCoO_2$ cathode with a minor reaction energy of −33 meV/atom, and is stable in the presence of delithiated $Li_{0.5}CoO_2$. The analyses also confirm good stabilities of halide SEs with other CAMs, including $LiFePO_4$, $LiCoPO_4$, $LiNiO_2$, $LiNi_{0.5}Mn_{1.5}O_4$, and NMC-111.[48,128,129] In summary, thermodynamic analyses confirm that chloride SEs show good electrochemical and interfacial stabilities with the most common CAMs, which is much better than the current sulfide SEs.

Cathodes Using Halide SEs. 4-V-class Ni-rich layered $LiMO_2$ compounds (M = Ni, Co, Mn, and Al mixture) are the
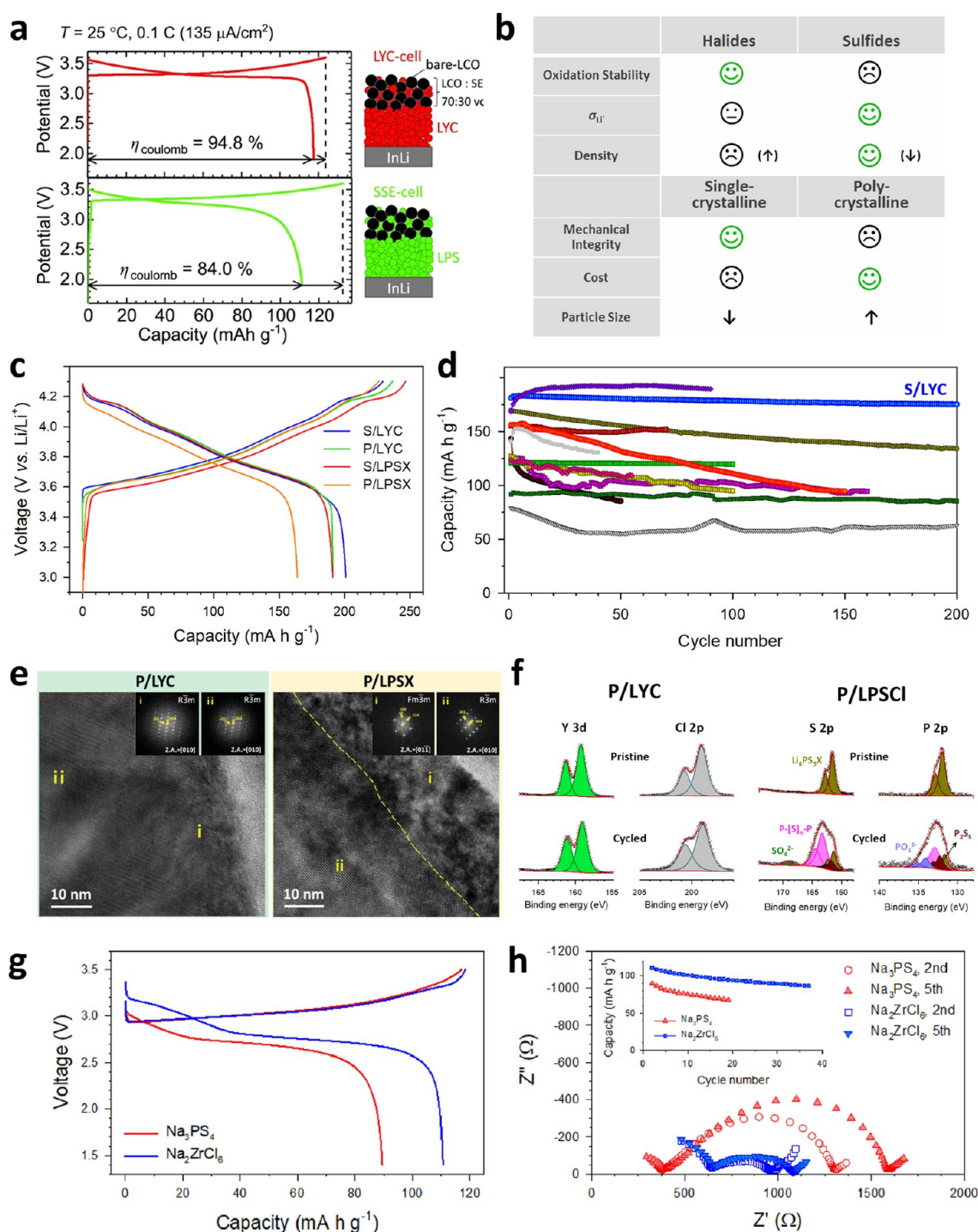
Figure 11. Electrochemical performances of LiMO$_2$ (or NaMO$_2$) using halide SEs. (a) Initial charge–discharge curves of LiCoO$_2$ cathodes using halide or sulfide SEs at 0.1C and 25 °C. Reproduced with permission from ref 27. Copyright 2018, Wiley-VCH. (b) Pros and cons for halide and sulfide SEs, and for single-crystalline and polycrystalline NCA. (c) First-cycle charge–discharge voltage profiles at 0.1C and 30 °C for electrodes with four different combinations of NCA (single- or polycrystalline) and SEs (Li$_3$YCl$_6$ or LPSX). (d) Cycling performances for LiCoO$_2$ and Ni-rich layered oxides in all-solid-state cells. Ex situ TEM and XPS results of P/LYC and P/LPSX electrodes in all-solid-state cells cycled at RT. (e) Low- and high-magnification ex situ TEM images for surface regions of the secondary particles of poly-NCA in contact with Li$_3$YCl$_6$ and LPSX after 100 cycles with corresponding FFT images. (f) Ex situ XPS spectra for P/Li$_3$YCl$_6$ and P/LPSX electrodes before cycling and after 100 cycles. Reproduced with permission from ref 22. Copyright 2021, Wiley-VCH. (g) First-cycle charge–discharge voltage profiles at 0.1C and 30 °C for NaCrO$_2$/Na–Sn all-solid-state cells using BM-Na$_2$ZrCl$_6$ or Na$_3$PS$_4$ as catholytes, and (h) the corresponding Nyquist plots. Cycling performance at 0.1C is also shown in the inset. Reproduced with permission from ref 70. Copyright 2021, Elsevier.

key CAMs enabling high energy density in the state-of-the-art LIBs,[11,130−133] and the adoption of these CAMs in ASSBs is critical to achieve high energy density for commercial applications. Thus far, multiple studies investigated the sulfide SEs for integration with the Ni-rich layered LiMO$_2$ in ASSBs.[5,6,9,44,45,134−136] However, the sulfide SEs suffer from

Table 4. Comparison of Electrochemical Performances of Cathodes Using Halide SEs

ref	CAM	SE	first discharge capacity specific capacity [mA h g⁻¹]	areal capacity [mA h cm⁻²]	ICE [%]	cycling retention [%]	current density [mA cm⁻²]	T [°C]	voltage range [V vs Li/Li⁺]	electrode mass loading [mg cm⁻²]	fraction of CAM [%]	note	fabricating pressure [MPa]	operating pressure [MPa]
27	LiCoO₂	Li₃YCl₆	115	1.14	94.8	98.0 (100 cycles)	0.135	25	2.52–4.22	9.9 (CAM)	82	–	300	–
53	LiCoO₂	Li₃InCl₆	127	–	92	75 (100 cycles)	0.13	25	2.5–4.2	–	70	PTFE	250	–
111	NMC811	Li₃InCl₆	136.4 / 131.2 / 138.2 / 154	12.16 / 5.85 / 2.64 / 1.37	72.2 / 74.9 / 78.8 / 84.2	– / – / – / 97.4 (70 cycles)	0.13	25	2.52–4.42	89.17 (CAM) / 44.59 (CAM) / 19.1 (CAM) / 8.92 (CAM)	70	PTFE	250	–
54	LiCoO₂	Li₃ScCl₆	126.2	1.25	90.3	83 (160 cycles)	0.13	25	2.52–4.22	8.92 (CAM)	70		375	–
59	LiCoO₂	Li₂.₆₃₃Er₀.₆₃₃Zr₀.₃₆₇Cl₆	110 (0.1C)	0.98	96.4	91 (100 cycles, 0.5C)	0.11 (0.1C), 0.55 (0.5C)	25	3.0–4.3	8.91 (CAM)	70		374	–
115	LiCoO₂	Li₃InCl₆	123.2 / 131.7	6 / 1.71	– / 92.7	– / 69 (200 cycles)	0.13	25	3.1–4.2	48.7 (CAM) / 12.99 (CAM)	85	LIC coating on LCO, PTFE	437	-
22	poly-NCA88	Li₃YCl₆	182.4 (0.1C)	1.17	–	77.4 (200 cycles, 0.5C)	0.13 (0.1C), 0.64 (0.5C)	30	3.0–4.3	6.43 (CAM)	40.7		370	70
			191 (0.1C)	1.47	80.8	67.8 (200 cycles, 0.5C)	0.15 (0.1C), 0.77 (0.5C)			7.68 (CAM)	68			
			193.2 (0.5C)	1.24	–	75.1 (100 cycles, 0.5C)	0.13 (0.1C), 0.64 (0.5C)		3.0–4.5	6.43 (CAM)	40.7			
			199 (0.1C)	1.28	89.6	96.8			3.0–4.3	6.43 (CAM)	40.7			
			201 (0.1C)	1.54	87.7	67.2 (200 cycles, 0.5C)	0.15 (0.1C), 0.77 (0.5C)			7.68 (CAM)	68			
159	NCM111	3LiCl–GaF₃	107.5	2.15	74.2	45 (100 cycles)	0.6	60	2.85–4.05	~20 (CAM)	85	Li/LLZTO/ (3Li Cl–GaF₃)/ cathode	250	–
52	NCM622	Li₂.₇Yb₀.₇Zr₀.₃Cl₆– HT350	~170 (0.2C)	1.39	–	~80 (150 cycles, 0.2C)	0.2 (0.2C)	RT	2.8–4.3	~8.15 (CAM)	80		375	–
	LiCoO₂		125 (0.1C)	1.02	–	~90 (200 cycles, 0.5C)	0.11 (0.1C), 0.55 (0.5C)		3.0–4.3					

Table 4. continued

ref	CAM	SE	specific capacity [mA h g⁻¹]	areal capacity [mA h cm⁻²]	ICE [%]	cycling retention [%]	current density [mA cm⁻²]	T [°C]	voltage range [V vs Li/Li⁺]	electrode mass loading [mg cm⁻²]	fraction of CAM [%]	note	fabricating pressure [MPa]	operating pressure [MPa]
49	single-NCA88	Li_2ZrCl_6	206 (0.1C)	2.33	85.8	91.3 (100 cycles, 0.5C)	0.13 (0.1C), 0.64 (0.5C)	30	3.0–4.3	11.3 (CAM)	57		370	70
	$LiCoO_2$		156 (0.1C)	1.59	91.4	90.5 (100 cycles, 0.5C)	0.16 (0.1C), 0.8 (0.5C)			10.19 (CAM)	68			
51	single-NCA88	$Li_{2.60}Yb_{0.40}Hf_{0.40}Cl_6$	188	1.03	84.8	83.6 (1000 cycles)	0.64 (0.5C)	30	3.0–4.3	5.49 (CAM)	49		370	70
72	$LiCoO_2$	$Li_3YBr_3Cl_3$	124 (0.1C)	0.7	–	–	–	RT	2.62–4.27	5.68 (CAM)	60		235.2 (44.1)	44.1
145	single-NCM811	Li_2ZrCl_6	181 (0.1C)	1.613	90.3	–	0.178	25	2.82–4.42	8.917 (CAM)	75		187	187
	$LiCoO_2$		137 (0.1C)	1.248	97.9	–	0.125		2.52–4.22					
127	$LiCoO_2$	$Li_3InCl_{4.8}F_{1.2}$	203.7	1.816	89.2	50.1 (70 cycles)	0.125	25	2.6–4.8	8.917 (CAM)	68	high voltage	300	–
			160.6	1.432	92	63.5 (70 cycles)	0.125		2.6–4.47					
138	$LiCoO_2$	$Li_{2.556}Yb_{0.492}Zr_{0.492}Cl_6$	193.9	1.729	89.2	82.1 (0.3C, 50 cycles)	0.535	25	2.5–4.5	8.917 (CAM)	68	high voltage	360	100
	$LiNi_{0.83}Co_{0.12}Mn_{0.05}O_2$	$Li_{2.766}Y_{0.462}Zr_{0.462}Cl_6$	200.6 (0.1C)	1.789	89.3	53.1 (0.3C, 50 cycles)			2.5–4.3					
			209.8 (0.1C)	1.87	91.5	78.3 (0.3C, 50 cycles)								
50	$LiNi_{0.83}Co_{0.12}Mn_{0.05}O_2$	$Li_2In_{0.33}Sc_{0.33}Cl_4$	–	–	–	–	0.49	RT	2.8–4.3	21.59	80	high mass loading	375	250
	$LiCoO_2$		–	–	–	100 (500 cycles)	1.2	50	2.6–4.3	52.46	80			
	$LiCoO_2$		–	–	–	–	1.79	50	3.0–4.3	26.08 (CAM)	80			
	$LiCoO_2$		–	–	–	–	1.24	RT	2.8–4.3	27.09 (CAM)	80			
	$LiNi_{0.85}Co_{0.12}Mn_{0.05}O_2$		–	–	–	95 (110 cycles)	0.226	RT	2.8–4.8	6.26 (CAM)	80	high voltage		
	$LiNi_{0.85}Co_{0.12}Mn_{0.05}O_2$		–	–	–	80 (3000 cycles)	3.36	RT	2.8–4.3	6.21 (CAM)	80			
	$LiNi_{0.6}Co_{0.2}Mn_{0.2}O_2$		–	–	–	92.8 (320 cycles)	0.235	RT	2.8–4.6	6.52 (CAM)	80	high voltage		
	$LiNi_{0.85}Co_{0.12}Mn_{0.05}O_2$		–	–	–	89.1 (695 cycles)	0.249	RT	2.8–4.3	6.93 (CAM)	80		360	100

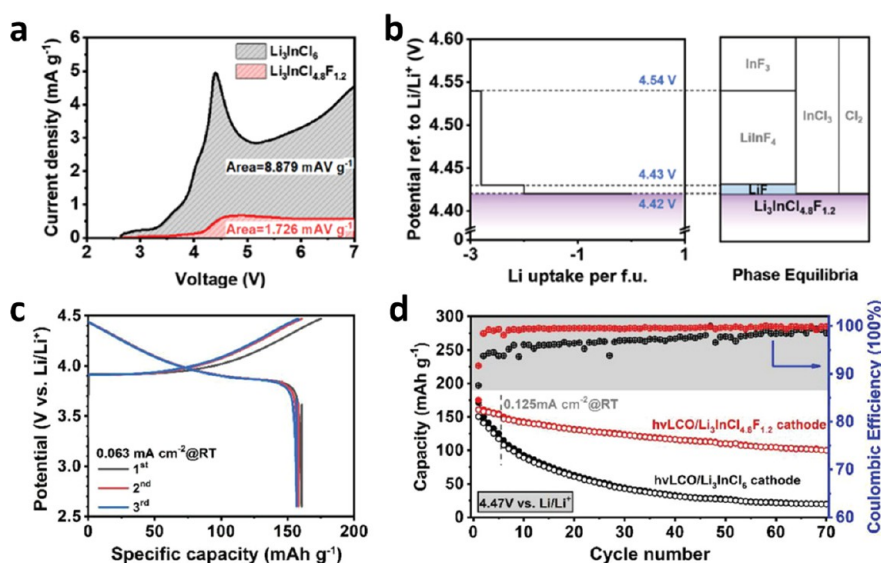**Figure 12.** Electrochemical oxidation stability and performance of F-substituted Li_3InCl_6, $Li_3InCl_{4.8}F_{1.2}$, compared with Li_3InCl_6. (a) LSV analysis of Li_3InCl_6 and $Li_3InCl_{4.8}F_{1.2}$ from OCV to 7 V. (b) Phase equilibria of $Li_3InCl_{4.8}F_{1.2}$ at different potentials, based on the first-principles computation. (c) First three discharge−charge voltage curves of $LiCoO_2$ cathodes using $Li_3InCl_{4.8}F_{1.2}$. (d) Cycling performances of $LiCoO_2$ cathodes using $Li_3InCl_{4.8}F_{1.2}$ or Li_3InCl_6 in the voltage range of 2.6−4.47 V (vs Li/Li^+). Reproduced with permission from ref 127. Copyright 2021, Wiley-VCH.

poor electrochemical oxidation stability. Extensive efforts have been devoted to the protective coatings for CAMs (e.g., $LiNbO_3$, Li_2ZrO_3, and $Li_{3-x}B_{1-x}C_xO_3$)[42,43,45,56] and compositional tuning of sulfide SEs (e.g., $Li_{10}GeP_2S_{12-x}O_x$, $Li_6PS_{4.7}O_{0.3}Br$) to enable cathode stability.[136,137] In the pioneering work by Asano et al., unprotected $LiCoO_2$ using the halide SE Li_3YCl_6 demonstrated a high ICE of 94.8%, in sharp contrast to that of 84.0% using sulfide SE Li_3PS_4 (Figure 11a).[27] Electrochemical impedance spectroscopy (EIS) measurements revealed much lower interfacial resistance when using Li_3YCl_6 (16.8 Ω cm²), compared to that while using Li_3PS_4 (128.4 Ω cm²). Indeed, theoretical and experimental results demonstrated that halide SEs possess an electrochemical oxidation stability up to ∼4.2 V (vs Li/Li^+). Thus, halide SEs are considered a potential game changer in ASSB technology based on high-energy $LiMO_2$ CAMs.[22,27,49−51,59] The electrochemical performances of various cathodes used together with different halide SEs are compared in Table 4.

Han et al. investigated and compared the electrochemical performance of a variety of uncoated Ni-rich layered oxide CAMs, such as single-crystalline $LiNi_{0.88}Co_{0.11}Al_{0.01}O_2$ (single-NCA) and conventional polycrystalline $LiNi_{0.88}Co_{0.11}Al_{0.01}O_2$ (poly-NCA), with halide SE, Li_3YCl_6 (LYC) compared to the conventional sulfide SE $Li_6PS_5Cl_{0.5}Br_{0.5}$ (LPSX) (Figure 11b−f).[22] Figure 11b shows the pros and cons of critical design factors for halide versus sulfide SEs combined with single-crystalline versus polycrystalline NCA, respectively. Secondary poly-NCA particles comprising randomly oriented grains undergo severe disintegration in all-solid-state cells even during the initial cycles, leading to poor ICE and fast capacity fading upon repeated cycling.[134] In contrast, the single-NCA particles do not suffer from mechanical failure. While the Li^+ conductivity of Li_3YCl_6 was an order of magnitude lower at 30 °C (0.40 mS cm⁻¹) than that of LPSX (4.8 mS cm⁻¹), it showed much superior electrochemical oxidation stability toward LPSX. The sloping voltage profile, starting at ∼3.2 V (vs Li/Li^+), during the initial charge when using LPSX confirmed the poor electrochemical

oxidation stability of sulfide SEs (Figure 11c). The combination of cracking-free single-NCA and the oxidation-tolerable Li_3YCl_6 has the highest performance at 30 °C in all aspects of discharge capacity (199 mA h g⁻¹ at 0.1C), ICE (89.6%), cycling stability (96.8% of capacity retention at the 200th cycle), and rate capability (130 mA h g⁻¹ at 4C). Ex situ TEM and XPS results confirmed that the Li_3YCl_6/NCA interfaces remained intact (Figure 11e,f), in contrast to the severe side reactions caused by the reactive Ni^{4+} with the sulfide SE. Moreover, as revealed by the operando electrochemical pressiometry measurements of control samples, the side reactions of sulfide SEs also contributed to the detrimental electrochemomechanical effects that accelerated the cracking of poly-NCA particles, whereas such side reactions and detrimental effects were circumvented using halide SEs.

Park et al. demonstrated the long-term cycling stability of bare single-crystalline NCA cathodes using $Li_{2.6}Yb_{0.4}Zr_{0.6}Cl_6$ with capacity retention of 83.6% after 1000 cycles at 30 °C.[51] Zhou et al. reported that uncoated $LiCoO_2$ and $LiNi_{0.85}Co_{0.1}Mn_{0.05}O_2$ with $Li_2In_{1/3}Sc_{1/3}Cl_4$ exhibited excellent rate capabilities and high-voltage cycling stability of up to 4.8 V vs Li/Li^+.[50] In particular, a long cycle life of >3000 cycles with 80% retention was demonstrated using a ASSB cell operated under 250 MPa. Zhou et al. further found that $Li_2In_{1/3}Sc_{1/3}Cl_4$ showed minimal reaction with $LiNi_{0.85}Co_{0.1}Mn_{0.05}O_2$ even when cycled up to 4.8 V (vs Li/L^+), which was ascribed to a kinetic overpotential owing to the exceptionally low electronic conductivity of $Li_2In_{1/3}Sc_{1/3}Cl_4$ (4.7 × 10⁻¹⁰ S cm⁻¹). Computational and experimental studies revealed the role of the central metals in determining electrochemical windows of halide SEs.[48,138] Li_3YbCl_6 with fully occupied atomic orbital of Yb ($4f^{14}6s^2$) has a higher electrochemical oxidation stability above 4.5 V (vs Li/Li^+), compared to those with Y ($4d^15s^2$) and In ($5s^25p^1$), as confirmed by cyclic voltammetry results.[138] Using Li_3YbCl_6, $LiNi_{0.83}Co_{0.12}Mn_{0.05}O_2$ and $LiCoO_2$ achieved good electrochemical performances with the higher cutoff voltages of 4.3 and 4.5 V (vs Li/Li^+), respectively, and capacity retentions of 78 and
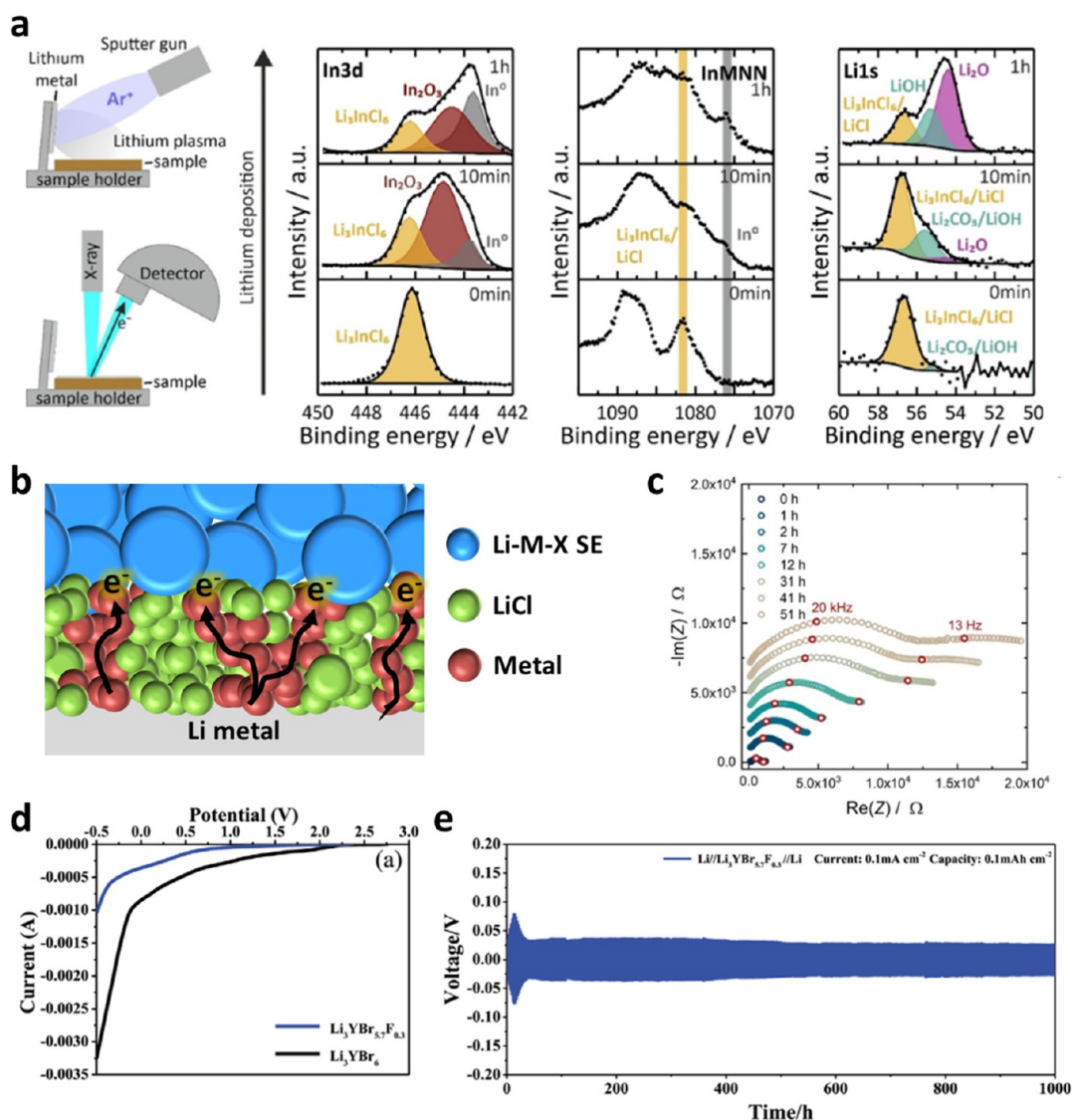
Figure 13. Electrochemical reduction stability of halide SEs. (a) Schematic of Li metal deposition on halide SE (Li_3InCl_6) using an argon sputter gun and subsequent XPS measurement (left). Auger In-MNN and XPS In 3d and Li 1s spectra during and after Li deposition on Li_3InCl_6 (right). Reproduced with permission from ref 143. Copyright 2021, Wiley-VCH. (b) Schematic illustrating the failure mechanism of the Li/halide SE interface. (c) Temporal evolution of the impedance spectra of a $Li/Li_3InCl_6/Li$ symmetric cell. Reproduced with permission from ref 143. Copyright 2021, Wiley-VCH. (d) LSV curves of Li_3YBr_6 and $Li_3YBr_{5.7}F_{0.3}$. (e) Li plating/stripping voltage profiles of $Li/Li_3YBr_{5.7}F_{0.3}/Li$ symmetric cells at 0.1 mA cm^{-2} with the capacity of 0.1 mA h cm^{-2}. Reproduced with permission from ref 126. Copyright 2021, Wiley-VCH.

82.2%, respectively, after 50 cycles. From ex situ XPS measurements of the $LiNi_{0.83}Co_{0.12}Mn_{0.05}O_2$ electrode with $Li_{2.556}Yb_{0.492}Zr_{0.492}Cl_6$, the Yb 4d spectrum was identical to that of the pristine sample, indicating good stability, whereas the Y 3d spectrum of $Li_{2.766}Y_{0.462}Zr_{0.462}Cl_6$ with the same CAM exhibited the peaks attributed to oxygen-containing compounds $Y_2O_3/Y_2(CO_3)_3$.

Recently, F-substituted chloride SEs are developed to further increase the electrochemical oxidation limit of halide SEs. Zhang et al. investigated the structural evolution and electrochemical stability of F-substituted Li_3InCl_6 ($Li_3InCl_{4.8}F_{1.2}$) (Figure 12).[127] As a result of F-substitution, F$^-$ anions occupy specific lattice sites of $Li_3InCl_{4.8}F_{1.2}$ and the lattice volume contracts due to the smaller ionic radius of F (F$^-$: 133 pm vs Cl$^-$: 181 pm). Electrochemical stability was improved by F-substitution at the expense of ionic conductivity decreased from 1.3 to 0.51 mS cm^{-1}. As revealed by the linear sweep voltammetry (LSV)

results (Figure 12a), $Li_3InCl_{4.8}F_{1.2}$ exhibited significantly improved electrochemical stability up to 4.3 V (vs Li/Li$^+$) or higher, compared to unsubstituted Li_3InCl_6. A first-principles computation study revealed the anodic limit of $Li_3InCl_{4.8}F_{1.2}$ to be 4.42 V and indicated the formation of F-based interphase materials, such as LiF, $LiInF_4$, and InF_3 (Figure 12b). These F-containing compounds passivated the interfaces, protecting further decomposition of $Li_3InCl_{4.8}F_{1.2}$, and thus increased the electrochemical oxidation stability. Furthermore, excellent electrochemical performance was demonstrated for ASSBs that employ F-substituted Li_3InCl_6 SE and $LiCoO_2$ cathode with a high cutoff voltage of 4.47 V (vs Li/Li$^+$), showing a high first discharge capacity of 160.6 mA h g^{-1} with a high ICE of 92% (Figure 12c). The cycling stability was significantly better for the ASSB cells employing $Li_3InCl_{4.8}F_{1.2}$ than those using Li_3InCl_6 (Figure 12d).
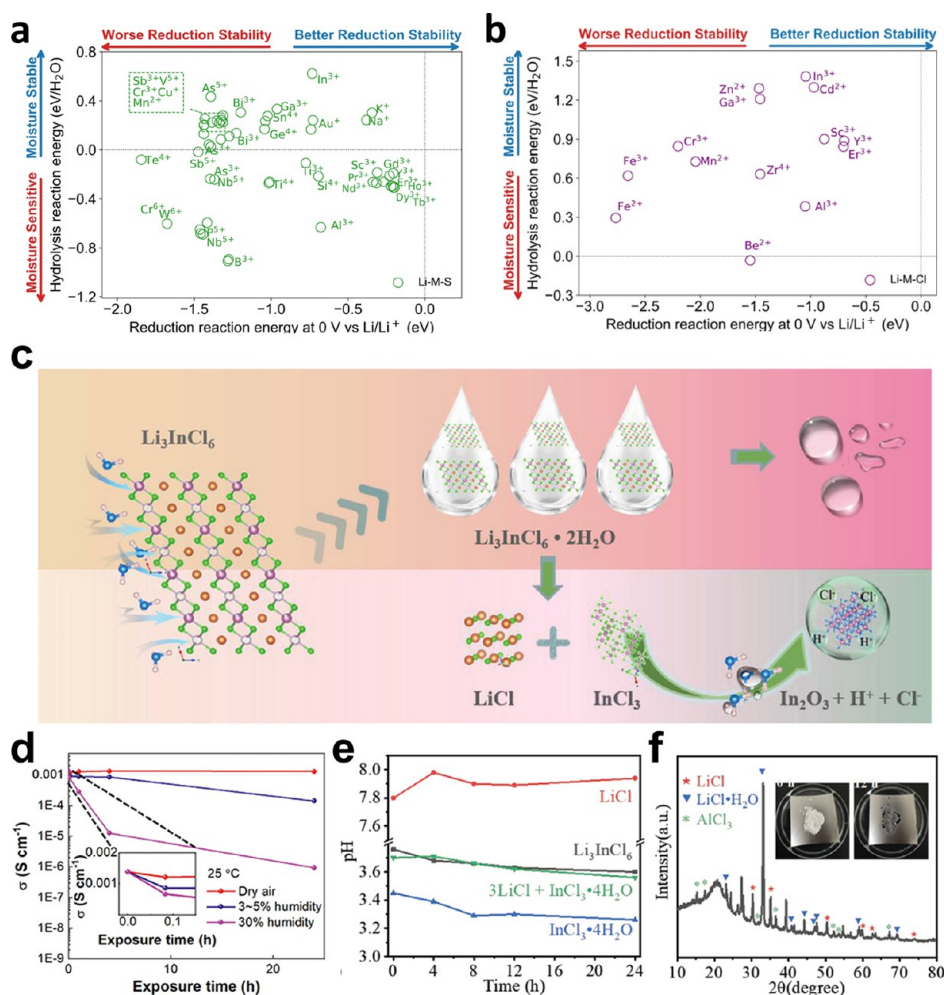
Figure 14. Chemical stability of SEs. Moisture stability (hydrolysis reaction energy, *y*-axis) versus reduction stability (reduction reaction energy with alkali metal, *x*-axis) for (a) 52 lithium ternary sulfides and (b) 14 lithium ternary chlorides. Reproduced with permission from ref 37. Copyright 2020, Wiley-VCH. (c) Illustration of Li_3InCl_6 reaction mechanism in humid air. Reproduced with permission from ref 144. Copyright 2021, Wiley-VCH. (d) Li^+ conductivity of Li_3InCl_6 at 25 °C as a function of air-exposure time with different humidity levels. Reproduced with permission from ref 114. Copyright 2021, the American Chemical Society. (e) pH of four aqueous solutions of Li_3InCl_6, LiCl, $InCl_3\cdot4H_2O$, and the mixture of LiCl and $InCl_3\cdot4H_2O$ as a function of time. (f) XRD pattern of Li_3InCl_6 reacted with Al foil for 12 h. Reproduced with permission from ref 144. Copyright 2021, Wiley-VCH.

Similar to Li^+ halide SEs, Na^+ halide SEs used as catholytes also significantly improved the performance of all-solid-state cells, compared to those using sulfide Na^+ SEs. Even though Na_2ZrCl_6 has an order of magnitude lower ionic conductivity (0.018 mS cm^{-1}) than that of Na_3PS_4 (0.1 mS cm^{-1}), $NaCrO_2$/Na-Sn all-solid-state cells using Na_2ZrCl_6 catholyte showed higher capacity (111 vs 90 mA h g^{-1}) and ICE (93.1% vs 76.5%) at 30 °C, compared to those using Na_3PS_4 (Figure 11g,h). Control experiments using EIS and ex situ XPS revealed that Na_2ZrCl_6 remained intact upon cycling, in contrast to the severe oxidation for Na_3PS_4.[139] Further, Wu et al. reported the long-term cycling stability of $NaCrO_2$/Na-Sn all-solid-state cells using $Na_{2.25}Y_{0.25}Zr_{0.75}Cl_6$ as the catholyte at 40 °C, in which a capacity retention of 89.3% after 1000 cycles was reported.[123]

Anodes for Halide SEs. As discussed in the section "Intrinsic Electrochemical Stability of Halide SEs", halide SEs exhibit poor electrochemical reduction stability, impending their application to anodes. Ji et al. compared the reactivity of sulfide (Li_6PS_5Cl) and halide (Li_3YCl_6) SEs with that of Li powders.[127] While the original XRD peaks were preserved in the Li_6PS_5Cl-Li mixture, for the Li_3YCl_6-Li mixture the characteristic peaks for

Li_3YCl_6 were almost degraded and the LiCl peak appeared, indicating the severe reaction between Li_3YCl_6 and Li metal. Besides the thermodynamic intrinsic stabilities of the materials, the formation of interfacial products as a result of the electrochemical reduction of halide SEs was also responsible for the interfacial stability.[31] The sulfide Li_6PS_5Cl SE decompose to Li_2S, Li_3P, and P_2S_5 in contact with Li metal or under low potentials,[31,140] and these products block the electron pathway while maintaining the Li^+ pathways, thus preventing further decomposition, similar to the working mechanism of solid electrolyte interphases (SEIs) in LIBs.[1,31,141,142] This passivating mechanism of sulfide SEs enables their compatibility with Li metal anodes. In contrast, halide SEs do not form favorable decomposition products when in contact with Li metal. Specifically, central metal ions in halide SEs are reduced to form detrimental metals, which are electronic conducting.[48] Using XPS, Riegger et al. measured the decomposition products of Li_3YCl_6 and Li_3InCl_6 during the sputtering deposition of Li on the SEs (Figure 13a).[143] As halide SEs were decomposed by the deposited Li metal, metal oxides were first formed, followed by the reduction to the metal. This result indicates that the

electrochemical reduction reaction of halide SEs in contact with Li metal continues and does not cease because of the electron conduction provided by the metal (Y or In) (Figure 13b), and as a result the SE/Li interfacial resistance continuously increases over time (Figure 13c).

To improve the stability of halide SEs with Li metal, Yu et al. suggested the F-substitution strategy, which was demonstrated for sulfide SEs.[126] The LSV results for $Li_3YBr_{5.7}F_{0.3}$ compared to Li_3YBr_6 showed that the onset voltage for the reduction was shifted in the negative direction and the overall reduction currents were decreased (Figure 13d). In addition, the XPS depth profiling results revealed the formation of LiF at the Li metal interfaces, which helped the passivation of the interfaces.[126] For Li/SE/Li symmetric cells using Li_3YBr_6, a high overpotential of ∼0.25 V occurred initially and continued to increase after 300 h. In contrast, a much lower overpotential was maintained for more than 1000 h for the F-substituted sample (Figure 13e). While the F-substitution strategy improved the anode interfacial stability of halide SEs, the overall results were unsatisfactory compared to those using sulfide SEs. For example, a very large overpotential of 0.4−1.5 V was observed even at low current densities (e.g., 0.1 mA cm$^{−2}$).[54,113,126,127] For this reason, ASSBs that employ sulfide SEs as the anolyte (or SE membranes) and halide SEs as the catholyte could benefit from the advantages of both SE chemistries for practical applications.[9] Indeed, several literature reports on halide SEs have adopted the dual electrolyte configuration for ASSB systems.[22,49,51,72,126,127]

■ INDUSTRIAL PERSPECTIVE OF HALIDE SEs

Air/Moisture Stability. Better chemical oxidation stability is a key positive feature of halide SEs compared to sulfide SEs. Asano et al. showed that the exothermic heat generated by the oxidation reactions of Li_3YCl_6 was 20−100 times lower than that for glass-ceramic $Li_2S-P_2S_5$.[27] Moreover, halide SEs do not suffer from the evolution of toxic H_2S gases as sulfide SEs upon exposure to humid air. Even with much better stabilities than sulfide SEs, halide SEs are also unstable in atmospheric air. Most halide SEs are hydrophilic, and water molecules from the moist air adsorb on the halide surfaces. As a result, irreversible chemical degradation occurs as the hydrolysis to form $MCl_3 \cdot xH_2O$ and $LiCl \cdot xH_2O$ in most halide SEs.[58,114] During the dehydration process with heating, $MCl_3 \cdot xH_2O$ is converted into M_2O_3 and HCl.

Zhu et al. conducted a systematic thermodynamic analysis for a wide range of halide and sulfide materials.[37] They investigated the thermodynamics of the hydrolysis and reduction reactions of M-X and Li/Na-M-X (M = cation, X = S, Cl) based on DFT computation data. The stability trends among the different chemistries were revealed, and the effects of cations, anions, and Li/Na content on moisture stability were identified (Figure 14a,b). For sulfides, metalloid ions, including Ga^{3+}, Ge^{4+}, Sn^{4+}, Sb^{5+}, Pb^{4+}, and Bi^{3+}, showed significantly better moisture stability than P^{5+}, in consistent with the empirical hard and soft acid and base (HSAB) theory and previous experiments.[38−41] The alkali and alkaline ions and late-transition-metal ions exhibited relatively better moisture stabilities. The thermodynamics analyses confirm the chlorides showed significantly better moisture stability than sulfides according to their hydrolysis reaction energies, in agreement with the experimental results. Their analyses found that for chlorides In cation shows the best moisture stability, which is in good agreement with the experimental reports of the excellent moisture stability of

Li_3InCl_6.[53] In addition, Zhu et al. charted the moisture and electrochemical stabilities for sulfides and chlorides with different cations (Figure 14b) and these charts provided guidance for cation selection or substitution in designing moisture-stable sulfide/chloride SEs.

As discussed in the section "Synthesis Methods of Halide SEs", compared with other halide SEs, Li_3InCl_6 possesses exceptional chemical properties when in contact with water. While other halide SEs are decomposed to form $MCl_3 \cdot xH_2O$ and LiCl, Li_3InCl_6 is converted to the hydrated intermediates ($Li_3InCl_6 \cdot xH_2O$) that have much better resistance to the detrimental hydrolysis reaction during the dehydration process (Figure 14c).[114,144] Since the hydrated intermediates may have lower Li^+ conductivities than that of the original phase (Li_3InCl_6), there is severe degradation of Li^+ conductivity upon exposure to air with higher humidity (Figure 14d).[114] The original Li^+ conductivity cannot be recovered even after the dehydration process, because of the partial hydrolysis reaction. In addition, the aqueous solutions of $InCl_3$ or Li_3InCl_6 are acidic (Figure 14e), which can be explained by the reaction of In^{3+} with water to generate the indium hydroxide and hydronium ions ($In^{3+} + 3H_2O \rightleftharpoons In(OH)_3\downarrow + 3H^+$). As a result, halide SEs in ambient air corrode an Al foil, which is an essential cell component (Figure 14f).[144] Compositional tuning of halide SEs using In showed positive effects on their air/moisture stability. With an increased ratio of substituting Li_3YCl_6 with In^{3+}, the ccp anion arrangement formed preferentially over the hcp structure, and the hydrated intermediates were formed instead of a hydrolysis after exposure to humid air.[58] The original ccp crystal structure was recovered after the dehydration process. As recently proposed, Li_2ZrCl_6 showed better humidity tolerance with no signs of moisture uptake or severe conductivity degradation, compared to Li_3InCl_6, which needs a dehydration process after being exposed to moisture.[145] Nevertheless, the air stability of Li_2ZrCl_6 and its potential applicability in ASSBs still require meticulous investigations.

Cost. The high cost of nearly all types of inorganic SEs is a significant barrier to their commercialization. In particular, the expensive Li_2S precursor, with an estimated bulk price of 732 USD kg$^{−1}$ (Table S1),[146] and the high production cost associated with maintaining the inert environment make sulfide SEs highly expensive.[22,147,148] In contrast, the price of LiCl precursor for the halide SEs is only ∼18 USD kg$^{−1}$ (estimated bulk price). Since both Li sources and SEs for halides are stable in dry air and do not pose a risk for generating toxic H_2S gas, the production cost of halide SEs is expected to be lower than those for sulfide SEs.

However, current central metals in halide SEs exhibiting ionic conductivities of ∼10$^{−3}$ S cm$^{−1}$ are expensive and are not attractive for mass production.[27,51,53,54] These halide SEs contain a large composition of REMs (e.g., Sc, Y, Tb−Lu), which have low abundance in the Earth's crust, in contrast to the phosphorus in sulfides SE. For example, the abundance of yttrium is 33 ppm compared to the 1050 ppm for phosphorus.[139] Since REMs need to be extracted from rare-earth minerals which often contain more than one rare-earth element, it is difficult to separate a specific REM from other lanthanides due to their similar properties. Each REM can be separated from the other lanthanides by ion-exchange chromatography by dissolving rare earth minerals into various acids, such as sulfuric acid.[149] Unfortunately, such processes pose severe environmental and health risks during the mining and purification processes. The metal halides are generally prepared using the "ammonium
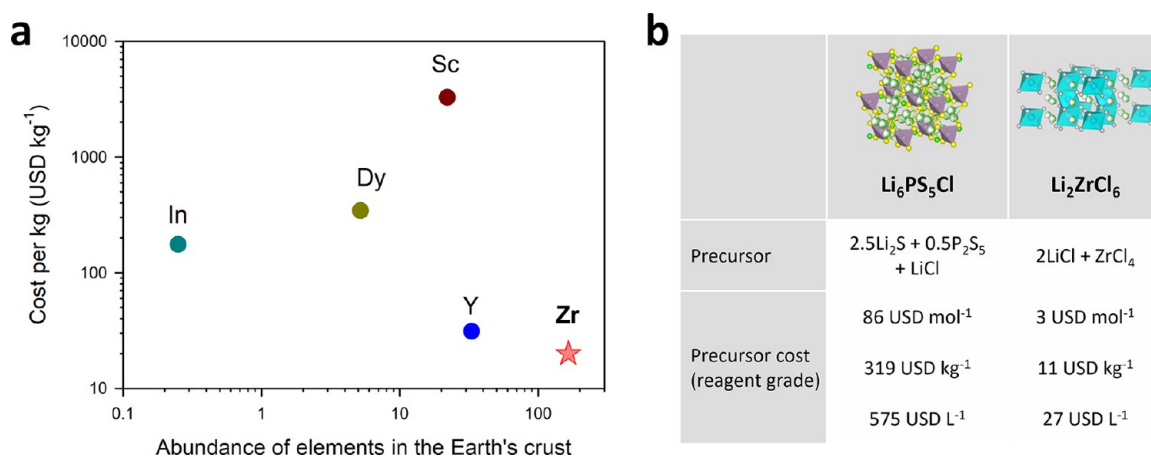
Figure 15. (a) Unit prices and abundance in the Earth's crust for various metals used for halide SEs. (b) Cost of precursors for Li_6PS_5Cl and Li_2ZrCl_6.
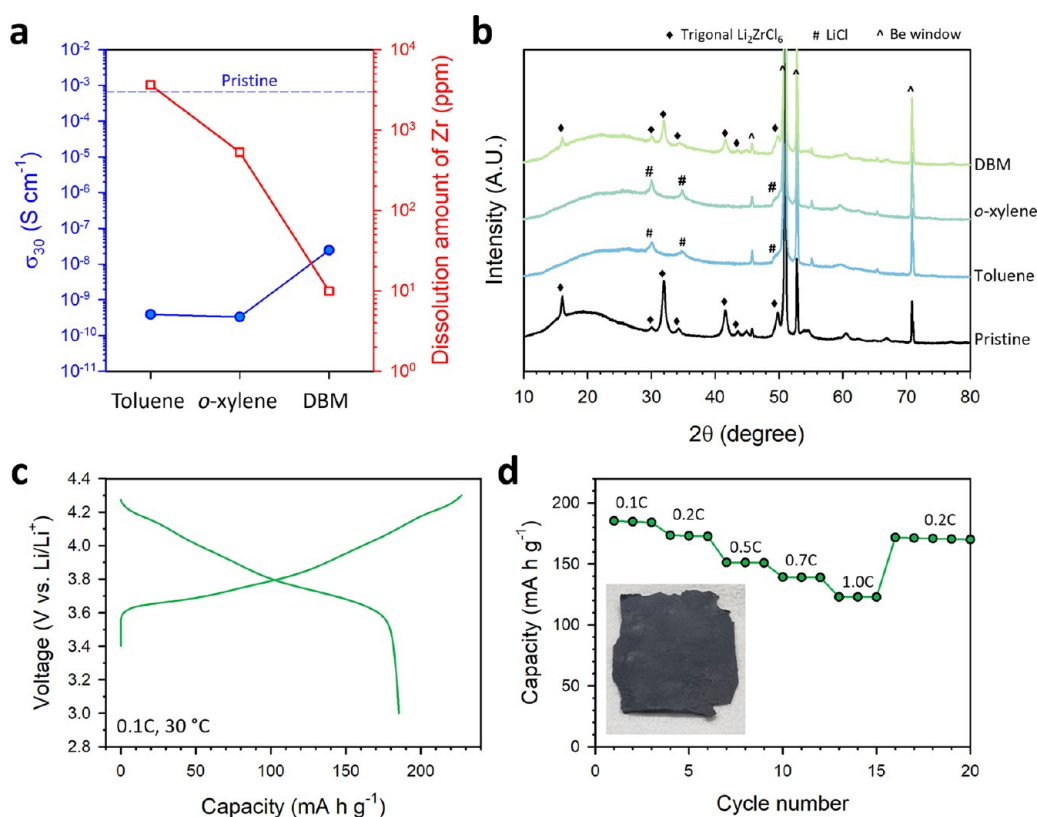

Figure 16. Compatibility results of slurry-processing solvents with Li_2ZrCl_6 and electrochemical performance of $LiNi_{0.8}Co_{0.1}Mn_{0.1}O_2/Li–In$ half-cells employing dry-fabricated $LiNi_{0.8}Co_{0.1}Mn_{0.1}O_2$ electrodes. (a) Li^+ conductivities at 30 °C and dissolved amounts of Zr for Li_2ZrCl_6 after the exposure to the solvents, and (b) corresponding XRD patterns. (c) First-cycle charge–discharge voltage profiles of the dry-fabricated $LiNi_{0.8}Co_{0.1}Mn_{0.1}O_2$ electrodes at 0.1C and 30 °C and (d) corresponding rate capability. A photograph of the dry-fabricated electrode is shown in the inset of (d).

chloride route" starting from either M_2O_3, hydrated chloride, oxychloride, or $MCl_3 \cdot 6H_2O$ (Table 3).[119] This series of complex processes further increases the cost of the REM halides.

In this context, Zr is an exceptionally advantageous central metal for halide SEs. Zr is 5 times more abundant than yttrium, and owing to such high abundance,[146] it has been widely utilized in a variety of industrial areas (Figure 15a).[150−152] The major commercial source of zirconium is zircon ($ZrSiO_4$), which is very common and widely distributed in the Earth's crust, and is directly used for commercial applications. In addition, the direct

chlorination of zircon proceeds in a fluidized bed containing carbon and produces zirconium tetrachloride according to the following reaction:[153]

$$ZrSiO_4 + 2C + 4Cl_2 \rightarrow ZrCl_4 + SiCl_4 + 2CO_2 \qquad (3)$$

The bulk price of $ZrCl_4$ is estimated to be 8.1 USD kg^{-1} (Table S1),[145] which could allow for the production of cost-effective halide SEs. Combining the low costs of LiCl and $ZrCl_4$, the price per volume for Li_2ZrCl_6 is predicted to be around 27 USD L^{-1}, which is 21 times cheaper than the estimated price of
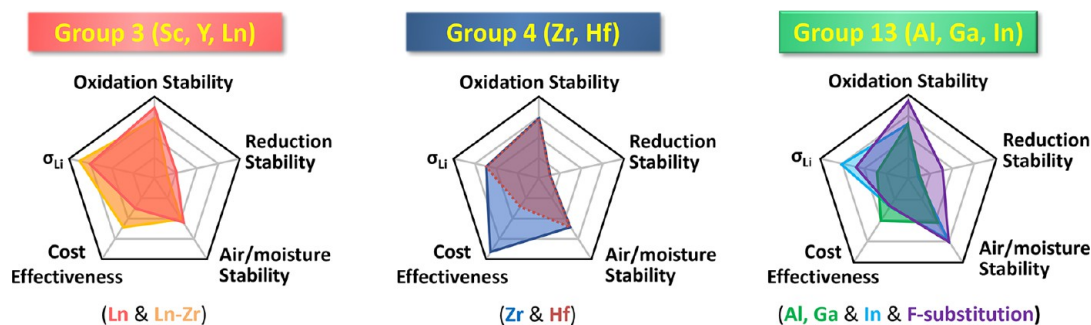
Figure 17. Spider plots comparing performances of the three types of halide SEs.

575 USD L^{-1} for Li$_6$PS$_5$Cl (Figure 15b), which is based on the estimated target price of Li$_2$S for industrial use. If one considers the production costs for protective coatings on CAMs and for maintaining the stringent dry-air conditions for sulfide SEs,[59,147] the cost advantages of Li$_2$ZrCl$_6$ over Li$_6$PS$_5$Cl may be further widened. Moreover, the divalent S^{2-} anion lattices of sulfide SEs (e.g., Li$_6$PS$_5$Cl) require a large amount of Li per volume (41.13 mol L^{-1} for Li$_6$PS$_5$Cl) for satisfying the charge neutrality, which translates to the need for a large amount of the expensive Li$_2$S. In contrast, the amount of Li in Li$_2$ZrCl$_6$ having a monovalent Cl$^-$ anion lattice structure is only 16.17 mol L^{-1}, which is five times lower than that required for Li$_6$PS$_5$Cl. These considerations emphasize the relevance of the recent developments in new Zr-based halide SEs that are free from REMs, such as Li$_2$ZrCl$_6$ and Fe^{3+}-substituted Li$_2$ZrCl$_6$, by a mechanochemical process.[49]

Fabrication of Sheet-Type Electrodes. While most reported results of halide SEs were obtained using lab-scale pelletized cells, pouch-type cells using sheet-type electrodes and thin SE membranes are needed for practical applications.[9,94,105,106,135,154−160] Wet-slurry fabrication is desirable for utilizing and exploiting the current manufacturing infrastructure of conventional LIBs without major alterations.[155−157,160] However, the chemical instability of halide SEs is also a critical issue as is the case for sulfide SEs.[155,156,160,161] For wet-slurry fabrication using sulfide SEs, processing solvents with low or intermediate polarity, such as xylene, toluene, dibromomethane (DBM), benzyl acetate, or hexyl butyrate, should be used, which in turn limit the choice of the polymeric binders toward the rubber-based ones, such as nitrile butadiene rubber and butadiene rubber.[155,156,160−162] Furthermore, Nam et al. showed that the detrimental effects of Li$^+$-insulating binders in electrodes could cause the degradation in electrochemical performance,[155] which fueled the research for binders with good Li$^+$ conductivity or enhanced mechanical properties.[155,160,161] These research directions could serve as a guidance for developing wet-slurry fabrication using halide SEs. In this regard, the stability of mechanochemically prepared Li$_2$ZrCl$_6$ toward various organic solvents was assessed by measuring ionic conductivities and dissolved amounts of Zr after exposure to various solvents (Figure 16). Li$_2$ZrCl$_6$ showed severe dissolution in the highly polar solvent *N*-methyl-2-pyrrolidinone, and even in the intermediate-polarity solvents such as hexyl butyrate and benzyl acetate. Surprisingly, upon exposure to nonpolar (or less polar) solvents such as toluene and *o*-xylene, followed by drying and HT at 150 °C, Li$_2$ZrCl$_6$ lost its Li$^+$ conductivity (3 × 10^{-10} S cm^{-1} at 30 °C). The corresponding XRD patterns showed a complete structural collapse upon exposure to toluene or *o*-xylene (Figure 16b). While the XRD peaks were retained for the exposure to DBM

alone, the peak intensities were significantly lower. Accordingly, the degradation of Li$^+$ conductivity was less severe when compared to those exposed to toluene or *o*-xylene and was 2.4 × 10^{-8} S cm^{-1} at 30 °C. The chemical stabilities of Li$_2$ZrCl$_6$ varied according to the solvents employed, and were further confirmed by inductively coupled plasma optical emission spectroscopy (ICPOES) results (Figure 16a). Dissolution of Zr for Li$_2$ZrCl$_6$ into toluene and *o*-xylene was 3.64 and 0.53%, respectively, which is in sharp contrast to the behavior of sulfide SEs.[160,161] The lowest amount of Zr dissolution for Li$_2$ZrCl$_6$ into DBM (9.9 ppm) accounts for the retained crystal structure and the higher Li$^+$ conductivity, compared to those exposed to toluene and *o*-xylene. Considering the intactness of the pristine Li$_2$ZrCl$_6$ after HT at 150 °C, the 150 °C drying condition of Li$_2$ZrCl$_6$ in contact with solvents may also cause the degradation of the structures and the Li$^+$ conductivity.

In this context, an alternative dry-fabrication method would be attractive for halide SEs.[135,163−166] The absence of organic solvents in the dry-process is not only beneficial for maintaining the halide SEs intact, but also for conforming with the principles of green chemistry for reducing environmental pollution. Using sulfide SEs, Hippauf et al. successfully fabricated dry-film all-solid-state electrodes using fibrous polytetrafluoroethylene (PTFE) binders.[163] Owing to its characteristic morphology, the PTFE binder effectively held the entire electrode components together even when an impressively low amount of ~0.1 wt% was used. It is noteworthy that record-breaking results of ASSBs based on sulfide SEs have been achieved using dry-fabricated electrodes.[135,164] Recently, Wang et al. reported the assembly of solid-state pouch cells using Li$_3$InCl$_6$-coated LiCoO$_2$ by dry-film fabrication method.[165] The pouch cells delivered an initial capacity of 121.2 mA h g^{-1} and retained 68.6% capacity after 50 cycles. Figure 16c,d shows the first-cycle charge−discharge voltage profiles of dry-fabricated Li-Ni$_{0.8}$Co$_{0.1}$Mn$_{0.1}$O$_2$ electrodes using Li$_2$ZrCl$_6$ and the corresponding rate capability, respectively. Notably, the dry-fabricated electrodes exhibited a high discharge capacity of 185.3 mA h g^{-1} at 0.1C and 30 °C. Recent developments in the dry-fabrication processes for LIB technology could be considered the benchmarks for ASSBs.[167−171]

■ CONCLUSION AND OUTLOOK

Since the seminal report on halide SEs in 2018, several classes of halide SEs have been developed with good ionic conductivities, reaching as high as 1 mS cm^{-1}. In Figure 17, they are categorized into three types based on the group of the central metal, and their (electro)chemical properties are compared. "Group 3 metal halides", the halide SEs comprising group 3 metals, such as Sc, Y, and La−Lu, possess good intrinsic electrochemical

stabilities against oxidation and decent ionic conductivities. However, owing to the scarcity of the REMs, the large-scale practical application of the group 3 metal halide SEs is challenging. The degradation of halide SEs by hydrolysis upon exposure to humid air is another challenge in their efficient usage. Furthermore, reheating the humid-air-exposed samples for dehydration could emit the hazardous and corrosive HCl. This issue has been overlooked thus far and should be carefully investigated to assess the practical applicability of halide SEs. The known instability issues of halide SE hydrates could be circumvented using the ammonium chloride route, and the aqueous-solution synthesis could then be enabled. On the other hand, "group 13 metal halides", the halide SEs with the group 13 elements (Al, Ga, and In, e.g., Li_3InCl_6), especially the In compounds, showed exceptional humidity tolerance and high ionic conductivities of ≥ 1 mS cm^{-1}. Specifically, because the hydrated intermediates of Li_3InCl_6 are not highly vulnerable to hydrolysis, the aqueous solution synthesis and processing of Li_3InCl_6 are feasible. However, similar to the group 3 metal halide SEs, the high cost of In remains a formidable problem for the practical applications of Li_3InCl_6. Further, the relatively insufficient electrochemical stability of Li_3InCl_6 is another issue, which can be addressed by F$^-$ substitution. Zr was initially used as the substituent for the group 3 metal halide SEs to improve ionic conductivity. Thereafter, Li_2ZrCl_6 and its derivatives (e.g., $Li_{2+x}Zr_{1-x}Fe_xCl_6$) were developed and exhibited high ionic conductivities, reaching a maximum of 1 mS cm^{-1}. Importantly, Zr-based halide SEs retain excellent (electro)chemical stability against oxidation and simultaneously offer great advantages in cost, surpassing sulfide SEs. As discussed, the synthesis methods, such as the mechanochemical method or the solid-state reaction, and conditions, such as the HT temperature profile and the reaction time, significantly affect the phase evolution and/or site disorder and thus determine the ionic conductivities. As benchmarked in the argyrodite sulfides, both advanced experimental characterization and theoretical calculations are required to understand a detailed relationship between ionic conduction and local structural evolution in halide SEs. The Na$^+$ halide SEs, such as $Na_{3-x}Er_{1-x}Zr_xCl_6$, $Na_{3-x}Y_{1-x}Zr_xCl_6$, and Na_2ZrCl_6, crystallize differently from their Li$^+$ analogues, but the ionic conductivities of current Na$^+$ halide SEs are still too low, in the range of 10^{-5} S cm^{-1}, for practical ASSB applications. In addition to studying fundamental mechanisms, computation studies also provided multiple directions for the further improvement of halide SEs in the future. For example, the high-throughput computation studies established the design principles for further improving the ionic conductivity through tailoring compositions and anion/cation sublattice, which may be achieved with substitution and different synthesis protocols.[73] The comprehensive thermodynamic analyses for the electrochemical and moisture stabilities on a wide range of cations and anions also provide a guiding map for material selection and substitution to further increase the electrochemical and the moisture stabilities of halide SE materials.

> Importantly, Zr-based halide solid electrolytes retain excellent (electro)-chemical stability against oxidation and simultaneously offer great advantages in cost.

Wide electrochemical windows and good interfacial compatibility for these halide SEs with high-voltage cathodes are also evaluated and confirmed by thermodynamic analyses and experimental studies. Almost all of the halide SEs developed thus far have demonstrated excellent electrochemical stabilities and compatibility with uncoated 4 V LiMO$_2$ (or 3 V NaMO$_2$) in ASSBs. Specifically, combining halide SEs with the newly emerging cracking-free, single-crystalline, Ni-rich layered oxide CAMs showed promising cycling stabilities, which was in sharp contrast to the poor performance of the conventional polycrystalline LiMO$_2$ with sulfide SEs. However, to ensure competitiveness of halide SEs over sulfide SEs, further improvement in the ionic conductivity to the level comparable to that of the best sulfide SEs ($\sim$10 mS cm^{-1}) is necessary, which calls for further combined experimental and theoretical investigations. Moreover, halide SEs exhibit higher specific densities than those of sulfide SEs (Table 1), which translates to the lower specific energy densities of ASSBs. It is important to develop processing techniques to evenly distribute fine particles of halide SEs to form intimate contacts with CAMs, such as via a dry- or wet-coating method for the direct coatings on CAMs.

Their excellent properties make halide Li$^+$ conductors promising candidates for SEs, in addition to currently used sulfide and oxide SEs. In addition, halide SEs can replace the oxide-based protective coating materials such as LiNbO$_3$, Li$_2$ZrO$_3$, and Li$_{3-x}$B$_{1-x}$C$_x$O$_3$, that are widely used for sulfide-SE-based ASSBs. By further leveraging the demonstrated F-substitution strategy to increase the oxidation limits, halide SE coating or catholytes may enable the reversible operation of the high-voltage cathodes at 5 V or higher. However, as a critical drawback, halide SEs have intrinsically poor electrochemical reduction stability and show unsatisfactory passivating behavior at low voltages or in contact with Li metal anodes, which originates from the reduction of central metal ions. Although the formation of the kinetically stabilized SEI layers allowed the operation of Li metal anodes using halide SEs, the performance level has been far from competitive with sulfide SEs in terms of practical application. In this regard, the fabrication of ASSBs, wherein the halide and sulfide SEs are used for catholyte and anolyte (and/or separating SE layer), respectively, will combine advantages from the respective strengths of the components for facilitating practical development of ASSBs. In particular, the ASSBs with hybrid halide−sulfide SEs could adopt the Ag−C composite anodes.[135] For this hybrid configuration of halide−sulfide SE systems, possible instability issues between the halide and sulfide SEs at elevated temperatures need careful scrutiny.[172] Our preliminary results of the wet-slurry process for halide SEs indicated further restrictions to the use of the available processing solvents, compared to the cases using sulfide SEs, and exhibited severe degradation upon contact with even nonpolar or less-polar solvents such as toluene and *o*-xylene. Accordingly, newly emerging dry-fabrication processes using PTFE are considered appropriate for the fabrication of the cathodes or SE membranes using halide SEs.

Beyond the F-substitution in chloride SEs, which demonstrated the improved electrochemical stabilities both for cathodes and anodes, investigating all-fluoride compounds might be a promising research direction. Computational studies have demonstrated the promise of fluorides in achieving high oxidation stabilities.[48,129] Although current fluoride SEs exhibited low ionic conductivities, such as in the cases of α-Li$_3$AlF$_6$ (6×10^{-5} S cm^{-1} at 300 °C), Li$_2$TiF$_6$ (2×10^{-4} S cm^{-1} at 300 °C), β-Li$_3$AlF$_6$ (3.9×10^{-6} S cm^{-1} at 100 °C), and β-

> While fundamental studies to explore new materials chemistry spaces of halide superionic conductors are of great scientific values, comprehensive investigations are also urgently requested on many overlooked aspects for practical applications.

Li_3AlF_6/γ-Al_2O_3 (1.8×10^{-5} S cm^{-1} at 100 °C),[173,174] further exploration could open up opportunities for identifying compounds with improved ionic conductivities, which may further enable access to cathodes with a high-voltage of >5 V. Even if only mediocre ionic conductivities are realized using fluorides, these materials would still make excellent coating materials to enable access to high-voltage cathodes.[129] Although its reactivity with oxide SEs is a limitation, recently discovered xLiCl−GaF$_3$ showed an outstanding ionic conductivity of 3.6 mS cm^{-1} and clay-like mechanical characteristics with a storage and loss moduli of 1 MPa.[159]

In conclusion, the inherent advantages of halide SEs, such as excellent (electro)chemical oxidation stability, mechanical deformability, and decent ionic conductivities, are poised to transform ASSB technologies. While fundamental studies to explore new materials chemistry spaces of halide SICs are of great scientific value, comprehensive investigations are also urgently requested on many overlooked aspects for practical applications, including cost, atmospheric and chemical stabilities, synthesis methods, and the fabrication of composite electrodes and membranes, in order to realize the large-scale commercial applications of ASSBs based on halide SEs.

■ ASSOCIATED CONTENT

Ⓢ Supporting Information

The Supporting Information is available free of charge at https://pubs.acs.org/doi/10.1021/acsenergylett.2c00438.

Experimental methods; Table S1, comparing SE precursor costs for Li_6PS_5Cl and Li_2ZrCl_6 (PDF)

■ AUTHOR INFORMATION

Corresponding Authors

Yifei Mo − *Department of Materials Science and Engineering, University of Maryland, College Park, Maryland 20742, United States;* ⊙ orcid.org/0000-0002-8162-4629; Email: yfmo@umd.edu

Yoon Seok Jung − *School of Chemical and Biomolecular Engineering, Yonsei University, Seoul 03722, South Korea;* ⊙ orcid.org/0000-0003-0357-9508; Email: yoonsjung@yonsei.ac.kr

Authors

Hiram Kwak − *School of Chemical and Biomolecular Engineering, Yonsei University, Seoul 03722, South Korea*
Shuo Wang − *Department of Materials Science and Engineering, University of Maryland, College Park, Maryland 20742, United States*
Juhyoun Park − *School of Chemical and Biomolecular Engineering, Yonsei University, Seoul 03722, South Korea*
Yunsheng Liu − *Department of Materials Science and Engineering, University of Maryland, College Park, Maryland 20742, United States*

Kyu Tae Kim − *School of Chemical and Biomolecular Engineering, Yonsei University, Seoul 03722, South Korea*
Yeji Choi − *School of Chemical and Biomolecular Engineering, Yonsei University, Seoul 03722, South Korea*

Complete contact information is available at:
https://pubs.acs.org/10.1021/acsenergylett.2c00438

Author Contributions
⊥H.K. and S.W. contributed equally to this work.

Notes
The authors declare no competing financial interest.

Biographies

Hiram Kwak received his B.S. degree from UNIST (2017) and Ph.D. degree from Hanyang University (2022). Currently, he is a postdoctoral researcher in Prof. Yoon Seok Jung's group at Yonsei University. His main research topics are halide and sulfide solid electrolytes for all-solid-state batteries.

Shuo Wang received his Ph.D. degree from Peking University (2020). Currently, he is a postdoctoral researcher in Prof. Yifei Mo's group at the University of Maryland, College Park. His research focuses on understanding and developing novel superionic conductors for all-solid-state batteries.

Juhyoun Park is a Ph.D. student under the supervision of Prof. Yoon Seok Jung at Yonsei University. His research focuses on the design, synthesis, and characterization of halide solid electrolytes for all-solid-state Li and Na batteries.

Yunsheng Liu is a Ph.D. student in Prof. Yifei Mo's group at the University of Maryland, College Park. His research focuses on developing novel computational techniques for the atomic modeling of materials for solid-state batteries.

Kyu Tae Kim is a Ph.D. student under the supervision of Prof. Yoon Seok Jung at Yonsei University. His research focuses on the fabrication methods and functional binders for all-solid-state battery electrodes.

Yeji Choi is a Ph.D. student under in Prof. Yoon Seok Jung's group at Yonsei University. Her research focuses on the design, synthesis, and characterization of sulfide solid electrolytes for all-solid-state batteries.

Yifei Mo is a Professor of Materials Science and Engineering at the University of Maryland, College Park, USA. His research aims to advance the understanding, design, and discovery of materials through computational techniques, with current emphases on critical materials problems in energy storage and conversion technologies, including beyond Li-ion and all-solid-state batteries. http://www.mse.umd.edu/faculty/mo

Yoon Seok Jung is a Professor in the Department of Chemical and Biomolecular Engineering at Yonsei University. He received his B.S. and Ph.D. degrees (2008) from Seoul National University. He was a Professor at UNIST (2011−2018) and Hanyang University (2018-2020). His research interests cover materials to cells for rechargeable batteries, especially all-solid-state batteries. http://yoonsjung.yonsei.ac.kr/

■ ACKNOWLEDGMENTS

■ REFERENCES

(1) Xu, K. Nonaqueous Liquid Electrolytes for Lithium-Based Rechargeable Batteries. *Chem. Rev.* **2004**, *104*, 4303−4418.

(2) Goodenough, J. B.; Kim, Y. Challenges for Rechargeable Li Batteries. *Chem. Mater.* **2010**, *22*, 587−603.

(3) Choi, J. W.; Aurbach, D. Promise and reality of post-lithium-ion batteries with high energy densities. *Nat. Rev. Mater.* **2016**, *1*, 16013.

(4) Cheng, X.-B.; Zhang, R.; Zhao, C.-Z.; Zhang, Q. Toward Safe Lithium Metal Anode in Rechargeable Batteries: A Review. *Chem. Rev.* **2017**, *117*, 10403−10473.

(5) Janek, J.; Zeier, W. G. A solid future for battery development. *Nat. Energy* **2016**, *1*, 16141.

(6) Kato, Y.; Hori, S.; Saito, T.; Suzuki, K.; Hirayama, M.; Mitsui, A.; Yonemura, M.; Iba, H.; Kanno, R. High-power all-solid-state batteries using sulfide superionic conductors. *Nat. Energy* **2016**, *1*, 16030.

(7) Han, X.; Gong, Y.; Fu, K.; He, X.; Hitz, G. T.; Dai, J.; Pearse, A.; Liu, B.; Wang, H.; Rubloff, G.; Mo, Y.; Thangadurai, V.; Wachsman, E. D.; Hu, L. Negating interfacial impedance in garnet-based solid-state Li metal batteries. *Nat. Mater.* **2017**, *16*, 572−579.

(8) Manthiram, A.; Yu, X.; Wang, S. Lithium battery chemistries enabled by solid-state electrolytes. *Nat. Rev. Mater.* **2017**, *2*, 16103.

(9) Park, K. H.; Bai, Q.; Kim, D. H.; Oh, D. Y.; Zhu, Y.; Mo, Y.; Jung, Y. S. Design strategies, practical considerations, and new solution processes of sulfide solid electrolytes for all-solid-state batteries. *Adv. Energy Mater.* **2018**, *8*, 1800035.

(10) Zhao, Q.; Stalin, S.; Zhao, C.-Z.; Archer, L. A. Designing solid-state electrolytes for safe, energy-dense batteries. *Nat. Rev. Mater.* **2020**, *5*, 229−252.

(11) Li, X.; Liang, J.; Yang, X.; Adair, K. R.; Wang, C.; Zhao, F.; Sun, X. Progress and perspectives on halide lithium conductors for all-solid-state lithium batteries. *Energy Environ. Sci.* **2020**, *13*, 1429−1461.

(12) Wang, M. J.; Kazyak, E.; Dasgupta, N. P.; Sakamoto, J. Transitioning solid-state batteries from lab to market: Linking electro-chemo-mechanics with practical considerations. *Joule* **2021**, *5*, 1371−1390.

(13) Duffner, F.; Kronemeyer, N.; Tübke, J.; Leker, J.; Winter, M.; Schmuch, R. Post-lithium-ion battery cell production and its compatibility with lithium-ion cell production infrastructure. *Nat. Energy* **2021**, *6*, 123−134.

(14) Ding, P.; Lin, Z.; Guo, X.; Wu, L.; Wang, Y.; Guo, H.; Li, L.; Yu, H. Polymer electrolytes and interfaces in solid-state lithium metal batteries. *Mater. Today* **2021**, *51*, 449−474.

(15) Kamaya, N.; Homma, K.; Yamakawa, Y.; Hirayama, M.; Kanno, R.; Yonemura, M.; Kamiyama, T.; Kato, Y.; Hama, S.; Kawamoto, K.; Mitsui, A. A lithium superionic conductor. *Nat. Mater.* **2011**, *10*, 682−686.

(16) Hayashi, A.; Noi, K.; Sakuda, A.; Tatsumisago, M. Superionic glass-ceramic electrolytes for room-temperature rechargeable sodium batteries. *Nat. Commun.* **2012**, *3*, 856.

(17) Thangadurai, V.; Narayanan, S.; Pinzaru, D. Garnet-type solid-state fast Li ion conductors for Li batteries: critical review. *Chem. Soc. Rev.* **2014**, *43*, 4714−4727.

(18) Bachman, J. C.; Muy, S.; Grimaud, A.; Chang, H.-H.; Pour, N.; Lux, S. F.; Paschos, O.; Maglia, F.; Lupart, S.; Lamp, P.; Giordano, L.; Shao-Horn, Y. Inorganic Solid-State Electrolytes for Lithium Batteries: Mechanisms and Properties Governing Ion Conduction. *Chem. Rev.* **2016**, *116*, 140−162.

(19) Fan, L.; Wei, S.; Li, S.; Li, Q.; Lu, Y. Recent Progress of the Solid-State Electrolytes for High-Energy Metal-Based Batteries. *Adv. Energy Mater.* **2018**, *8*, 1702657.

(20) Zhang, Z.; Shao, Y.; Lotsch, B.; Hu, Y.-S.; Li, H.; Janek, J.; Nazar, L. F.; Nan, C.-W.; Maier, J.; Armand, M.; Chen, L. New horizons for inorganic solid state ion conductors. *Energy Environ. Sci.* **2018**, *11*, 1945−1976.

(21) Chen, R.; Li, Q.; Yu, X.; Chen, L.; Li, H. Approaching practically accessible solid-state batteries: stability issues related to solid electrolytes and interfaces. *Chem. Rev.* **2020**, *120*, 6820−6877.

(22) Han, Y.; Jung, S. H.; Kwak, H.; Jun, S.; Kwak, H. H.; Lee, J. H.; Hong, S.-T.; Jung, Y. S. Single- or Poly-Crystalline Ni-Rich Layered Cathode, Sulfide or Halide Solid Electrolyte: Which Will be the Winners for All-Solid-State Batteries? *Adv. Energy Mater.* **2021**, *11*, 2100126.

(23) Song, Y. B.; Kwak, H.; Cho, W.; Kim, K. S.; Jung, Y. S.; Park, K.-H. Electrochemo-mechanical effects as a critical design factor for all-solid-state batteries. *Curr. Opin. Solid State Mater. Sci.* **2022**, *26*, 100977.

(24) Deiseroth, H. J.; Kong, S. T.; Eckert, H.; Vannahme, J.; Reiner, C.; Zaiß, T.; Schlosser, M. Li₆PS₅X: a class of crystalline Li-rich solids with an unusually high Li+ mobility. *Angew. Chem., Int. Ed.* **2008**, *120*, 767−770.

(25) Zhou, L.; Minafra, N.; Zeier, W. G.; Nazar, L. F. Innovative Approaches to Li-Argyrodite Solid Electrolytes for All-Solid-State Lithium Batteries. *Acc. Chem. Res.* **2021**, *54*, 2717−2728.

(26) Stramare, S.; Thangadurai, V.; Weppner, W. Lithium lanthanum titanates: a review. *Chem. Mater.* **2003**, *15*, 3974−3990.

(27) Asano, T.; Sakai, A.; Ouchi, S.; Sakaida, M.; Miyazaki, A.; Hasegawa, S. Solid Halide Electrolytes with High Lithium-Ion Conductivity for Application in 4 V Class Bulk-Type All-Solid-State Batteries. *Adv. Mater.* **2018**, *30*, 1803075.

(28) Duchêne, L.; Remhof, A.; Hagemann, H.; Battaglia, C. Status and prospects of hydroborate electrolytes for all-solid-state batteries. *Energy Storage Mater.* **2020**, *25*, 782−794.

(29) Kim, S.; Oguchi, H.; Toyama, N.; Sato, T.; Takagi, S.; Otomo, T.; Arunkumar, D.; Kuwata, N.; Kawamura, J.; Orimo, S.-i. A complex hydride lithium superionic conductor for high-energy-density all-solid-state lithium metal batteries. *Nat. Commun.* **2019**, *10*, 1081.

(30) Kim, K. H.; Iriyama, Y.; Yamamoto, K.; Kumazaki, S.; Asaka, T.; Tanabe, K.; Fisher, C. A. J.; Hirayama, T.; Murugan, R.; Ogumi, Z. Characterization of the interface between LiCoO₂ and Li₇La₃Zr₂O₁₂ in an all-solid-state rechargeable lithium battery. *J. Power Sources* **2011**, *196*, 764−767.

(31) Zhu, Y.; He, X.; Mo, Y. Origin of Outstanding Stability in the Lithium Solid Electrolyte Materials: Insights from Thermodynamic Analyses Based on First-Principles Calculations. *ACS Appl. Mater. Interfaces* **2015**, *7*, 23685−23693.

(32) van den Broek, J.; Afyon, S.; Rupp, J. L. M. Interface-Engineered All-Solid-State Li-Ion Batteries Based on Garnet-Type Fast Li⁺ Conductors. *Adv. Energy Mater.* **2016**, *6*, 1600736.

(33) Fu, K.; Gong, Y.; Dai, J.; Gong, A.; Han, X.; Yao, Y.; Wang, C.; Wang, Y.; Chen, Y.; Yan, C.; Li, Y.; Wachsman, E. D.; Hu, L. Flexible, solid-state, ion-conducting membrane with 3D garnet nanofiber networks for lithium batteries. *Proc. Natl. Acad. Sci. U. S. A.* **2016**, *113*, 7094.

(34) Sakuda, A.; Hayashi, A.; Tatsumisago, M. Interfacial observation between LiCoO₂ electrode and Li₂S-P₂S₅ solid electrolytes of all-solid-state lithium secondary batteries using transmission electron microscopy. *Chem. Mater.* **2010**, *22*, 949−956.

(35) Xiao, Y.; Wang, Y.; Bo, S.-H.; Kim, J. C.; Miara, L. J.; Ceder, G. Understanding interface stability in solid-state batteries. *Nat. Rev. Mater.* **2020**, *5*, 105−126.

(36) Muramatsu, H.; Hayashi, A.; Ohtomo, T.; Hama, S.; Tatsumisago, M. Structural change of Li₂S-P₂S₅ sulfide solid electrolytes in the atmosphere. *Solid State Ion.* **2011**, *182*, 116−119.

(37) Zhu, Y.; Mo, Y. Materials Design Principles for Air-Stable Lithium/Sodium Solid Electrolytes. *Angew. Chem., Int. Ed.* **2020**, *59*, 17472−17476.

(38) Park, K. H.; Oh, D. Y.; Choi, Y. E.; Nam, Y. J.; Han, L.; Kim, J.-Y.; Xin, H.; Lin, F.; Oh, S. M.; Jung, Y. S. Solution-Processable Glass LiI-Li₄SnS₄ Superionic Conductors for All-Solid-State Li-Ion Batteries. *Adv. Mater.* **2016**, *28*, 1874−1883.

(39) Choi, Y. E.; Park, K. H.; Kim, D. H.; Oh, D. Y.; Kwak, H. R.; Lee, Y.-G.; Jung, Y. S. Coatable Li$_4$SnS$_4$ Solid Electrolytes Prepared from Aqueous Solutions for All-Solid-State Lithium-Ion Batteries. *ChemSusChem* **2017**, *10*, 2605−2611.

(40) Banerjee, A.; Park, K. H.; Heo, J. W.; Nam, Y. J.; Moon, C. K.; Oh, S. M.; Hong, S.-T.; Jung, Y. S. Na$_3$SbS$_4$: A Solution Processable Sodium Superionic Conductor for All-Solid-State Sodium-Ion Batteries. *Angew. Chem., Int. Ed.* **2016**, *55*, 9634−9638.

(41) Kwak, H.; Park, K. H.; Han, D.; Nam, K.-W.; Kim, H.; Jung, Y. S. Li$^+$ conduction in air-stable Sb-Substituted Li$_4$SnS$_4$ for all-solid-state Li-Ion batteries. *J. Power Sources* **2020**, *446*, 227338.

(42) Jung, S. H.; Oh, K.; Nam, Y. J.; Oh, D. Y.; Brüner, P.; Kang, K.; Jung, Y. S. Li$_3$BO$_3$-Li$_2$CO$_3$: Rationally Designed Buffering Phase for Sulfide All-Solid-State Li-Ion Batteries. *Chem. Mater.* **2018**, *30*, 8190−8200.

(43) Ohta, N.; Takada, K.; Sakaguchi, I.; Zhang, L.; Ma, R.; Fukuda, K.; Osada, M.; Sasaki, T. LiNbO$_3$-coated LiCoO$_2$ as cathode material for all solid-state lithium secondary batteries. *Electrochem. Commun.* **2007**, *9*, 1486−1490.

(44) Ito, S.; Fujiki, S.; Yamada, T.; Aihara, Y.; Park, Y.; Kim, T. Y.; Baek, S.-W.; Lee, J.-M.; Doo, S.; Machida, N. A rocking chair type all-solid-state lithium ion battery adopting Li$_2$O-ZrO$_2$ coated Li-Ni$_{0.8}$Co$_{0.15}$Al$_{0.05}$O$_2$ and a sulfide based electrolyte. *J. Power Sources* **2014**, *248*, 943−950.

(45) Strauss, F.; Teo, J. H.; Maibach, J.; Kim, A. Y.; Mazilkin, A.; Janek, J.; Brezesinski, T. Li$_2$ZrO$_3$-Coated NCM622 for Application in Inorganic Solid-State Batteries: Role of Surface Carbonates in the Cycling Performance. *ACS Appl. Mater. Interfaces* **2020**, *12*, 57146−57154.

(46) Ginnings, D. C.; Phipps, T. E. Temperature-Conductance Curves of Solid Salts. III. Halides of Lithium. *J. Am. Chem. Soc.* **1930**, *52*, 1340−1345.

(47) Wang, Y.; Richards, W. D.; Ong, S. P.; Miara, L. J.; Kim, J. C.; Mo, Y.; Ceder, G. Design principles for solid-state lithium superionic conductors. *Nat. Mater.* **2015**, *14*, 1026−1031.

(48) Wang, S.; Bai, Q.; Nolan, A. M.; Liu, Y.; Gong, S.; Sun, Q.; Mo, Y. Lithium Chlorides and Bromides as Promising Solid-State Chemistries for Fast Ion Conductors with Good Electrochemical Stability. *Angew. Chem., Int. Ed.* **2019**, *58*, 8039−8043.

(49) Kwak, H.; Han, D.; Lyoo, J.; Park, J.; Jung, S. H.; Han, Y.; Kwon, G.; Kim, H.; Hong, S.-T.; Nam, K.-W.; Jung, Y. S. New Cost-Effective Halide Solid Electrolytes for All-Solid-State Batteries: Mechanochemically Prepared Fe^{3+}-Substituted Li$_2$ZrCl$_6$. *Adv. Energy Mater.* **2021**, *11*, 2003190.

(50) Zhou, L.; Zuo, T.-T.; Kwok, C. Y.; Kim, S. Y.; Assoud, A.; Zhang, Q.; Janek, J.; Nazar, L. F. High areal capacity, long cycle life 4 V ceramic all-solid-state Li-ion batteries enabled by chloride solid electrolytes. *Nat. Energy* **2022**, *7*, 83−93.

(51) Park, J.; Han, D.; Kwak, H.; Han, Y.; Choi, Y. J.; Nam, K.-W.; Jung, Y. S. Heat treatment protocol for modulating ionic conductivity via structural evolution of Li$_{3-x}$Yb$_{1-x}$M$_x$Cl$_6$ (M = Hf^{4+}, Zr^{4+}) new halide superionic conductors for all-solid-state batteries. *Chem. Eng. J.* **2021**, *425*, 130630.

(52) Kim, S. Y.; Kaup, K.; Park, K.-H.; Assoud, A.; Zhou, L.; Liu, J.; Wu, X.; Nazar, L. F. Lithium Ytterbium-Based Halide Solid Electrolytes for High Voltage All-Solid-State Batteries. *ACS Mater. Lett.* **2021**, *3*, 930−938.

(53) Li, X.; Liang, J.; Luo, J.; Norouzi Banis, M.; Wang, C.; Li, W.; Deng, S.; Yu, C.; Zhao, F.; Hu, Y.; Sham, T.-K.; Zhang, L.; Zhao, S.; Lu, S.; Huang, H.; Li, R.; Adair, K. R.; Sun, X. Air-stable Li$_3$InCl$_6$ electrolyte with high voltage compatibility for all-solid-state batteries. *Energy Environ. Sci.* **2019**, *12*, 2665−2671.

(54) Liang, J.; Li, X.; Wang, S.; Adair, K. R.; Li, W.; Zhao, Y.; Wang, C.; Hu, Y.; Zhang, L.; Zhao, S.; Lu, S.; Huang, H.; Li, R.; Mo, Y.; Sun, X. Site-Occupation-Tuned Superionic Li$_x$ScCl$_{3+x}$ Halide Solid Electrolytes for All-Solid-State Batteries. *J. Am. Chem. Soc.* **2020**, *142*, 7012−7022.

(55) Liang, J.; Li, X.; Adair, K. R.; Sun, X. Metal Halide Superionic Conductors for All-Solid-State Batteries. *Acc. Chem. Res.* **2021**, *54*, 1023−1033.

(56) Moon, C. K.; Lee, H.-J.; Park, K. H.; Kwak, H.; Heo, J. W.; Choi, K.; Yang, H.; Kim, M.-S.; Hong, S.-T.; Lee, J. H.; Jung, Y. S. Vacancy-Driven Na$^+$ Superionic Conduction in New Ca-Doped Na$_3$PS$_4$ for All-Solid-State Na-Ion Batteries. *ACS Energy Lett.* **2018**, *3*, 2504−2512.

(57) West, A. R. *Solid state chemistry and its applications*; John Wiley & Sons, 2014.

(58) Li, X.; Liang, J.; Adair, K. R.; Li, J.; Li, W.; Zhao, F.; Hu, Y.; Sham, T.-K.; Zhang, L.; Zhao, S.; Lu, S.; Huang, H.; Li, R.; Chen, N.; Sun, X. Origin of Superionic Li$_3$Y$_{1-x}$In$_x$Cl$_6$ Halide Solid Electrolytes with High Humidity Tolerance. *Nano Lett.* **2020**, *20*, 4384−4392.

(59) Park, K.-H.; Kaup, K.; Assoud, A.; Zhang, Q.; Wu, X.; Nazar, L. F. High-Voltage Superionic Halide Solid Electrolytes for All-Solid-State Li-Ion Batteries. *ACS Energy Lett.* **2020**, *5*, 533−539.

(60) Helm, B.; Schlem, R.; Wankmiller, B.; Banik, A.; Gautam, A.; Ruhl, J.; Li, C.; Hansen, M. R.; Zeier, W. G. Exploring Aliovalent Substitutions in the Lithium Halide Superionic Conductor Li$_{3-x}$In$_{1-x}$Zr$_x$Cl$_6$ (0 ≤ x ≤ 0.5). *Chem. Mater.* **2021**, *33*, 4773−4782.

(61) Kwak, H.; Han, D.; Son, J. P.; Kim, J. S.; Park, J.; Nam, K.-W.; Kim, H.; Jung, Y. S. Li$^+$ conduction in aliovalent-substituted monoclinic Li$_2$ZrCl$_6$ for all-solid-state batteries: Li$_{2+x}$Zr$_{1-x}$M$_x$Cl$_6$ (M = In, Sc). *Chem. Eng. J.* **2022**, *437*, 135413.

(62) Schlem, R.; Muy, S.; Prinz, N.; Banik, A.; Shao-Horn, Y.; Zobel, M.; Zeier, W. G. Mechanochemical Synthesis: A Tool to Tune Cation Site Disorder and Ionic Transport Properties of Li$_3$MCl$_6$ (M = Y, Er) Superionic Conductors. *Adv. Energy Mater.* **2020**, *10*, 1903719.

(63) Steiner, H. J.; Lutz, H. D. Neue schnelle Ionenleiter vom Typ MMIIICl$_6$ (MI = Li, Na, Ag; MIII = In, Y). *Z. Anorg. Allg. Chem.* **1992**, *613*, 26−30.

(64) Tomita, Y.; Fuji-i, A.; Ohki, H.; Yamada, K.; Okuda, T. New Lithium Ion Conductor Li$_3$InBr$_6$ Studied by ^{7}Li NMR. *Chem. Lett.* **1998**, *27*, 223−224.

(65) Yamada, K.; Kumano, K.; Okuda, T. Lithium superionic conductors Li3InBr6 and LiInBr4 studied by ^{7}Li, ^{115}In NMR. *Solid State Ion.* **2006**, *177*, 1691−1695.

(66) Adelstein, N.; Wood, B. C. Role of Dynamically Frustrated Bond Disorder in a Li$^+$ Superionic Solid Electrolyte. *Chem. Mater.* **2016**, *28*, 7218−7231.

(67) Zevgolis, A.; Wood, B. C.; Mehmedović, Z.; Hall, A. T.; Alves, T. C.; Adelstein, N. Alloying effects on superionic conductivity in lithium indium halides for all-solid-state batteries. *APL Mater.* **2018**, *6*, 047903.

(68) Bohnsack, A.; Stenzel, F.; Zajonc, A.; Balzer, G.; Wickleder, M. S.; Meyer, G. Ternäre Halogenide vom Typ A$_3$MX$_6$. VI [1]. Ternäre Chloride der Selten-Erd-Elemente mit Lithium, Li$_3$MCl$_6$ (M = Tb-Lu, Y, Sc): Synthese, Kristallstrukturen und Ionenbewegung. *Z. Anorg. Allg. Chem.* **1997**, *623*, 1067−1073.

(69) Bohnsack, A.; Balzer, G.; Güdel, H.-U.; Wickleder, M. S.; Meyer, G. Ternäre Halogenide vom Typ A$_3$MX$_6$. VII [1]. Die Bromide Li$_3$MBr$_6$ (M = Sm-Lu, Y): Synthese, Kristallstruktur, Ionenbeweglichkeit. *Z. Anorg. Allg. Chem.* **1997**, *623*, 1352−1356.

(70) Kwak, H.; Lyoo, J.; Park, J.; Han, Y.; Asakura, R.; Remhof, A.; Battaglia, C.; Kim, H.; Hong, S.-T.; Jung, Y. S. Na$_2$ZrCl$_6$ enabling highly stable 3 V all-solid-state Na-ion batteries. *Energy Storage Mater.* **2021**, *37*, 47−54.

(71) Shannon, R. Revised effective ionic radii and systematic studies of interatomic distances in halides and chalcogenides. *Acta Cryst. A* **1976**, *32*, 751−767.

(72) Liu, Z.; Ma, S.; Liu, J.; Xiong, S.; Ma, Y.; Chen, H. High Ionic Conductivity Achieved in Li$_3$Y(Br$_3$Cl$_3$) Mixed Halide Solid Electrolyte via Promoted Diffusion Pathways and Enhanced Grain Boundary. *ACS Energy Lett.* **2021**, *6*, 298−304.

(73) Liu, Y.; Wang, S.; Nolan, A. M.; Ling, C.; Mo, Y. Tailoring the Cation Lattice for Chloride Lithium-Ion Conductors. *Adv. Energy Mater.* **2020**, *10*, 2002356.

(74) Kanno, R.; Takeda, Y.; Takada, K.; Yamamoto, O. Ionic Conductivity and Phase Transition of the Spinel System Li$_{2-2x}$M$_{1+x}$Cl$_4$ (M = Mg, Mn, Cd). *J. Electrochem. Soc.* **1984**, *131*, 469−474.

(75) Lutz, H. D.; Schmidt, W.; Haeuseler, H. Zur Kenntnis der Chlorid-Spinelle Li$_2$MgCl$_4$, Li$_2$MnCl$_4$, Li$_2$FeCl$_4$, Li$_2$CdCl$_4$. *Z. Anorg. Allg. Chem.* **1979**, *453*, 121−126.

(76) Schmidt, W.; Lutz, H. D. Fast Ionic Conductivity and Dielectric Properties of the Lithium Halide Spinels Li_2MnCl_4, Li_2CdCl_4, Li_2MnBr_4, and Li_2CdBr_4. *Berichte der Bunsengesellschaft für physikalische Chemie* **1984**, *88*, 720−723.

(77) Zhou, L.; Kwok, C. Y.; Shyamsunder, A.; Zhang, Q.; Wu, X.; Nazar, L. F. A new halospinel superionic conductor for high-voltage all solid state lithium batteries. *Energy Environ. Sci.* **2020**, *13*, 2056−2063.

(78) Ito, H.; Shitara, K.; Wang, Y.; Fujii, K.; Yashima, M.; Goto, Y.; Moriyoshi, C.; Rosero-Navarro, N. C.; Miura, A.; Tadanaga, K. Kinetically Stabilized Cation Arrangement in Li_3YCl_6 Superionic Conductor during Solid-State Reaction. *Adv. Sci.* **2021**, *8*, 2101413.

(79) Qi, J.; Banerjee, S.; Zuo, Y.; Chen, C.; Zhu, Z.; Holekevi Chandrappa, M. L.; Li, X.; Ong, S. P. Bridging the gap between simulated and experimental ionic conductivities in lithium superionic conductors. *Mater. Today Phys.* **2021**, *21*, 100463.

(80) Morgan, B. J. Mechanistic Origin of Superionic Lithium Diffusion in Anion-Disordered Li_6PS_5X Argyrodites. *Chem. Mater.* **2021**, *33*, 2004−2018.

(81) Kraft, M. A.; Ohno, S.; Zinkevich, T.; Koerver, R.; Culver, S. P.; Fuchs, T.; Senyshyn, A.; Indris, S.; Morgan, B. J.; Zeier, W. G. Inducing High Ionic Conductivity in the Lithium Superionic Argyrodites $Li_{6+x}P_{1-x}Ge_xS_5I$ for All-Solid-State Batteries. *J. Am. Chem. Soc.* **2018**, *140*, 16330−16339.

(82) Zhou, L.; Assoud, A.; Zhang, Q.; Wu, X.; Nazar, L. F. New Family of Argyrodite Thioantimonate Lithium Superionic Conductors. *J. Am. Chem. Soc.* **2019**, *141*, 19002−19013.

(83) Hayashi, A.; Masuzawa, N.; Yubuchi, S.; Tsuji, F.; Hotehama, C.; Sakuda, A.; Tatsumisago, M. A sodium-ion sulfide solid electrolyte with unprecedented conductivity at room temperature. *Nat. Commun.* **2019**, *10*, 5266.

(84) Papatheodorou, G. N. Raman spectroscopic studies of yttrium (III) chloride-alkali metal chloride melts and of Cs_2NaYCl_6 and YCl_3 solid compounds. *J. Chem. Phys.* **1977**, *66*, 2893−2900.

(85) Biswas, K.; Du, M.-H. Energy transport and scintillation of cerium-doped elpasolite Cs_2LiYCl_6: Hybrid density functional calculations. *Phys. Rev. B* **2012**, *86*, 014102.

(86) Park, K. H.; Kim, D. H.; Kwak, H.; Jung, S. H.; Lee, H.-J.; Banerjee, A.; Lee, J. H.; Jung, Y. S. Solution-derived glass-ceramic NaI·Na_3SbS_4 superionic conductors for all-solid-state Na-ion batteries. *J. Mater. Chem. A* **2018**, *6*, 17192−17200.

(87) Schlem, R.; Burmeister, C. F.; Michalowski, P.; Ohno, S.; Dewald, G. F.; Kwade, A.; Zeier, W. G. Energy Storage Materials for Solid-State Batteries: Design by Mechanochemistry. *Adv. Energy Mater.* **2021**, *11*, 2101022.

(88) Flores-González, N.; Minafra, N.; Dewald, G.; Reardon, H.; Smith, R. I.; Adams, S.; Zeier, W. G.; Gregory, D. H. Mechanochemical Synthesis and Structure of Lithium Tetrahaloaluminates, $LiAlX_4$ (X = Cl, Br, I): A Family of Li-Ion Conducting Ternary Halides. *ACS Mater. Lett.* **2021**, *3*, 652−657.

(89) Banik, A.; Famprikis, T.; Ghidiu, M.; Ohno, S.; Kraft, M. A.; Zeier, W. G. On the underestimated influence of synthetic conditions in solid ionic conductors. *Chem. Sci.* **2021**, *12*, 6238−6263.

(90) Mizuno, F.; Hayashi, A.; Tadanaga, K.; Tatsumisago, M. New, Highly Ion-Conductive Crystals Precipitated from Li_2S-P_2S_5 Glasses. *Adv. Mater.* **2005**, *17*, 918−921.

(91) Mizuno, F.; Hayashi, A.; Tadanaga, K.; Tatsumisago, M. High lithium ion conducting glass-ceramics in the system Li_2S-P_2S_5. *Solid State Ion.* **2006**, *177*, 2721−2725.

(92) Boulineau, S.; Courty, M.; Tarascon, J.-M.; Viallet, V. Mechanochemical synthesis of Li-argyrodite Li_6PS_5X (X = Cl, Br, I) as sulfur-based solid electrolytes for all solid state batteries application. *Solid State Ion.* **2012**, *221*, 1−5.

(93) Brinek, M.; Hiebl, C.; Wilkening, H. M. R. Understanding the Origin of Enhanced Li-Ion Transport in Nanocrystalline Argyrodite-Type Li_6PS_5I. *Chem. Mater.* **2020**, *32*, 4754−4766.

(94) Song, Y. B.; Kim, D. H.; Kwak, H.; Han, D.; Kang, S.; Lee, J. H.; Bak, S.-M.; Nam, K.-W.; Lee, H.-W.; Jung, Y. S. Tailoring Solution-Processable Li Argyrodites $Li_{6+x}P_{1-x}M_xS_5I$ (M = Ge, Sn) and Their

(95) Kraft, M. A.; Culver, S. P.; Calderon, M.; Böcher, F.; Krauskopf, T.; Senyshyn, A.; Dietrich, C.; Zevalkink, A.; Janek, J.; Zeier, W. G. Influence of Lattice Polarizability on the Ionic Conductivity in the Lithium Superionic Argyrodites Li_6PS_5X (X = Cl, Br, I). *J. Am. Chem. Soc.* **2017**, *139*, 10909−10918.

(96) Schlem, R.; Banik, A.; Ohno, S.; Suard, E.; Zeier, W. G. Insights into the Lithium Sub-structure of Superionic Conductors Li_3YCl_6 and Li_3YBr_6. *Chem. Mater.* **2021**, *33*, 327−337.

(97) Busche, M. R.; Weber, D. A.; Schneider, Y.; Dietrich, C.; Wenzel, S.; Leichtweiss, T.; Schröder, D.; Zhang, W.; Weigand, H.; Walter, D.; Sedlmaier, S. J.; Houtarde, D.; Nazar, L. F.; Janek, J. In Situ Monitoring of Fast Li-Ion Conductor $Li_7P_3S_{11}$ Crystallization Inside a Hot-Press Setup. *Chem. Mater.* **2016**, *28*, 6152−6165.

(98) Phuc, N. H. H.; Morikawa, K.; Mitsuhiro, T.; Muto, H.; Matsuda, A. Synthesis of plate-like Li_3PS_4 solid electrolyte via liquid-phase shaking for all-solid-state lithium batteries. *Ionics* **2017**, *23*, 2061−2067.

(99) Yubuchi, S.; Ito, A.; Masuzawa, N.; Sakuda, A.; Hayashi, A.; Tatsumisago, M. Aqueous solution synthesis of Na_3SbS_4-Na_2WS_4 superionic conductors. *J. Mater. Chem. A* **2020**, *8*, 1947−1954.

(100) Lee, J. E.; Park, K.-H.; Kim, J. C.; Wi, T.-U.; Ha, A. R.; Song, Y. B.; Oh, D. Y.; Woo, J.; Kweon, S. H.; Yeom, S. J.; Cho, W.; Kim, K.; Lee, H.-W.; Kwak, S. K.; Jung, Y. S. Universal Solution Synthesis of Sulfide Solid Electrolytes Using Alkahest for All-Solid-State Batteries. *Adv. Mater.* **2022**, 2200083.

(101) Liu, Z.; Fu, W.; Payzant, E. A.; Yu, X.; Wu, Z.; Dudney, N. J.; Kiggans, J.; Hong, K.; Rondinone, A. J.; Liang, C. Anomalous High Ionic Conductivity of Nanoporous β-Li_3PS_4. *J. Am. Chem. Soc.* **2013**, *135*, 975−978.

(102) Rangasamy, E.; Liu, Z.; Gobet, M.; Pilar, K.; Sahu, G.; Zhou, W.; Wu, H.; Greenbaum, S.; Liang, C. An Iodide-Based $Li_7P_2S_8I$ Superionic Conductor. *J. Am. Chem. Soc.* **2015**, *137*, 1384−1387.

(103) Sedlmaier, S. J.; Indris, S.; Dietrich, C.; Yavuz, M.; Dräger, C.; von Seggern, F.; Sommer, H.; Janek, J. Li_4PS_4I: A Li^+ Superionic Conductor Synthesized by a Solvent-Based Soft Chemistry Approach. *Chem. Mater.* **2017**, *29*, 1830−1835.

(104) Yubuchi, S.; Teragawa, S.; Aso, K.; Tadanaga, K.; Hayashi, A.; Tatsumisago, M. Preparation of high lithium-ion conducting Li_6PS_5Cl solid electrolyte from ethanol solution for all-solid-state lithium batteries. *J. Power Sources* **2015**, *293*, 941−945.

(105) Kim, D. H.; Oh, D. Y.; Park, K. H.; Choi, Y. E.; Nam, Y. J.; Lee, H. A.; Lee, S.-M.; Jung, Y. S. Infiltration of Solution-Processable Solid Electrolytes into Conventional Li-Ion-Battery Electrodes for All-Solid-State Li-Ion Batteries. *Nano Lett.* **2017**, *17*, 3013−3020.

(106) Oh, D. Y.; Kim, D. H.; Jung, S. H.; Han, J.-G.; Choi, N.-S.; Jung, Y. S. Single-step wet-chemical fabrication of sheet-type electrodes from solid-electrolyte precursors for all-solid-state lithium-ion batteries. *J. Mater. Chem. A* **2017**, *5*, 20771−20779.

(107) Kim, T. W.; Park, K. H.; Choi, Y. E.; Lee, J. Y.; Jung, Y. S. Aqueous-solution synthesis of Na_3SbS_4 solid electrolytes for all-solid-state Na-ion batteries. *J. Mater. Chem. A* **2018**, *6*, 840−844.

(108) Heo, J. W.; Banerjee, A.; Park, K. H.; Jung, Y. S.; Hong, S.-T. New Na-Ion Solid Electrolytes $Na_{4-x}Sn_{1-x}Sb_xS_4$ ($0.02 \leq x \leq 0.33$) for All-Solid-State Na-Ion Batteries. *Adv. Energy Mater.* **2018**, *8*, 1702716.

(109) Kim, D. H.; Lee, Y.-H.; Song, Y. B.; Kwak, H.; Lee, S.-Y.; Jung, Y. S. Thin and Flexible Solid Electrolyte Membranes with Ultrahigh Thermal Stability Derived from Solution-Processable Li Argyrodites for All-Solid-State Li-Ion Batteries. *ACS Energy Lett.* **2020**, *5*, 718−727.

(110) Duchêne, L.; Kim, D. H.; Song, Y. B.; Jun, S.; Moury, R.; Remhof, A.; Hagemann, H.; Jung, Y. S.; Battaglia, C. Crystallization of closo-borate electrolytes from solution enabling infiltration into slurry-casted porous electrodes for all-solid-state batteries. *Energy Storage Mater.* **2020**, *26*, 543−549.

(111) Li, X.; Liang, J.; Chen, N.; Luo, J.; Adair, K. R.; Wang, C.; Banis, M. N.; Sham, T.-K.; Zhang, L.; Zhao, S.; Lu, S.; Huang, H.; Li, R.; Sun, X. Water-Mediated Synthesis of a Superionic Halide Solid Electrolyte. *Angew. Chem., Int. Ed.* **2019**, *58*, 16427−16432.

Microstructural Evolution Revealed by Cryo-TEM for All-Solid-State Batteries. *Nano Lett.* **2020**, *20*, 4337−4345.

(112) Wang, C.; Liang, J.; Luo, J.; Liu, J.; Li, X.; Zhao, F.; Li, R.; Huang, H.; Zhao, S.; Zhang, L.; Wang, J.; Sun, X. A universal wet-chemistry synthesis of solid-state halide electrolytes for all-solid-state lithium-metal batteries. *Sci. Adv.* **2021**, *7*, No. eabh1896.

(113) Shi, X.; Zeng, Z.; Zhang, H.; Huang, B.; Sun, M.; Wong, H. H.; Lu, Q.; Luo, W.; Huang, Y.; Du, Y.; Yan, C.-H. Gram-Scale Synthesis of Nanosized Li$_3$HoBr$_6$ Solid Electrolyte for All-Solid-State Li-Se Battery. *Small Methods* **2021**, *5*, 2101002.

(114) Li, W.; Liang, J.; Li, M.; Adair, K. R.; Li, X.; Hu, Y.; Xiao, Q.; Feng, R.; Li, R.; Zhang, L.; Lu, S.; Huang, H.; Zhao, S.; Sham, T.-K.; Sun, X. Unraveling the Origin of Moisture Stability of Halide Solid-State Electrolytes by In Situ and Operando Synchrotron X-ray Analytical Techniques. *Chem. Mater.* **2020**, *32*, 7019−7027.

(115) Wang, C.; Liang, J.; Jiang, M.; Li, X.; Mukherjee, S.; Adair, K.; Zheng, M.; Zhao, Y.; Zhao, F.; Zhang, S.; Li, R.; Huang, H.; Zhao, S.; Zhang, L.; Lu, S.; Singh, C. V.; Sun, X. Interface-assisted in-situ growth of halide electrolytes eliminating interfacial challenges of all-inorganic solid-state batteries. *Nano Energy* **2020**, *76*, 105015.

(116) Zhao, B.; Lu, Y.; Yuan, B.; Wang, Z.; Han, X. Preparation of free-standing Li$_3$InCl$_6$ solid electrolytes film with infiltration-method enable roll-to-roll manufacture. *Mater. Lett.* **2022**, *310*, 131463.

(117) Taylor, M. D. Preparation of Anhydrous Lanthanon Halides. *Chem. Rev.* **1962**, *62*, 503−511.

(118) Weigel, F.; Wishnevsky, V. Die Dampfphasenhydrolyse von Lanthaniden(III)-chloriden, 5. Wärmetönung und Gibbs-Energie der Reaktion MCl$_3$ (f) + H$_2$O (g) ⇌ MOCl (f) + 2HCl (g) (M = Y, Tb). *Chem. Ber.* **1973**, *106*, 1976−1984.

(119) Meyer, G.; Ax, P. An analysis of the ammonium chloride route to anhydrous rare-earth metal chlorides. *Mater. Res. Bull.* **1982**, *17*, 1447−1455.

(120) Park, D.; Kim, K.; Chun, G. H.; Wood, B. C.; Shim, J. H.; Yu, S. Materials design of sodium chloride solid electrolytes Na$_3$MCl$_6$ for all-solid-state sodium-ion batteries. *J. Mater. Chem. A* **2021**, *9*, 23037−23045.

(121) Qie, Y.; Wang, S.; Fu, S.; Xie, H.; Sun, Q.; Jena, P. Yttrium-Sodium Halides as Promising Solid-State Electrolytes with High Ionic Conductivity and Stability for Na-Ion Batteries. *J. Phys. Chem. Lett.* **2020**, *11*, 3376−3383.

(122) Schlem, R.; Banik, A.; Eckardt, M.; Zobel, M.; Zeier, W. G. Na$_{3-x}$Er$_{1-x}$Zr$_x$Cl$_6$—A Halide-Based Fast Sodium-Ion Conductor with Vacancy-Driven Ionic Transport. *ACS Appl. Energy Mater.* **2020**, *3*, 10164−10173.

(123) Wu, E. A.; Banerjee, S.; Tang, H.; Richardson, P. M.; Doux, J.-M.; Qi, J.; Zhu, Z.; Grenier, A.; Li, Y.; Zhao, E.; Deysher, G.; Sebti, E.; Nguyen, H.; Stephens, R.; Verbist, G.; Chapman, K. W.; Clément, R. J.; Banerjee, A.; Meng, Y. S.; Ong, S. P. A stable cathode-solid electrolyte composite for high-voltage, long-cycle-life solid-state sodium-ion batteries. *Nat. Commun.* **2021**, *12*, 1256.

(124) Meyer, G.; Peter Ax, S.; Schleid, T.; Irmler, M. The chlorides Na$_3$MCl$_6$ (M = Eu-Lu, Y, Sc): Synthesis, crystal structures, and thermal behaviour. *Z. Anorg. Allg. Chem.* **1987**, *554*, 25−33.

(125) Yamada, K.; Kumano, K.; Okuda, T. Conduction path of the sodium ion in Na$_3$InCl$_6$ studied by X-ray diffraction and ^{23}Na and ^{115}In NMR. *Solid State Ion.* **2005**, *176*, 823−829.

(126) Yu, T.; Liang, J.; Luo, L.; Wang, L.; Zhao, F.; Xu, G.; Bai, X.; Yang, R.; Zhao, S.; Wang, J.; Yu, J.; Sun, X. Superionic Fluorinated Halide Solid Electrolytes for Highly Stable Li-Metal in All-Solid-State Li Batteries. *Adv. Energy Mater.* **2021**, *11*, 2101915.

(127) Zhang, S.; Zhao, F.; Wang, S.; Liang, J.; Wang, J.; Wang, C.; Zhang, H.; Adair, K.; Li, W.; Li, M.; Duan, H.; Zhao, Y.; Yu, R.; Li, R.; Huang, H.; Zhang, L.; Zhao, S.; Lu, S.; Sham, T.-K.; Mo, Y.; Sun, X. Advanced High-Voltage All-Solid-State Li-Ion Batteries Enabled by a Dual-Halogen Solid Electrolyte. *Adv. Energy Mater.* **2021**, *11*, 2100836.

(128) Nolan, A. M.; Wachsman, E. D.; Mo, Y. Computation-guided discovery of coating materials to stabilize the interface between lithium garnet solid electrolyte and high-energy cathodes for all-solid-state lithium batteries. *Energy Storage Mater.* **2021**, *41*, 571−580.

(129) Nolan, A. M.; Liu, Y.; Mo, Y. Solid-state chemistries stable with high-energy cathodes for lithium-ion batteries. *ACS Energy Lett.* **2019**, *4*, 2444−2451.

(130) Sun, Y.-K.; Myung, S.-T.; Park, B.-C.; Prakash, J.; Belharouak, I.; Amine, K. High-energy cathode material for long-life and safe lithium batteries. *Nat. Mater.* **2009**, *8*, 320−324.

(131) Liu, W.; Oh, P.; Liu, X.; Lee, M.-J.; Cho, W.; Chae, S.; Kim, Y.; Cho, J. Nickel-Rich Layered Lithium Transition-Metal Oxide for High-Energy Lithium-Ion Batteries. *Angew. Chem., Int. Ed.* **2015**, *54*, 4440−4457.

(132) Manthiram, A.; Knight, J. C.; Myung, S.-T.; Oh, S.-M.; Sun, Y.-K. Nickel-Rich and Lithium-Rich Layered Oxide Cathodes: Progress and Perspectives. *Adv. Energy Mater.* **2016**, *6*, 1501010.

(133) Manthiram, A.; Song, B.; Li, W. A perspective on nickel-rich layered oxide cathodes for lithium-ion batteries. *Energy Storage Mater.* **2017**, *6*, 125−139.

(134) Jung, S. H.; Kim, U.-H.; Kim, J.-H.; Jun, S.; Yoon, C. S.; Jung, Y. S.; Sun, Y.-K. Ni-Rich Layered Cathode Materials with Electrochemo-Mechanically Compliant Microstructures for All-Solid-State Li Batteries. *Adv. Energy Mater.* **2020**, *10*, 1903360.

(135) Lee, Y.-G.; Fujiki, S.; Jung, C.; Suzuki, N.; Yashiro, N.; Omoda, R.; Ko, D.-S.; Shiratsuchi, T.; Sugimoto, T.; Ryu, S.; Ku, J. H.; Watanabe, T.; Park, Y.; Aihara, Y.; Im, D.; Han, I. T. High-energy long-cycling all-solid-state lithium metal batteries enabled by silver-carbon composite anodes. *Nat. Energy* **2020**, *5*, 299−308.

(136) Zhang, Z.; Zhang, L.; Yan, X.; Wang, H.; Liu, Y.; Yu, C.; Cao, X.; van Eijck, L.; Wen, B. All-in-one improvement toward Li$_6$PS$_5$Br-Based solid electrolytes triggered by compositional tune. *J. Power Sources* **2019**, *410−411*, 162−170.

(137) Sun, Y.; Suzuki, K.; Hara, K.; Hori, S.; Yano, T.-a.; Hara, M.; Hirayama, M.; Kanno, R. Oxygen substitution effects in Li$_{10}$GeP$_2$S$_{12}$ solid electrolyte. *J. Power Sources* **2016**, *324*, 798−803.

(138) Xu, G.; Luo, L.; Liang, J.; Zhao, S.; Yang, R.; Wang, C.; Yu, T.; Wang, L.; Xiao, W.; Wang, J.; Yu, J.; Sun, X. Origin of high electrochemical stability of multi-metal chloride solid electrolytes for high energy all-solid-state lithium-ion batteries. *Nano Energy* **2022**, *92*, 106674.

(139) Haynes, W. M., Abundance of Elements in the Earth's Crust and in the Sea. *CRC Handbook of Chemistry and Physics*, 95th edition, Internet Version, 2016. DOI: 10.1201/9781315380476

(140) Wenzel, S.; Sedlmaier, S. J.; Dietrich, C.; Zeier, W. G.; Janek, J. Interfacial reactivity and interphase growth of argyrodite solid electrolytes at lithium metal electrodes. *Solid State Ion.* **2018**, *318*, 102−112.

(141) Peled, E. The Electrochemical Behavior of Alkali and Alkaline Earth Metals in Nonaqueous Battery Systems—The Solid Electrolyte Interphase Model. *J. Electrochem. Soc.* **1979**, *126*, 2047−2051.

(142) Li, Y.; Li, Y.; Pei, A.; Yan, K.; Sun, Y.; Wu, C.-L.; Joubert, L.-M.; Chin, R.; Koh, A. L.; Yu, Y.; Perrino, J.; Butz, B.; Chu, S.; Cui, Y. Atomic structure of sensitive battery materials and interfaces revealed by cryo-electron microscopy. *Sci.* **2017**, *358*, 506−510.

(143) Riegger, L. M.; Schlem, R.; Sann, J.; Zeier, W. G.; Janek, J. Lithium-Metal Anode Instability of the Superionic Halide Solid Electrolytes and the Implications for Solid-State Batteries. *Angew. Chem., Int. Ed.* **2021**, *60*, 6718−6723.

(144) Wang, S.; Xu, X.; Cui, C.; Zeng, C.; Liang, J.; Fu, J.; Zhang, R.; Zhai, T.; Li, H. Air Sensitivity and Degradation Evolution of Halide Solid State Electrolytes upon Exposure. *Adv. Funct. Mater.* **2022**, *32*, 2108805.

(145) Wang, K.; Ren, Q.; Gu, Z.; Duan, C.; Wang, J.; Zhu, F.; Fu, Y.; Hao, J.; Zhu, J.; He, L.; Wang, C.-W.; Lu, Y.; Ma, J.; Ma, C. A cost-effective and humidity-tolerant chloride solid electrolyte for lithium batteries. *Nat. Commun.* **2021**, *12*, 4410.

(146) Hart, P. W.; Sommerfeld, J. T. Cost estimation of specialty chemicals from laboratory-scale prices: a Publication of the American Association of Cost Engineers. *Cost Eng.* **1997**, *39* (3), 31−35.

(147) Schnell, J.; Günther, T.; Knoche, T.; Vieider, C.; Köhler, L.; Just, A.; Keller, M.; Passerini, S.; Reinhart, G. All-solid-state lithium-ion

and lithium metal batteries - paving the way to large-scale production. *J. Power Sources* **2018**, *382*, 160−175.

(148) Schnell, J.; Knörzer, H.; Imbsweiler, A. J.; Reinhart, G. Solid versus Liquid—A Bottom-Up Calculation Model to Analyze the Manufacturing Cost of Future High-Energy Batteries. *Energy Technol.* **2020**, *8*, 1901237.

(149) Strelow, F. W. E.; Rethemeyer, R.; Bothma, C. J. C. Ion Exchange Selectivity Scales for Cations in Nitric Acid and Sulfuric Acid Media with a Sulfonated Polystyrene Resin. *Anal. Chem.* **1965**, *37*, 106−111.

(150) Kelly, J. R.; Denry, I. Stabilized zirconia as a structural ceramic: An overview. *Dent. Mater.* **2008**, *24*, 289−298.

(151) Chen, Y.-W.; Moussi, J.; Drury, J. L.; Wataha, J. C. Zirconia in biomedical applications. *Expert Rev. Med. Devices* **2016**, *13*, 945−963.

(152) Zhang, X.; Wu, X.; Shi, J. Additive manufacturing of zirconia ceramics: a state-of-the-art review. *J. Mater. Res. Technol.* **2020**, *9*, 9029−9048.

(153) Budi, S.; Sunarjo; Dwiretnani, S.; Pristi, H. The Effect of Composition and Pressure on Briquette Production of Zircon Sand Toward Chlorination Conversion; *Proceeding of the Scientific Meeting and Presentation on Basic Research in Nuclear Science and Technology part II: Nuclear Chemistry, Process Technology, Radioactive Waste Management and Environment*; National Nuclear Energy Agency: Indonesia, 2002; p 359.

(154) Nam, Y. J.; Cho, S.-J.; Oh, D. Y.; Lim, J.-M.; Kim, S. Y.; Song, J. H.; Lee, Y.-G.; Lee, S.-Y.; Jung, Y. S. Bendable and Thin Sulfide Solid Electrolyte Film: A New Electrolyte Opportunity for Free-Standing and Stackable High-Energy All-Solid-State Lithium-Ion Batteries. *Nano Lett.* **2015**, *15*, 3317−3323.

(155) Nam, Y. J.; Oh, D. Y.; Jung, S. H.; Jung, Y. S. Toward practical all-solid-state lithium-ion batteries with high energy density and safety: Comparative study for electrodes fabricated by dry- and slurry-mixing processes. *J. Power Sources* **2018**, *375*, 93−101.

(156) Oh, D. Y.; Nam, Y. J.; Park, K. H.; Jung, S. H.; Kim, K. T.; Ha, A. R.; Jung, Y. S. Slurry-Fabricable Li$^+$-Conductive Polymeric Binders for Practical All-Solid-State Lithium-Ion Batteries Enabled by Solvate Ionic Liquids. *Adv. Energy Mater.* **2019**, *9*, 1802927.

(157) Wang, C.; Liang, J.; Zhao, Y.; Zheng, M.; Li, X.; Sun, X. All-solid-state lithium batteries enabled by sulfide electrolytes: from fundamental research to practical engineering design. *Energy Environ. Sci.* **2021**, *14*, 2577−2619.

(158) Wu, J.; Yuan, L.; Zhang, W.; Li, Z.; Xie, X.; Huang, Y. Reducing the thickness of solid-state electrolyte membranes for high-energy lithium batteries. *Energy Environ. Sci.* **2021**, *14*, 12−36.

(159) Jung, S.-K.; Gwon, H.; Yoon, G.; Miara, L. J.; Lacivita, V.; Kim, J.-S. Pliable Lithium Superionic Conductor for All-Solid-State Batteries. *ACS Energy Lett.* **2021**, *6*, 2006−2015.

(160) Kim, K. T.; Oh, D. Y.; Jun, S.; Song, Y. B.; Kwon, T. Y.; Han, Y.; Jung, Y. S. Tailoring Slurries Using Cosolvents and Li Salt Targeting Practical All-Solid-State Batteries Employing Sulfide Solid Electrolytes. *Adv. Energy Mater.* **2021**, *11*, 2003766.

(161) Oh, D. Y.; Kim, K. T.; Jung, S. H.; Kim, D. H.; Jun, S.; Jeoung, S.; Moon, H. R.; Jung, Y. S. Tactical hybrids of Li$^+$-conductive dry polymer electrolytes with sulfide solid electrolytes: Toward practical all-solid-state batteries with wider temperature operability. *Mater. Today* **2021**, DOI: 10.1016/j.mattod.2021.01.006.

(162) Lee, K.; Kim, S.; Park, J.; Park, S. H.; Coskun, A.; Jung, D. S.; Cho, W.; Choi, J. W. Selection of Binder and Solvent for Solution-Processed All-Solid-State Battery. *J. Electrochem. Soc.* **2017**, *164*, A2075−A2081.

(163) Hippauf, F.; Schumm, B.; Doerfler, S.; Althues, H.; Fujiki, S.; Shiratsuchi, T.; Tsujimura, T.; Aihara, Y.; Kaskel, S. Overcoming binder limitations of sheet-type solid-state cathodes using a solvent-free dry-film approach. *Energy Storage Mater.* **2019**, *21*, 390−398.

(164) Tan, D. H. S.; Chen, Y.-T.; Yang, H.; Bao, W.; Sreenarayanan, B.; Doux, J.-M.; Li, W.; Lu, B.; Ham, S.-Y.; Sayahpour, B.; Scharf, J.; Wu, E. A.; Deysher, G.; Han, H. E.; Hah, H. J.; Jeong, H.; Lee, J. B.; Chen, Z.; Meng, Y. S. Carbon-free high-loading silicon anodes enabled by sulfide solid electrolytes. *Science* **2021**, *373*, 1494−1499.

(165) Wang, C.; Yu, R.; Duan, H.; Lu, Q.; Li, Q.; Adair, K. R.; Bao, D.; Liu, Y.; Yang, R.; Wang, J.; Zhao, S.; Huang, H.; Sun, X. Solvent-Free Approach for Interweaving Freestanding and Ultrathin Inorganic Solid Electrolyte Membranes. *ACS Energy Lett.* **2022**, *7*, 410−416.

(166) Lu, Y.; Zhao, C.-Z.; Yuan, H.; Hu, J.-K.; Huang, J.-Q.; Zhang, Q. Dry electrode technology, the rising star in solid-state battery industrialization. *Matter* **2022**, *5*, 876−898.

(167) Ludwig, B.; Zheng, Z.; Shou, W.; Wang, Y.; Pan, H. Solvent-Free Manufacturing of Electrodes for Lithium-ion Batteries. *Sci. Rep.* **2016**, *6*, 23150.

(168) Astafyeva, K.; Dousset, C.; Bureau, Y.; Stalmach, S.-L.; Dufour, B. High Energy Li-Ion Electrodes Prepared via a Solventless Melt Process. *Batter. Supercaps* **2020**, *3*, 341−343.

(169) El Khakani, S.; Verdier, N.; Lepage, D.; Prébé, A.; Aymé-Perrot, D.; Rochefort, D.; Dollé, M. Melt-processed electrode for lithium ion battery. *J. Power Sources* **2020**, *454*, 227884.

(170) Froboese, L.; Groffmann, L.; Monsees, F.; Helmers, L.; Loellhoeffel, T.; Kwade, A. Enhancing the Lithium Ion Conductivity of an All Solid-State Electrolyte via Dry and Solvent-Free Scalable Series Production Processes. *J. Electrochem. Soc.* **2020**, *167*, 020558.

(171) Schälicke, G.; Landwehr, I.; Dinter, A.; Pettinger, K.-H.; Haselrieder, W.; Kwade, A. Solvent-Free Manufacturing of Electrodes for Lithium-Ion Batteries via Electrostatic Coating. *Energy Technol.* **2020**, *8*, 1900309.

(172) Koç, T.; Marchini, F.; Rousse, G.; Dugas, R.; Tarascon, J.-M. In Search of the Best Solid Electrolyte-Layered Oxide Pairing for Assembling Practical All-Solid-State Batteries. *ACS Appl. Energy Mater.* **2021**, *4*, 13575−13585.

(173) Feinauer, M.; Euchner, H.; Fichtner, M.; Reddy, M. A. Unlocking the Potential of Fluoride-Based Solid Electrolytes for Solid-State Lithium Batteries. *ACS Appl. Energy Mater.* **2019**, *2*, 7196−7203.

(174) Esaka, T.; Okuyama, R.; Iwahara, H. Ionic conduction in sintered fluorocomplexes Li$_m$MF$_6$, M = Al, Ti. *Solid State Ion.* **1989**, *34*, 201−205.

(175) Oi, T.; Miyauchi, K. Amorphous thin film ionic conductors of mLiF.nAlF$_3$. *Mater. Res. Bull.* **1981**, *16*, 1281−1289.

(176) Adeli, P.; Bazak, J. D.; Park, K. H.; Kochetkov, I.; Huq, A.; Goward, G. R.; Nazar, L. F. Boosting Solid-State Diffusivity and Conductivity in Lithium Superionic Argyrodites by Halide Substitution. *Angew. Chem., Int. Ed.* **2019**, *58*, 8681−8686.

(177) Buschmann, H.; Dölle, J.; Berendts, S.; Kuhn, A.; Bottke, P.; Wilkening, M.; Heitjans, P.; Senyshyn, A.; Ehrenberg, H.; Lotnyk, A.; Duppel, V.; Kienle, L.; Janek, J. Structure and dynamics of the fast lithium ion conductor "Li$_7$La$_3$Zr$_2$O$_{12}$. *Phys. Chem. Chem. Phys.* **2011**, *13*, 19378−19392.

(178) Fourquet, J. L.; Duroy, H.; Crosnier-Lopez, M. P. Structural and Microstructural Studies of the Series La$_{2/3-x}$Li$_{3x\square1/3-2x}$TiO$_3$. *J. Solid State Chem.* **1996**, *127*, 283−294.

(179) Waetzig, K.; Rost, A.; Langklotz, U.; Matthey, B.; Schilm, J. An explanation of the microcrack formation in Li$_{1.3}$Al$_{0.3}$Ti$_{1.7}$(PO$_4$)$_3$ ceramics. *J. Eur. Ceram. Soc.* **2016**, *36*, 1995−2001.